Ca' Foscari University of Venice

Master's Degree Programme in

Science and Technology of Bio and Nanomaterials

(LM-53)

Master Thesis

Nanostructured Materials for the Photo-driven Conversion of CO_2

An Investigation on the Strategies for Improved Photo-Catalysis by Metal Oxide Semiconductors

Supervisor: Distinguished Prof. Michela Signoretto

Co-supervisor: Distinguished Prof. Isabella Concina

Graduating Student: Giulia Forghieri

Academic Year: 2019/2020

SUMMARY

Nanostructured Materials

for the photo-driven Conversion of CO_2

“Be the change
you want to see
in the world.”

M. Gandhi

Nanostructured Materials for the Photo-driven Conversion of CO_2

Preface

1. Abstract

One of the attempts to climate change mitigation, as response to the forecast of increasing temperature, consisted in the control of the increasing levels of greenhouse gases (GHG), such as carbon dioxide (CO_2), by means of the implementation of carbon capture and utilization (CCU) technologies. The employment of two different systems for the capture and the utilization of CO_2 have so far required an additional energetic supply in form of heat or electricity, to afford consequent CO_2 conversion. The latter mainly relies on thermo- and electro-driven conversions, with less attention for photo-catalytic systems.

In this study, zinc oxide (ZnO) and titanium oxide (TiO_2) were tested first as candidates for the coupled capture and direct conversion of CO_2, using light as energetic source and requiring no additional energetic supply, and then for the electro-assisted photo-catalysis, in presence of a bias potential, as cleaner and cheaper alternative to the more widely employed metals.

The first experimental activities were performed with the CATMAT research group at Venice Ca' Foscari University, where the material synthesis, the photo-catalytic tests and part of the structural, optical and functional characterization took place. Here, different approaches such as metal-sensitizing, lanthanide-doping and synthetic method were employed to explore the correlation between structural features and the charge mobility, to both elucidate the reaction mechanism and the underlying features for the design of an efficiently photo-active heterogeneous catalyst.

The second part of the project involved the design of nanostructured ZnO and TiO_2, with focus on the optical, structural and electro-chemical characterization of the material, which took part at Luleå University of Technology in Luleå, Sweden. Therefore, ZnO and TiO_2 nanorods were first tested in the oxygen evolution reaction (OER) for the photo-driven water splitting process, to provide clues on the oxidizing properties of the materials, and then on the photo-electro-mediated degradation of the organic pollutant methylene blue (MB).

The findings allowed to elucidate the catalytic mechanism and to propose the underlying prerequisites for a more efficient photo-driven conversion of CO_2.

2. Scientific context: a general introduction

1.1 The energetic challenge

Carbon dioxide (CO_2) is the main by-product related to fossil fuel consumption – as well as to other anthropogenic activities – whose atmospheric levels, together with other greenhouse gases (GHG) (figure 1), were found to considerably contribute to the global warming [1, 2].

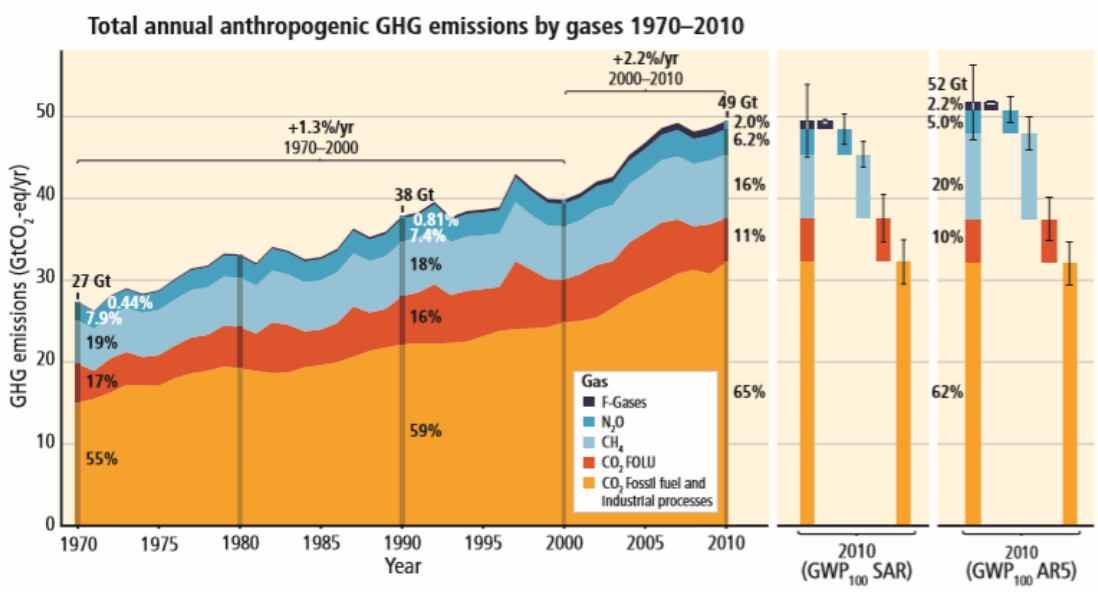

Figure 1 *GHG emission in type by year and type of gas [2]*

The latter process has been observed and identified as a temperature increase concerning the atmosphere and the ocean, with the period between 1983 and 2012 being likely the warmest in 1400 years also interested by a 0.85 ^{o}C increase of the ocean surface temperature (figure 2a) [2]. However, a series of other events were also associated to the global warming, such as ice retreat, sea levels rising (figure 2b), ocean acidification and extreme weather, all of which retained able to directly or indirectly affect both physical, biological and human-related systems and referred to more generally as climate change [2, 3].

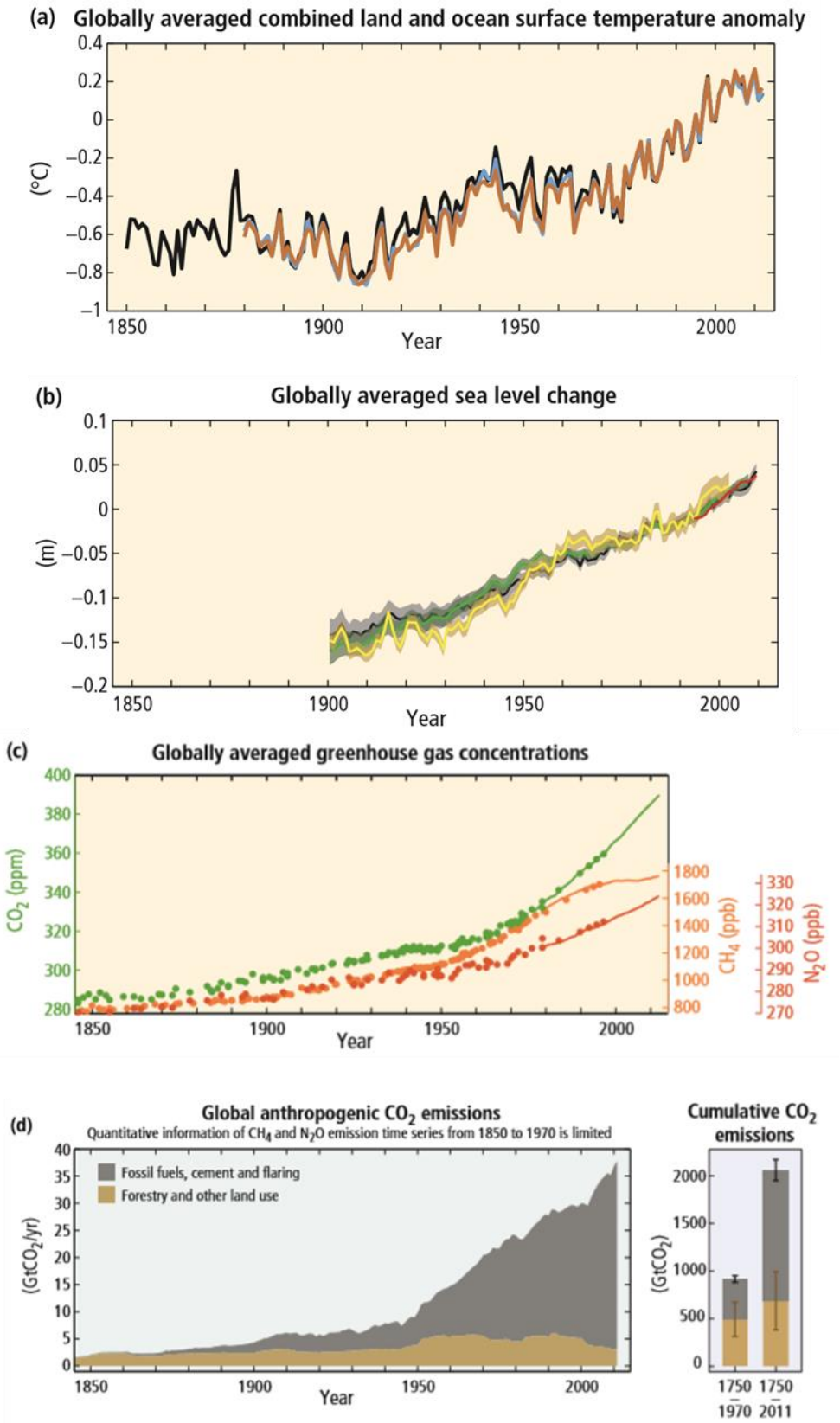

Figure 2 *a) Land and ocean surface temperature increase, b) average sea level, c) GHG and d) CO_2 emissions variation in time [2]*

As one of the outcomes of the fourth assessment report of IPCC (2007) [4] expressed the necessity of a development aiming to a sudden and efficient climate mitigation, the following Special Report

on Renewable Energy Sources and Climate Change Mitigation (SRREN) [5] underlined the utmost role of renewable energy (RE) sources for the achievement of such a goal, together with carbon policies and carbon capture and storage (CCS) technologies [6, 1].

Biomass-derived (bioenergy), direct solar, hydropower, geothermal, ocean and wind energy are the main alternative sources whose combination and employment were proposed to have the technical potential to supply the global energy demand, thereby contributing to the economic and social development with a generally reduced impact on health and environment (figure 3) [6]. The competitivity, investment in and employment of RE has recently shown an increasing trend. However, the technical, societal and economic integration in current energy systems represent a current challenge, and even though technological advancement already provided several opportunities to improve efficiency and cost-effectiveness in electric power systems, other issues such as uncertainty and intermittency of the produced energy remain to be faced [7].

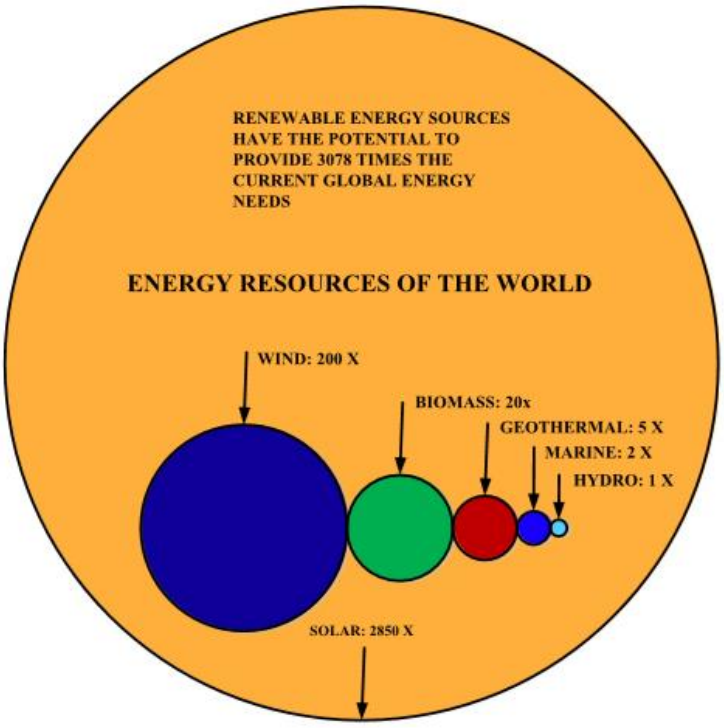

Figure 3 *Global renewable energy sources and their potential [7]*

The power and industry sector are currently responsible of 60% of total CO_2 emission, the latter resulting from fossil fuel combustion. This type of sources defined as “large stationary sources” are those accounting for more than 0.1 $MtCO_2\ yr^{-1}$ and represent a potential opportunity for CO_2 capture and storage or conversion. Conversely, CO_2 emission deriving from the residential and transport sectors is still less likely to be captured due to the very nature of the source [1].

Therefore, considered the present distribution of large stationary emitting source (figure 4) and given an increasing trend for CO_2 emission in the near future [2, 4], the capture of CO_2 not merely represents a necessity in line with the mitigation plan, but also an opportunity if properly coupled to its conversion into high-value and re-usable products. The most relevant factors affecting the outcome of CO_2 capture are the yielded volume, the concentration and the partial pressure of the emission. In this regard, the concentration of CO_2 from fuel combustion is generally less than 15% and a maximum of 30% for metal and cement industries, where chemical transformation is combined with fuel combustion [1],but can reach 100% in chemical industries [8]. For this reason, CO_2 capture may be challenging, presenting different plant- and process-dependent requirements [1].

There are four main type of capture systems namely post-combustion, pre-combustion, oxy-fuel and capture from industrial process streams, which rely on technologies currently consisting in sorbent/solvent separation, membranes, gas liquefaction and distillation, and refrigerated separation [1]. A recent approach aimed to convert the captured CO_2 into energetically valuable, reusable or marketable products such as formic acid/formate ($HCOOH/HCOO^-$), monoxide carbon (CO), formaldehyde (HCHO), methane (CH_4), ethylene (C_2H_4), methanol (CH_3OH) and ethanol (CH_3CH_2O) by mean of an electro- or photo-driven conversion [10]. However, the carbon capture and utilization (CCU) technologies currently employed may also have a considerable energetic demand, generally requiring an additional electric or heat supply [8]. Therefore, the development of a technology able to both capture and directly convert CO_2 into valuable products, may considerably boost the technological implementation of more efficient and convenient CCU systems.

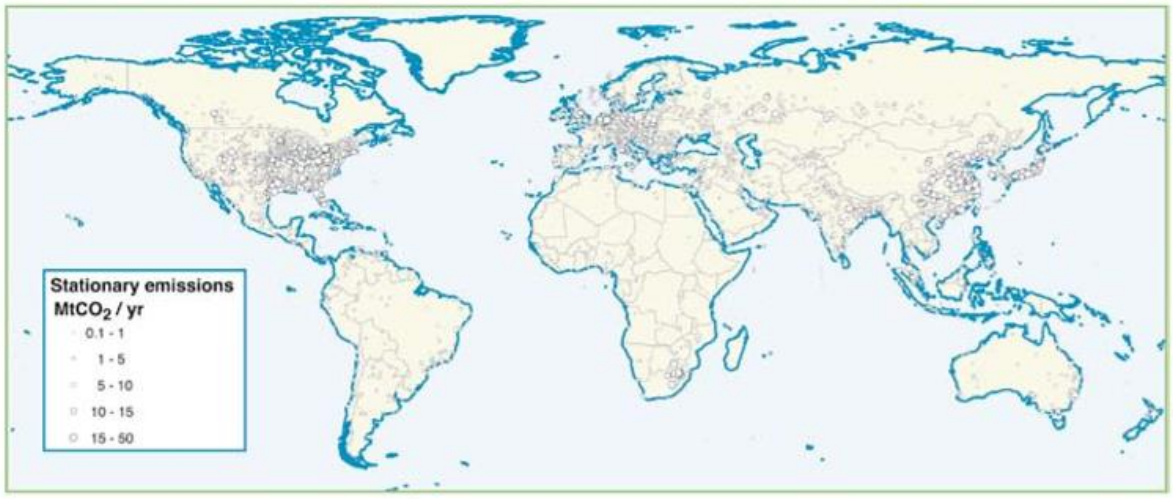

Figure 4 *Global distribution of large stationary emission [1]*

1.2 The photo-driven conversion of CO_2

The CO_2 photoconversion refers to the ability of a semiconductor (SC) to employ the energy of incident photons to form new chemical bonds, in a chemical redox reaction via electrons or holes transfer, eventually resulting in different C-based products and molecular oxygen

$$CO_2 + H_2O \xrightarrow{h\nu} C_xH_yO_z + O_2$$

Equation 1

In fact, when the energy of photons is equal or greater than the semiconductor's bandgap, an electron-hole pair is generated, which can either recombine or transfer to an acceptor molecule, thereby initiating the oxidizing or reducing process [10]. For the reduction process, the conduction band (CB) edge of the catalyst must have a redox potential higher than the one of the lowest unoccupied molecular orbital (LUMO) of the adsorbed molecule. Conversely, oxidation requires the highest occupied molecular orbital (HOMO) of the molecule to have a higher potential than the valence band (VB) of the catalyst [10].

For an effective light-to-chemical conversion the photogeneration step, the charge transfer and migration as well as the surface activity are the main relevant factors able to affect the redox process [11]. Therefore, successful photoconversion relies on the prevalence of the transfer over the recombination process, which may be affected by several factors, such as the electron mobility and the defects density in the material (figure 5) [10].

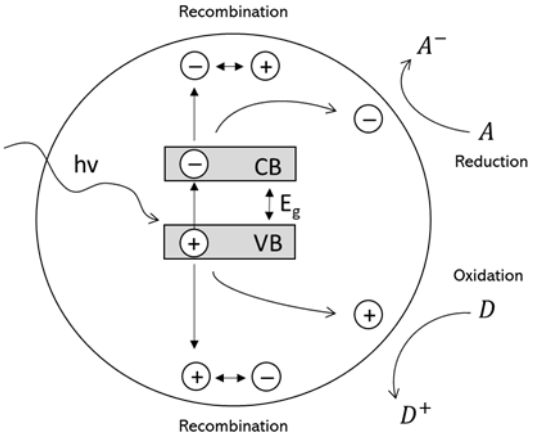

Figure 5 *Electron-hole pair generation and depletion mechanisms.*

In order to improve the charge mobility, by preventing fast recombination of photogenerated electron-hole pairs and promoting surface activation, techniques like (a) crystal facet exposure modification, (b) co-catalyst and (c) another SC coupling have been proposed [11]. The activity of the surface is mainly influenced by the presence of surface electronic states which determines the Fermi energy (E_F) level thereby affecting the adsorption process and therefore the catalytic performance

[11]. Due to the atomic arrangement, the presence of unsaturated atomic coordination numbers, active states and large bond angles, different surface-exposed crystal facets are also likely to result in diverse electronic states resulting in unique adsorption ability and catalytic activity [12]. The role of d-band levels in transition metals was suggested as relevant in the mediation of surface-to-intermediate interaction and the adjustment of the orbital structure was proposed as tool for tuning the product selectivity in the photo-conversion process [13]. Particle size modification was also employed as strategy to modify the surface chemistry as a way to control the crystal plane exposure and the number of active sites, such as corners and edges [14]. Additionally, a SC exposing crystal facets with E_F higher or lower than the bulk, may lead to a preferential charge distribution owed to an internal electric field formation, thereby accounting for charge separation in bare SC [15]. The surface-related defects amount and type were also reported to have a relevant role in both the adsorption of organic molecule [16] and the photocatalytic activity, by means of intra-band states introduction able to affect the charge separation, recombination, transfer and the E_F level [17]. Similarly, coupling of large-band SC with a metal acting as co-catalyst was proposed to promote the charge separation and transfer thereby enhancing the photocatalytic performance [18, 19]. In n-type semiconductors, whose E_F level is near to the CB, the metal-semiconductor interaction results in the transfer of photo-generated electrons from the CB of the SC to the metal (figure 6) and the consequent formation of an inner electric field, which further drives the charge separation process and enhances the SC oxidative potential by increased holes concentration [11].

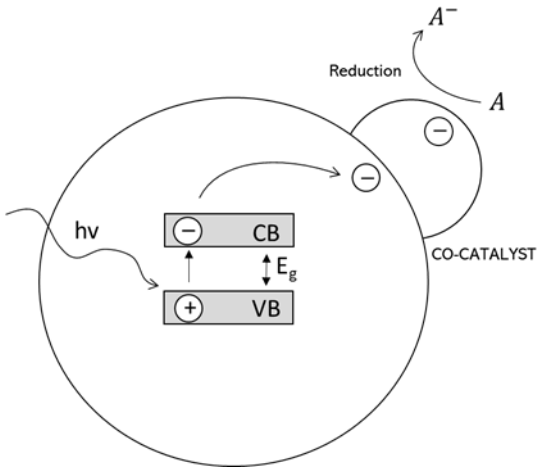

Figure 6 *Electron transfer and consequent reduction mediated by a co-catalyst.*

Four main models were instead proposed to describe a SC-SC junction, such as sensitization, type II, phase junction and Z-scheme. While in the sensitization only one of the interacting SCs is photo-excited, in type II and phase junctions two different light-absorbing SC or SC phases, respectively are involved in the electron-hole pairs photo-generation. In any case the generated electrons and holes transfer occurs between the CBs and VBs respectively, according to their relative positions. In a Z-

Scheme, an electron transfer from the CB of a SC to the VB of another, enhances the oxidative and reducing potential of their respective photo-stimulated VB and CB [11].

The proposed mechanism for CO_2 reduction is the proton coupled electron transfer (PCET), mainly composed by an activation step (I), the de-hydroxylation (II) and the product release step (III), the latter depending on both the molecule-to-catalyst affinity and the reaction conditions (figure 7) [10, 20, 21].

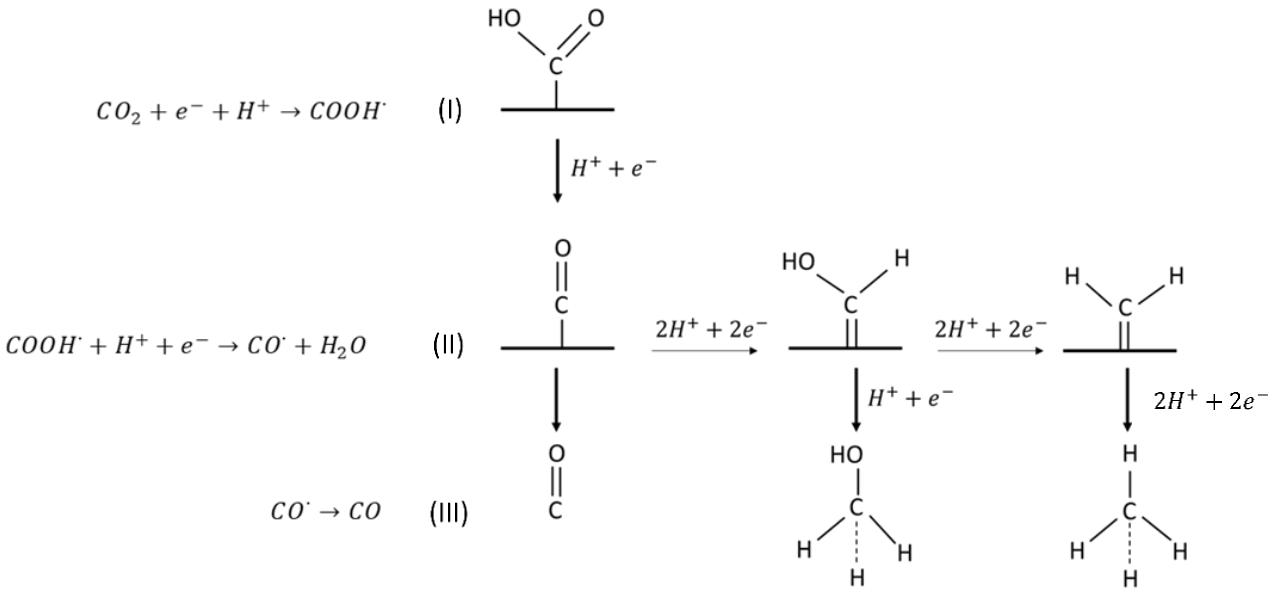

Figure 7 *Proposed reaction steps for (I) CO_2 activation, (II) de-hydroxylation and (III) product release leading to different products such as CO, CH_3OH and CH_4 [2, 3]*

Theoretically, the transfer of 8 electron is necessary to fully convert CO_2 into CH_4 (equation 2, step I) and it is believed that a series of one-step electron transfers with different potential E^0_{Redox} (V vs RHE) are required, with different chemical intermediates leading to the final product (figure 7) (equation 2, step I-IV) [10, 21]

$$CO_2 + 8H^+ + 8e^- \rightarrow CH_4 + 2H_2O \quad E^0_{Redox} = -0.24\,V \quad \text{(I)}$$
$$CO_2 + 6H^+ + 6e^- \rightarrow CH_3OH + H_2O \quad E^0_{Redox} = -0.38\,V \quad \text{(II)}$$
$$CO_2 + 4H^+ + 4e^- \rightarrow HCHO + H_2O \quad E^0_{Redox} = -0.48\,V \quad \text{(III)}$$
$$CO_2 + 2H^+ + 2e^- \rightarrow CO + H_2O \quad E^0_{Redox} = -0.53\,V \quad \text{(IV)}$$

Equation 2

Moreover, an effective photocatalytic system should not only be able to stabilize the less stable intermediates and provide a successful electron transfer, but also to suppress the competitive

reaction of hydrogen formation due to the presence of water in the reaction medium. In fact, the photocatalytic activity of many n-type semiconductors was proposed to mainly rely on oxygen reactive species and radicals formation via water oxidation (equation 3), owed to the higher binding energies of water and oxygen on the SCs surface, although direct electron transfer to CO_2 has also been proposed [22].

$$2H_2O + 4h^+ \rightarrow O_2 + 4H^+ \qquad E^0_{Redox} = 0.82\ V$$

Equation 3

However, for the photoconversion to occur, CO_2 have been postulated to chemisorb to the surface of the semiconductor, thereby competing with the more favourable hydrogen evolution reaction (equation 4) [13], as well as possibly undergoing back oxidation due to the strongly oxidizing environment.

$$2H^+ + 2e^- \rightarrow H_2 \qquad E^0_{Redox} = -0.41\ V$$

Equation 3

The reaction would then occur by bound CO_2 activation, followed by the contemporaneous transfer of an electron and a proton or a hydrogen radical to convert C – O bonds into C – H ones [11].
Three main conversion pathways have been proposed, such as 1) the formaldehyde, 2) the carbene and 3) the glyoxal pathway. Experimental evidence supported role of the hydrophilicity of the catalytic system to obtain either methane or methanol, also according to the relative amount of water in the reaction medium. In fact, the increase in CO_2 availability and solubility, beside the possibility to tune H_2O/CO_2 ratio, mainly yielded methanol and methane in gas phase. The final product selectivity and yield was reported to be dependent on the substrate, the H_2O/CO_2 ratio itself, the hydrophilicity of the system surface, size and presence of both pores and co-catalysts [23]. Two different reaction pathways were proposed in water-based media, either in liquid or gas phase when TiO_2 was used as photocatalyst. At neutral pH, the former favoured a fast hydrogenation and formation of O-containing products such as formic acid, formaldehyde and methanol, while the faster-occurring de-oxygenation in gas phase preferentially lead to methane. Moreover, water presents higher refractive index in liquid phase than in vapour phase (1.34795 and 1.000256 respectively) as well as lower CO_2 solubility, although organic solvents or alkaline solutions were proposed as alternatives, although less sustainable [24]. However, pH, reaction medium composition and phase, temperature as well as intensity of radiation are all relevant parameters able to affect the catalytic performance [10, 24, 25].

Eventually, an efficient photo-conversion by earth-abundant and cost-effective SCs is believed to play a relevant role in the future employment and spread of related technologies contributing to the control of rising CO_2 levels.

1.3 TiO_2 properties and photo-catalytic activity

TiO_2 has been broadly studied for its photocatalytic properties and its ability to convert CO_2 in presence of light as energetic source, due to the UV-excitable broad bandgap with a VB able to oxidize water (+2.94 V vs RHE) and a CB negative enough (-0.16 V vs RHE) to reduce protons [10].

TiO_2 is a cheap, earth-abundant, chemically stable, non-toxic, n-type and indirect band-gap semiconductor with unique scattering properties [26], which is present in four different crystallographic phases, namely rutile (tetragonal), anatase (tetragonal), brookite (orthorhombic) (figure 8a-c) and TiO_2-B (monoclinic) [10].

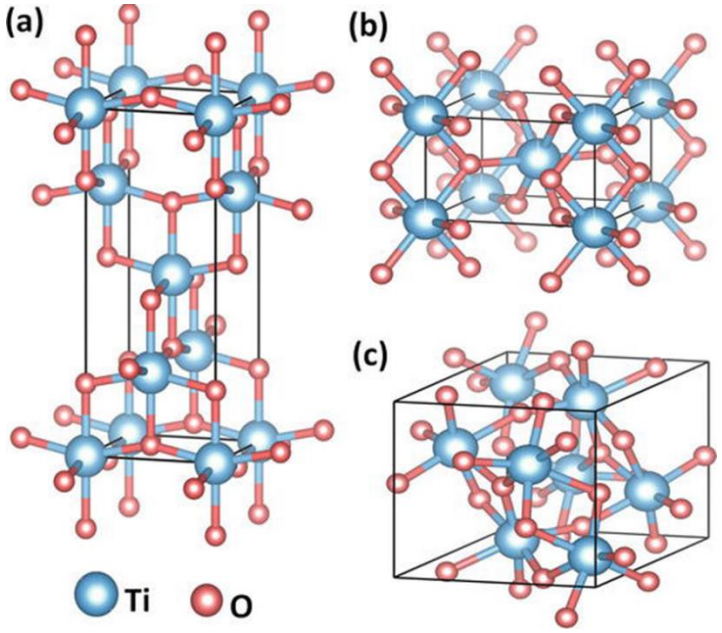

Figure 8 *TiO_2 crystal structure with (a) anatase, (b) rutile and (c) brookite [44].*

TiO_2 is industrially produced by a) the sulphate process, in which Ti-containing raw material reacts with sulfuric acid at 150-220 ^oC, before being further precipitated, purified and heat treated or b) the chloride process, in which the raw material is chlorinated at 700-1200 ^oC to form $TiCl_4$ and oxidized at 900-1400 ^oC to obtain TiO_2 [26]. Although widely employed as white pigment for paints, coating, synthetic fibers, plastics, printing inks, paper brightening and as UV absorber for sun-screening purposes, non-pigmentary TiO_2 is also used as thermally or photochemically-activated catalyst for the decomposition of inorganic and organic water and air pollutants [26], as well as other electrochemical and photovoltaic applications [27].

Rutile and anatase were mostly investigated for the photocatalytic activity, with their structural differences accounting for different bandgaps – ~3.0 eV and ~3.2 eV respectively – thereby resulting in a different energy for inter-band transition, generally occurring at 389 nm and 413 nm wavelength of light of excitation, for anatase and rutile respectively [9]. Thermal stability, recombination rate and charge mobility are also different in the two polymorphs, with anatase showing a lower thermal stability but also a lower recombination rate [9]. Several strategies have been proposed to boost efficiency, such as particle size and shape modification, and to suppress the electron-hole recombination such as dye-sensitizing or co-catalyst coupling [28].

P25 (Evonik) is a widely reported TiO_2-based benchmark, whose dimensions range from 20 to 80 nm, composed by 80% of anatase and 20% of rutile phase. The existence of heterojunction at the phase interface with bandgap differences were entitled as responsible for improved charge mobility and increased photocatalytic performance of the material, currently employed in many photocatalytic experiments [10].

1.4 ZnO properties and potential in photo-catalysis

ZnO is a widespread, non-toxic, earth-abundant direct-bandgap semiconductor currently mostly studied for its piezoelectric and light-emitting properties for optoelectronic applications, due to the wide bandgap (~3.3 eV) and the high exciton binding energy (~ 60 meV) accounting for room and higher temperature intense emission [29]. ZnO is a II-VI semiconductor present in three main structure: cubic rock salt, zinc-blend and hexagonal wurtzite (figure 9a-c), the latter being stable and most commonly growing at atmospheric pressure conditions, with each atom spatially organized as a tetrahedron and binding by turn four other atoms [29].

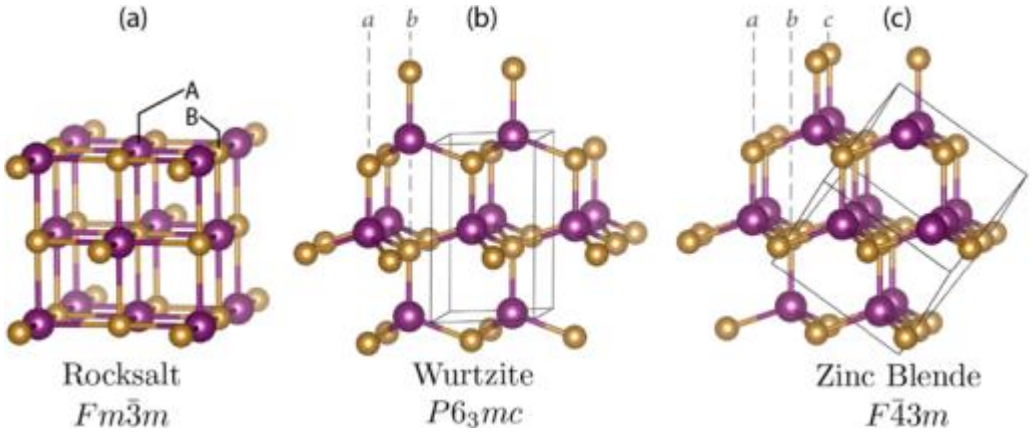

Figure 9 *ZnO crystal structures as (a) rocksalt, (b) wurtzite and zinc blend [45].*

Although well known as "cadmia" since the Roman Empire, ZnO has been extensively employed as white pigment and in the rubber, coating, pharmaceutical, ceramic and catalytic industry after the industrialization of its production, which nowadays mainly occurs by either a wet (1-2%), a direct (10-20%) or an indirect process [26]. The direct process consists in the coal-mediated Zn reduction at 1000-1200 ^{o}C from a zinc-containing material, vaporization and its further oxidation to yield ZnO and CO_2 [26]. In the indirect process, metallic Zn is vaporized and oxidized upon air combustion, while in the wet process ZnO is obtained by precipitation of zinc sulphate or chloride solutions, which is then filtered and calcinated [26]. While abundancy and availability of low-cost synthetic techniques ZnO further competitive, its absorption in the near-UV region with a highly oxidizing VB, p- and n-like semiconductor tuneable properties also suggested its potential application in photo-promoted reactions and energy harvesting technologies [30].

Due to a bandgap similar to the one of TiO_2 and a VB able to oxidize water, ZnO was proposed as candidate for CO_2 photoconversion for methane production in presence of water. In fact, the VB redox potential for ZnO was reported as ~3.0 V (vs RHE), enough positive to produce $OH^{\bullet}$ radicals by water oxidation (XI) and with a CB value of nearly -0.2 V (vs RHE), as well able to reduce protons or oxygen (X) [31]. However, the role of ZnO as a promising photocatalyst is currently mainly limited by a) photo-corrosion upon UV-light exposure (equation 5) and b) absorption in only the UV region of the sun light spectrum [30].

$$ZnO + 2h^{+} \rightarrow Zn^{2+} + 1/2\, O_2$$

Equation 5

Furthermore, factors such as morphology and phase crystallinity have been reported as relevant for ZnO photocatalytic activity, even more than the BET specific surface [32]. In accordance with the more likely oxidizing properties, ZnO have been mainly employed for photo-driven oxidative reactions, such as pollutants or dye degradation in water [30].

1.5 CeO_2 in photo-catalysis

Cerium is the most abundant rare-earth element, of which nearly 50% of the raw material consist of cerium oxide [33], mainly present as CeO_2 with a cubic fluorite and Ce_2O_3 with a hexagonal structure (figure 10) [34].

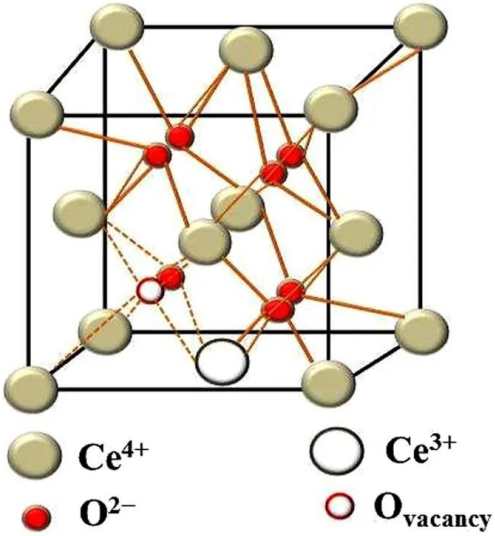

Figure 10 *CeO_2 structure of both hexagonal Ce(III) and cubic fuorite Ce(IV) [46].*

Separation of the oxide from other rare-earth, in cerium-containing raw materials like monazite and bastnaesite, occurs by oxidation of solutions and further precipitation of Ce(IV) [33]. CeO_2 is mainly used as polishing agent and glass constituent [33], although the co-existence of Ce^{3+} and Ce^{4+} oxidation states in the same material has been reported and related to the ability of oxygen storage according to its chemical potential [35], with Ce^{3+} states being mainly localized at the surface [36], thereby suggesting many other applications. The band gap of bulk CeO_2 was reported to be ~3.2 eV, for which the O-2p to Ce-4f transition accounts, and to increase by decreasing the particle size, due to both a quantum confinement and to a cluster effect [36]. However, the band gap was elsewhere reported as ~2.8 eV and potentially related to the stoichiometric ratio between CeO_2 and Ce_2O_3 oxides [37].

CeO_2 reducibility is often reported to occur at high temperatures and its thermo-catalytic potential has been already exploited for H_2O and CO_2 reduction for H_2 and CO production, which was also proved to depend on the material morphology [38]. Moreover, CeO_2-mediated H_2 production has been proposed in a two-step process by thermal solar-induced reduction of Ce(IV) to Ce(III) (T=2000 ^oC) followed by hydrolysis as the regeneration step (T=400-600 ^oC) [39], although CeO_2 decreased particle size has been suggested to have higher reducibility than its bulk counterpart [40].

The introduction of Ce in TiO_2 or ZnO-based materials, to form CeO_2-TiO_2 or CeO_2-ZnO mixed oxides composites, was shown to reduce the bandgap thereby promoting a visible light-induced photocatalysis of organic compounds, the latter also depending on Ce/Ti and Ce/Zn molar ratios [41, 42]. Eventually, the identification of adsorbed CO_2 on surface of CeO_2-ZnO [37] as well as the decreased acidity of CeO_2-TiO_2 composite, supported by NH_3-TPD experiments [43], suggested the potential application of both materials for CO_2 adsorption and storage.

1.6 Aim of the study

As an answer to the modern environmental concerns, a series of nanostructured materials were tested for the photocatalytic conversion of CO_2 into CH_4.

The following project aimed to test and compare the photo-induced CO_2 conversion efficiency of two earth-abundant metal oxides, such as TiO_2 and ZnO, in gas phase, mild temperature and pressure conditions, and can be divided in two different parts.

In the first part, the ability of different ZnO-based samples as effective CO_2 photocatalysts under UV illumination and their physical, optical and structural properties were investigated and compared to P25, used as standard.

Introduction of co-catalysts and the shape modification aimed to improve ZnO photoconversion efficiency, while the effect of silica-based scaffold on P25 photo-activity was also estimated. The addition of CeO_2 to form Zn-Ce and Ti-Ce mixed oxides aimed to modify the bandgap and improve the visible light harvesting.

The second part mainly focused on the study of the stability, ability to oxidize water and/or organic pollutants by means of PC experiments and PEC characterization, in order to understand the possible exploitation of nanostructured ZnO-based materials for photo-electro-catalytic purposes. Again, Ce-Ti, Ce-Zn and Zn-Ti systems were prepared starting from one-dimensional (1D) ZnO and TiO_2-based nanorods, to explore the effect of different synthetic method, deposition techniques, shape and facet exposure in the OER of the water splitting process, to investigate their potential ability in the water oxidation as one of the possible mechanisms driving the CO_2 light-mediated conversion.

Overall, the present project explored the range of available techniques and their role in the promotion of the SC-mediated light-to-chemical conversion of CO_2 into marketable products or in OER of the water-splitting process.

1.7 Bibliography

[1] Metz, B., O. Davidson, H. C. de Coninck, M. Loos, and L. A. Meyer, *IPCC, 2005: IPCC Special Report on Carbon Dioxide Capture and Storage. Prepared by Working Group III of the Intergovernmental Panel on Climate Change.* Cambridge University Press, Cambridge, United Kingdom and NewYork, NY, USA, Ch. 2(77-84), Ch. 3(108-110)

[2] R.K. Pachauri and L.A. Meyer, *IPCC, 2014*: *Climate Change 2014: Synthesis Report. Contribution of Working Groups I, II and III to the Fifth Assessment Report of the Intergovernmental Panel on Climate Change*, IPCC, Geneva, Switzerland, (2014)

[3] J. M. Melillo, T. V. Callaghan, F. I. Woodward, E. Salati, S. K. Sinha, *IPCC, 1990: Climate change 1990, IPCC Scientific assessment. Effect on Ecosystems, Ch. 10, 289-306*

[4] B. Metz, O.R. Davidson, P.R. Bosch, R. Dave, L.A. Meyer, *IPCC, 2007: Climate Change 2007: Mitigation. Contribution of Working Group III to the Fourth Assessment Report of the Intergovernmental Panel on Climate Change*, Cambridge University Press, Cambridge, United Kingdom and New York, NY, USA., XXX

[5] O. Edenhofer, R. Pichs-Madruga, Y. Sokona, K. Seyboth, P. Matschoss, S. Kadner, T. Zwickel, P. Eickemeier, G. Hansen, S. Schlömer, C. von Stechow. *IPCC, 2011: IPCC Special Report on Renewable Energy Sources and Climate Change Mitigation: Summary for Policymakers*, Cambridge University Press, Cambridge, United Kingdom and New York, NY, US, (2011)

[6] M. Hoel, S. Kverndokk, *Depletion of fossil fuels and the impacts of global warming*, Resource and Energy Economics (1996), 18, 115-136

[7] Omar Ellabbana,b,n, Haitham Abu-Rubb, Frede Blaabjerg, *Renewable energy resources: Current status, future prospects and their enabling technology,* Renewable and Sustainable Energy Reviews, (2014) 39, 748–764

[8] N. von der Assen, L. J. Müller, A. Steingrube, P. Voll and A. Bardo, *Selecting CO_2 Sources for CO_2 Utilization by Environmental-Merit-Order Curves,* Environ. Sci. Technol. (2016) 50(3), 1093-1101

[9] W. Zhang, Y. Hu, L. Ma, G. Zhu, Y. Wang, X. Xue, R. Chen, S. Yang and Z. Jin, *Progress and Perspective of Electrocatalytic CO_2 Reduction for Renewable Carbonaceous Fuels and Chemicals,* Adv. Sci. (2018) 5, 1700275, 1-24

[10] Severin N. Habisreutinger, Lukas Schmidt-Mende and Jacek K. Stolarczyk, *Photocatalytic Reduction of CO_2 on TiO_2 and Other Semiconductors*, Angew. Chem. Int. Ed. (2013) 52, 7372–7408

[11] S. Bai, J. Jiang, Q. Zhang and Y. Xion, *Steering charge kinetics in photocatalysis: intersection of materials syntheses, characterization techniques and theoretical simulations*, Chem. Soc. Rev. (2015) 44, 2893--2939

[12] W.-J. Ong, L.-L. Tan, S.-P. Chai, S.-T. Yong and A. R. Mohamed, *Facet-Dependent Photocatalytic Properties of TiO2-Based Composites for Energy Conversion and Environmental Remediation,* Chem. Sus. Chem. (2014) 7, 690–719

[13] J. Greeley, J. K. Nørskov, and Manos Mavrikakis, Electronic structure and catalysis on metal surfaces, Annual Review of Physical Chemistry (2002) 53, 319-348

[14] E. M. Andrews, J. Flake and Y. Fang, *CO_2 Electrocatalytic Reduction at Gold and Copper Electrodes: Role of Particle Size and Surface Chemistry*, ECS Transactions (2015) 66, 22(3)

[15] C.-S. Tan, S.-C. Hsu, W.-H. Ke, L.-J. Chen and M. H. Huang, *Facet-Dependent Electrical Conductivity Properties of Cu2O Crystals,* Nano Lett. (2015) 15(3), 2155-2160

[16] F. Liu, Y. H. Leung, A. B. Djurišić, A. M. Ching Ng and W. K. Chan, *Native Defects in ZnO: Effect on Dye Adsorption and Photocatalytic Degradation*, J. Phys. Chem. C (2013) 117, 12218−12228

[17] Defect and its dominance in ZnO films: a new insight into the role of defects over photocatalytic activity, Applied Catalysis B: Environmental (2013) 142-143, 736-743

[18] V. Subramanian, E. E. Wolf and P. V. Kamat, *Catalysis with TiO_2/Gold Nanocomposites. Effect of Metal Particle Size on the Fermi Level Equilibration*, Am. Chem. Soc. (2004) 126(15), 4943-4950

[19] A. Tanaka, K. Hashimoto and H. Kominami, *Visible-Light-Induced Hydrogen and Oxygen Formation over Pt/Au/WO_3 Photocatalyst Utilizing Two Types of Photoabsorption Due to Surface Plasmon Resonance and Band-Gap Excitation*, Am. Chem. Soc. (2014) 136(2), 586-589

[20] A. Li, T. Wang, X. Chang, Z.-J. Zhao, C. Li, Z. Huang, P/ Yang, G. Zhou and J. Gong, *Tunable syngas production from photocatalytic CO_2 reduction with mitigated charge recombination driven by spatially separated cocatalyst*, Chem. Sci., 2018,9, 5334–5340

[21] L. Liu and Y. Li, *Understanding the Reaction Mechanism of Photocatalytic Reduction of CO_2 with H_2O on TiO_2-Based Photocatalysts: A Review*, Aerosol and Air Quality Research, (2014) 14, 453–469

[22] B. Han, J. Wang, C. Yan, Y. Dong, Y. Xu, R. Nie, H. Jing, *The photoelectrocatalytic CO_2 reduction on TiO_2@ZnO heterojunction by tuning the conduction band potential*, Electrochimica Acta (2018), doi: 10.1016/j.electacta.2018.07.216

[23] M. Fu, Y. Li, S. Wu, P. Lu, J. Liu, F. Dong, *Sol-gel preparation and enhance photocatalytic performance of Cu-doped ZnO nanoparticles*, Applied Surface Science (2011) 268, 1587-1591

[24] A. Olivo, E. Ghedini, M. Signoretto, M. Compagnoni and I. Rossetti*, Liquid vs. Gas Phase CO_2 Photoreduction Process: Which Is the Effect of the Reaction Medium?* Energies (2017) 10, 1394, 1-14

[25] A. Olivo, W. A. Thompson, E. R. B. Bay, Elena Ghedini, F. Menegazzo, M. Maroto-Valer and M. Signoretto, *Investigation of process parameters assessment via design of experiments for CO_2 photoreduction in two photoreactors*, Journal of CO2 Utilization (2020) 36, 25-32

[26] G. Auer, P. Woditsch, A. Westerhaus, J. KischkewitZ, W.-D. Griebler, M. De Liedekerke, *Pigments, Inorganic, 2. White Pigments*, Wiley-VCH Verlag GmbH & Co. KGaA, (2012) 27, 257-289

[27] M. Ni, M. K. H. Leung, D. Y. C. Leung and K. Sumathy, *A Review and recent developments on photocatalytic water-splitting using TiO_2 for hydrogen production*, Renewable and Sustainable Energy Reviews (2007) 11, 401–425

[28] Lianjun Liu, Ying Li, *Understanding the Reaction Mechanism of Photocatalytic Reduction of CO_2 with H_2O on TiO_2-Based Photocatalysts: A Review*, Aerosol and Air Quality Research, 14: 453–469, 2014

[29] Ü. Özgür, Ya. I. Alivov, C. Liu, A. Teke, M. A. Reshchikov, S. Doğan, V. Avrutin, S.-J. Cho, and H. Morkoç, *A comprehensive review of ZnO materials and devices*, J. Appl. Phys. (2005) 98, 041301

[30] Y. Li, W. Xie, X. Hu, G. Shen, X. Zhou, Y. Xiang, X. Zhao and P. Fan, *Comparison of Dye Photodegradation and its Coupling with Light-to-Electricity Conversion over TiO_2 and ZnO*, Langmuir (2010) 26(1), 591–597

[31] S. Wang, B. Zhu, M. Liu, L. Zhang, J. Yu, M. Zhou, *Direct Z-scheme ZnO/CdS hierarchical photocatalyst for enhanced photocatalytic H_2-production activity*, Applied Catalysis B: Environmental (2018)

[32] D. Li, H. Haneda, *Morphologies of zinc oxide particles and their effects on photocatalysis*, Chemosphere (2003), 51, 129–137

[33] K. Reinhardt and H. Winkler, Cerium Mischmetal, *Cerium Alloys, and Cerium Compounds*, Wiley-VCH Verlag GmbH & Co. KGaA, (2012) 8, 41-54

[34] H. Abdullah, M. R. Khan, M. Pudukudy, Z. Yaakob, N. A. Ismail, *CeO_2-TiO_2 as a visible light active catalyst for the photoreduction of CO2 to methanol*, Journal Of Rare Earths (2015) 33(11), 1155-1161

[35] N. V. Skorodumova, R. Ahujia, S. I. Simak, I. A. Abrikosov, B. Johansson and B. I. Lundqvist, *Electronic, bonding and optical properties of CeO_2 and Ce_2O_3 from first principle*, Physical Review B, (2001) 64(115108), 1-9

[36] S. Tsunekawa, J.-T. Wang and Y. Kawazoe, *Lattice constant and electron gap energies of nano- and subnano-sized cerium oxides from the experiments and from first-principles calculation*, Journal of Alloys and Compounds (2006) 408–412, 1145–1148

[37] E. D. Sherly, J. J. Vijaya and L. J. Kennedy, *Effect of the CeO_2 coupling on the structural, optical photocatalytic properties of ZnO nanoparticles*, Journal of Molecular Structure (2015) 1099, 114-125

[38] L. J. Venstrom, N. Petkovich, S. Rudisill, J. H. Davidson, The Effects of Morphology on the Oxidation of Ceria by Water and Carbon Dioxide, Journal of Solar Energy Engineering (2012) 134(011005), 1-8

[39] S. Abanades and G. Flamant, *Thermochemical hydrogen production in a two-step solar-driven water-splitting cycle based on cerium oxide*, Solar Energy (2006) 80, 1611–1623

[40] S. Kundu, J. Ciston, S. D. Senanayake, D. A. Arena, E. Fujita, D. Stacchiola, L. Barrio, R. M. Navarro, J. L. G. Fierro, and J. A. Rodriguez, *Exploring the Structural and Electronic Properties of Pt/Ceria Modified TiO2 and Its Photocatalytic Activity for Water Splitting under Visible Light*, J. Phys. Chem. C (2012) 116, 14062−14070

[41] A. M. T. Silva, C. G. Silva, G. Drazic, J. L. Faria, *Ce-doped TiO_2 for photocatalytic degradation of chlorophenol*, Catalysis Today (2009) 144, 13–18

[42] S. Rajendran, M. M. Khan, F. Gracia, J. Qin, V. K. Gupta and S. Arumainathan, *Ce^{3+}-ion-induced visible-light photocatalytic degradation and electrochemical activity of ZnO/CeO_2 nanocomposite*, Scientific Reports (2016) 6(31641), 1-11

[43] S. Watanabe, X. Ma, and C. Song, *Characterization of Structural and Surface Properties of Nanocrystalline TiO_2-CeO_2 Mixed Oxides by XRD, XPS, TPR, and TPD*, J. Phys. Chem. C (2009) 113, 14249–14257

[44] H. Siddiqui, *Modification of Physical and Chemical Properties of Titanium Dioxide (TiO2) by Ion Implantation for Dye Sensitized Solar Cells,* Intech. Open, DOI: 10.5772/intechopen.83566

[45] P. V. Balachandran, J. Theiler, J. M. Rondinelli, T. Lookman *Material prediction via classification learning,* NIH: PubMed Sci. Rep. (2015), http://creativecommons.org/licenses/by/4.0/

[46] Khan, M.E., Khan, M.M. & Cho, M.H. *Ce^{3+}-ion, Surface Oxygen Vacancy, and Visible Light-induced Photocatalytic Dye Degradation and Photocapacitive Performance of CeO_2-Graphene Nanostructures*, Sci. Rep. (2017) 7, 5928. https://doi.org/10.1038/s41598-017-06139-6

Chapter 1

Strategies for increased photo-stability and photo-catalytic conversion CO_2 of nano-sized semiconductors

1. Introduction

Since more than two decades, large band gap semiconductors (SC) such as ZnO and TiO_2 has been proposed as effective photocatalyst and their employment as an environmentally acceptable alternative for the light-mediated treatment of liquid and gaseous pollutants [1], as well as in CO_2 photo-conversion [2].

SC have attracted much attention, as possessing an energy bandgap within the range of the energy of UV-visible light although often coupled with metal co-catalyst, in order to decrease the recombination probability [3] and to improve the reduction by mean of direct electron transfer to the acceptor molecule [4]. Scaffolding [5] and metal coupling [4], together with size, shape, crystal phase, presence of active sites and external orbital structure of the catalyst were also reported as relevant features to improve the yield and selectivity of the photo-driven conversion, thereby affecting the intermediates stabilization on the surface [6, 7]. Common attempts to modify a SC bandgap width and structure in semiconductors consists in a) doping, such as N or non-metal doping, b) introduction of hybridized orbitals by metals, c) creation of impurity states by mean of oxygen vacancies states, d) coupling of a SC with narrower bandgap and d) introduction of heterojunctions, all approaches aiming to shorten the bandgap or introduce intermediate intra-gap states for a more effective electron transfer [2, 8] as well as to improve the light-harvesting process [9]. Attempts to increase the TiO_2 performance in CO_2 photo-conversion included metal loading, such as Cu, Au, Ag, Ru and Pd, scaffolding such as SiO_2, kaolin and zeolites [10], dye sensitizing, as well as size and shape modulation [2]. For instance, introduction of CuO in nanosized TiO_2 has been reported as able to effectively increase CH_4 production (23.0 $\mu mol \cdot g_{cat}$) and CO_2 selectivity by 98%, while Au coupling both lead to CH_4 and H_2 production (15.0 and 10.0 $\mu mol \cdot g_{cat}$) in mild conditions, underlining the uttermost relevance of surface composition and properties for product selectivity [11]. Increased charge separation in Ti-O-Si bonds and modified hydrophilicity in TiO_2/SiO_2 systems were also suggested as relevant factors for the increased performance in the composites. The pore size and shape of the scaffolding material was experimentally related to both product selectivity and catalytic performance modulation [12]. Anatase TiO_2 nanorods and nanotubes showed increased CO_2 photoconversion with respect to anatase nanoparticles, further boosted by Pt

nanoparticles decoration [13]. Similarly, the introduction of a metal co-catalysts, such as Au and Ag, on the surface of ZnO nanoflowers was also reported to promote the photocatalytic activity in visible light conditions by a proposed charged separation improvement and consequent delayed recombination, underlining the fundamental role of holes in the degradation of phenols and MB in water [14]. In a similar context, dye sensitizing was reported to promote the catalysis also under visible light condition, while low-content surface TiO_2 loading was suggested to overall decrease photo-corrosion and improve ZnO photocatalytic performance [15]. Moreover, Cu-doped ZnO nanostructures showed an increased photocatalytic activity, a visible light absorption and a modified crystal structure in dependence with the amount of the doping material and the synthetic conditions, remarking the importance of both shape and crystallinity in ZnO-based photocatalysis [16, 17]. Eventually, the different facets exposure and morphologies of ZnO nanoplates, nanorods and nanowires, were reported to also differ in the photocatalytic activity [18] and to possess unique chemical, optical and physical properties [19]. Therefore, various synthetic methods have been employed to modify shape, facets exposure, or aspect ratio in case of nanorods, as additional tool to modulate surface defects, activity and the photocatalytic performance [20, 21, 22, 23]. While thermal evaporation, chemical vapour deposition (CVD), vapor-liquid-solid (VLS) and other chemical synthetic methods, such as inverse-micelles and sol-gel were widely reported for the synthesis of ZnO nanorods [19], the hydrothermal route was proposed as cost-effective and low temperature template-mediated alternative [24]. The method consisted in a surfactant-assisted precipitation of Zn precursor, followed by a constant-temperature and pressure aging procedure. Parameters like aging temperature, pressure, surfactant and precursors employed, as well as pH of the reaction were all recognised as effective modulators of rods size and shape [25]. The use of poly-vinyl-pyrrolidone (PVP) as surfactant agent in water-based medium was reported for the preparation of stable mono-dimensional ZnO nanostructures [25, 26]. The capping mechanism proposed suggested the PVP-mediated stabilization of the *(100)* plane growth of ZnO wurtzite, with the consequent growth in the (*001)* and (*00-1)* directions [26].

The introduction of CeO_2 in ZnO-based micro-sized materials was reported to increase the surface area, affect the porosity, crystallinity and bandgap of CeO_2-ZnO composites, proportional to the amount of Ce [27]. Notably, a shift of UV-to-visible absorption with respect to bare CeO_2 or ZnO was detected and attributed to the narrowing of the bandgap in CeO_2-ZnO mixed materials [45]. Furthermore, the Ce-dependent increased photocatalytic activity, as well as the decreased temperature necessary for a complete oxidation of CO by CeO_2-ZnO composites, was attributed to

an enhanced charge transfer due to the co-existence of Ce^{4+} and Ce^{3+} states and the presence of a not fully oxidized surface [27]. Similarly, ZnO nanoflowers decorated with CeO_2 and nanoparticles obtained by wet chemical and hydrothermal method respectively, were reported to have enhanced photocatalytic properties under both UV and visible light excitation, compared to bare ZnO and CeO_2 [28, 29]. Both semiconductors bandgaps were calculated as 3.13 eV and 2.86 eV for ZnO and CeO_2 respectively, and a photoinduced charge transfer was proposed to occur by two possible methods, namely type II semiconductor heterojunction or Z-scheme [28, 29]. CeO_2-ZnO nano-catalysts with different atomic ratio obtained by a co-precipitation method were tested for wastewater treatment of several organic and chlorine-containing compounds, showing different removal percentage depending on temperature and optimal atomic ratio [30]. Importantly, the presence of both Ce oxidation states Ce^{4+} and Ce^{3+} were suggested to have a role in modulating oxygen vacancies levels during the photocatalytic process [30].

Visible-light irradiation of 2% CeO_2 loaded on TiO_2 resulted in the increased photoconversion of CO_2 into methanol in a 0.1 M NaOH solution, when compared to bare TiO_2, which was attributed to an electron transfer from CeO_2 CB to the one of TiO_2 [31]. A similar interparticle electron transfer process (IETP) has been proposed for CeO_2-ZnO composites prepared via microwave assisted combustion synthesis, which showed decreased crystallite size, reduced calculated band gap, reduced PL emission and improved UV and visible light-mediated photodegradation of 2,4-dichlorophenol, compared to bare ZnO and CeO_2 [32].

In this study, the effect of crystallinity and defect content on the photo-catalytic efficiency has been investigated by comparing ZnO-based nano-structured materials treated with different annealing temperatures. The loading of small amounts of TiO_2 attempted to improve ZnO photo-stability upon UV-light illumination, while ZnO coupling with metals such as Cu and Ag aimed to insight the effect of a co-catalyst in the photo-catalytic performance.

The role of silica-based scaffolds with different physical properties to boost TiO_2 photo-activity in mild temperature and pressure conditions, was evaluated by loading P25 on either a commercial SiO_2 or a mesoporous SBA-15-based substrate. The introduction of Cerium in Zn and Ti-based materials via co-precipitation chemical route aimed to investigate the type of SC-SC interaction and its role in the CO_2 photo-conversion by increased visible light harvesting.

2. Materials and Methods

2.1. Synthetic Methods

2.1.1. ZnO-based materials

2.1.1.1. Reagents

- Zinc sulphate, $ZnSO_4$ Sigma-Aldrich
- Sodium carbonate, Na_2CO_3 Sigma-Aldrich
- Sodium hydroxide, NaOH Sigma-Aldrich
- Titanium isopropoxide, $Ti(OC_3H_8)_4$ Sigma Aldrich
- Distilled water

2.1.1.2. Procedure

All the ZnO-based materials had been previously synthesized via wet chemistry precipitation method, by using $ZnSO_4$ as precursor and Na_2CO_3 as precipitating agent.

In detail, 1.1 M $ZnSO_4$ was precipitated with 1.0 M Na_2CO_3 solution in a round-bottom flask and aged at 60 ^oC for 20 h. The as prepared compounds were filtered, washed with deionized water, air-dried at 110 ^oC for 18 h and eventually exposed to two different air annealing at either 400 ^oC or 600 ^oC for 4 h and with a 2 ^oC/min ramp. Samples were 4CSZ and 6CSZ respectively. The Ti-modified sample was prepared by wetness impregnation using 1% molar $Ti(OC_3H_8)_4$ dissolved in isopropyl alcohol on 4CSZ, followed by a mild air annealing at 400 ^oC for 1 h. The sample was labelled T4CSZ.

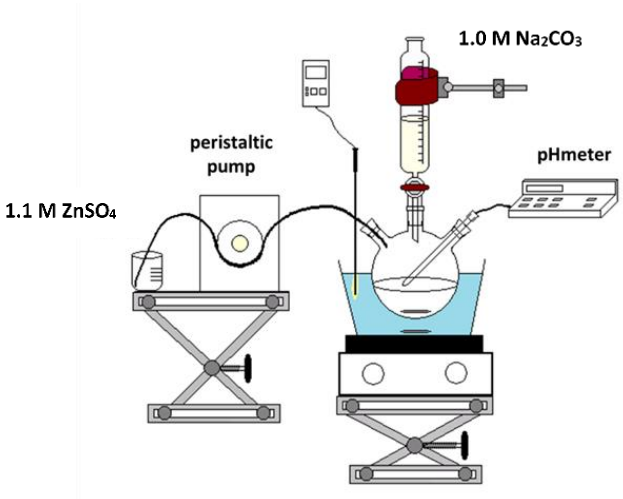

Figure 11 *Laboratory precipitation rig*

2.1.2. Preparation of SiO_2-supported P25 via impregnation method

2.1.2.1. Reagents

- P25, TiO_2 Evonik
- Isopropyl alcohol, C_3H_7OH Sigma-Aldrich
- Silicon dioxide, SiO_2 Sigma Aldrich
- SBA-15

2.1.2.2. Procedure

A dry impregnation method was employed to decorate either commercial SiO_2 or meso-porous SBA-15 with 10% weight of P25. Therefore, 0.2 g of P25 dispersed in 2 mL of isopropyl alcohol were drop-to-drop poured on 2 g of SiO_2 in a large-bottom beaker (crystallizer). The resultant compound was dried for 18 h at 110 ^oC. Commercial SiO_2 and meso-porous SBA-15 samples obtained were named SCP10 and SBP10.

2.1.3. Hydrothermal synthesis of ZnO

2.1.3.1. Reagents

- Zinc nitrate hexahydrate, $Zn(NO_3)_2 \cdot 6H_2O$ Sigma Aldrich
- Polyvinylpirrolidone, PVP $(C_6H_9NO)_n$ (M_W=40000 g·mol-1) Sigma-Aldrich
- Sodium hydroxide, NaOH Sigma-Aldrich
- Distilled water

2.1.3.2. Procedure

Hydrothermal method was used to synthesize ZnO by preparing 200 mL of 0.2 M $Zn(NO_3)_2 \cdot 6H_2O$ aqueous solution, under constant stirring conditions at 700 rpm. After complete dissolution, 14.2 g of polyvinylpyrrolidone (PVP) were added and the solution was further stirred for 40 minutes at room temperature. By mean of a peristaltic pump, 50 mL of a 0.5 M NaOH solution was then added to the mixture, while the pH was adjusted to 10 with a 10 M NaOH. The mixture was left stirring at 400 rpm at room temperature for 3 h and then poured into a Teflon tube and sealed for the aging procedure which occurred into a glycol bath at 60 ^oC for 18 h. The whitish solution was filtered and washed three times with distilled water. The as obtained compound was dried at 60 ^oC for 18 h, air annealed at 400 ^oC for 4 h with 2 ^oC/min ramp and labelled 4PNZ.

2.1.4. Loading of Cu and Ag metals on ZnO-based materials

2.1.4.1. Reagents

- Copper nitrate trihydrate, $Cu(NO_3)_2 \cdot 3H_2O$ Sigma-Aldrich
- Silver nitrate, $AgNO_3$ Sigma-Aldrich
- Distilled water

2.1.4.2. Procedure

The dry impregnation method was used to load either Ag or Cu in 0.1% mol or both Ag and Cu in 0.05%:0.05% mol on 4CSZ. Therefore, the appropriate quantities of $Cu(NO_3)_2 \cdot 3H_2O$ and of $AgNO_3$ were dissolved, together or individually, in 2.5 mL of deionized water and added drop by drop to 4CSZ in a crystallizer. The as prepared powders were air dried at 110 ^oC for 18 h and labelled Ag4CSZ, Cu4CSZ and AgCu4CSZ.

2.1.5. Synthesis of Ce-containing ZnO and Ce-containing TiO_2 composites

2.1.5.1. Reagents

- Zinc nitrate hexahydrate, $Zn(NO_3) \cdot 6H_2O$ Sigma Aldrich
- Ammonium Cerium(IV) nitrate, $Ce(NO_3)_6(NH_4)_2$ Sigma Aldrich
- Sodium hydroxide, NaOH Sigma-Aldrich
- Sodium carbonate, Na_2CO_3 Sigma-Aldrich
- Distilled water

2.1.5.2. Procedure

A 0.5 M of $Zn(NO_3) \cdot 6H_2O$ and of $Ce(NO_3)_6(NH_4)_2$ solution was prepared in 100 mL of distilled water, in order to obtain a 20% mol Ce-80% mol Zn composite. By means of a peristaltic pump, the solution was progressively added to 200 mL of distilled water together with the continuous introduction by Pasteur pipette of a 1 M Na_2CO_3 solution, to stabilize the pH at 9. The white-yellowish solution was then moved into a round-bottom flask and aged under continuous stirring (500 rpm) for 20 h at 60 ^oC. The compound was filtered and washed three times with distilled water and dried for 18 h at 110 ^oC. Therefore, the sample was heat-treated at 400 ^oC for 4 h with 2 ^oC/min ramp and labelled CCZ20. With a similar procedure a 20% mol Ce-80% mol Ti composite was prepared, starting from a

0.4 M of $TiO(SO_4)\cdot x(H_2O)$ and $Ce(NO_3)_6(NH_4)_2$ aqueous solution and using a 9 M NaOH instead of Na_2CO_3 as precipitating agent. The sample was named CT20.

2.2. *Photo-catalytic experiment*

2.2.1. CO_2 photo-conversion

The photo-conversion of CO_2 occurred in a flat-bottom borosilicate glass photoreactor reactor. The catalyst dispersed in ethanol (Sigma Aldrich) was spread on the bottom reactor by means of Pasteur pipette while heating at 150 ^oC to obtain a homogenous film, alternating spreading and heating cycles until complete depletion of the dispersion. The reactor was then installed into a lab-made gas line [33] furnished with a separate He and CO_2 inlet valves, a gas flow controller, a saturator kept at 40 ^oC for water vaporization, a heater and a gas chromatograph (GC, HP 6890) equipped with a thermo-conductivity detector (TCD) and a Porapak Q packed-column, to analyze the outcoming gases (figure 12). A 125 W Hg UVA lamp (Helios Italquartz) with an emission line centred at 365 nm, and a 42 W halogen table lamp (Lexman) were used as UV and visible light source with an irradiance of 60 $W\cdot m^{-2}$ and 120 $W\cdot m^{-2}$ respectively. A Delta Ohm HD 2302.0 photo-radiometer and a LP 471 probe where employed for the detection of either UV (315-400 nm) or visible light (400-1000 nm) intensities.

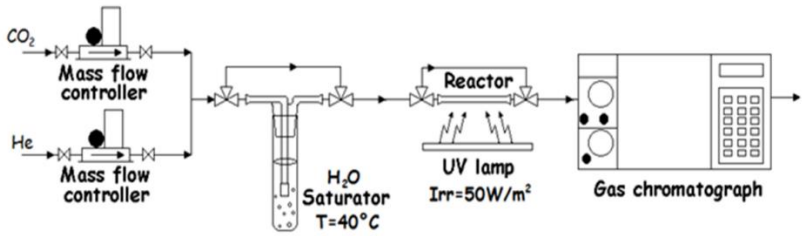

Figure 12 *Lab-made gas line employed for the photo-catalytic experiment.*

The reaction conditions were set as follow:

- Duration: 6 h
- Thin-film plate type borate glass reactor, volume 2.8 cm^3 and exposed surface 7.5cm^2
- UV-light source: 50 W/m^2, main emission peak 365 nm
- Gas flow: CO_2/H_2O mixture in a 13.33 ratio
- Temperature: 70 ^oC
- Saturator: 40 ^oC, water

Samples were UV-light irradiated for 15 minutes previous the experiment, to ensure homogeneous heating of the reaction environment. The reaction products, such as O_2, N_2, CH_4, CO_2, CO and H_2 were identified by means of calibration curves.

The turnover number (TON) was employed as tool for the comparison of CH_4 yields, as the quantity of product in moles ($mol_{\ product}$) over the mass in grams of the employed catalyst (g_{cat}), according to:

$$TON = \frac{mol_{\ product}}{g_{cat}}$$

Equation 1

2.3. Characterizations

2.3.1. Nitrogen Physisorption

Nitrogen physisorption analysis is commonly employed in the study of materials surface and pore volume, size, distribution and shape, which relies on the quantification of the physically adsorbed amount of the gas on the sample's surface.

In a typical physisorption experiment, nitrogen is let to interact with the sample at constant temperature – 196.15 ^{o}C while the pressure is varied from zero to the saturation pressure p_0 – or the normal vapour pressure of the material at that temperature – and vice versa. By plotting the volume adsorbed (or desorbed) versus the relative pressure, curves named isotherms are obtained, and their behaviour is related to the layer-to-surface adsorption [34]. Isotherms are classified by the International Union of Pure and Applied Chemistry (IUPAC) as type I-VI. Type I is typical of microporous materials. Type IV is the most common, typical of mesoporous materials Type III and V are less common and related to weak adsorbent-adsorbate interaction in non-porous or macro-porous and mesoporous, respectively. Type VI is related to the multilayer adsorption on a non-porous surface (figure 13) [35].

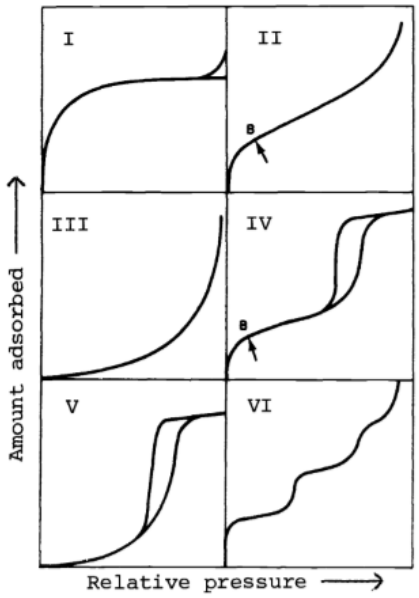

Figure 13 *IUPAC classification of physisorption isotherms [5]*

According to IUPAC, porous materials are classified for their diameter (*d*) as microporous when $d < 2\ nm$, mesoporous when $2\ nm < d < 50\ nm$ and macroporous when $d > 50\ nm$ [36].
The specific surface area A_{sp} can be calculated knowing the volume adsorbed at the monolayer V_m according to equation 1:

$$A_{sp} = \frac{V_m}{22414} N_A \sigma$$

Equation 2 *BET specific surface relation*

Where N_A is the Avogadro number ($6{,}023 \cdot 10^{23}\ mol^{-1}$), 22414 is the volume ($cm^3$) of one mole of ideal gas in standard conditions, while σ represents the occupied surface area by one N_2 molecule, generally accepted to be 0,162 nm^2 [34].
The volume adsorbed at the monolayer is commonly calculated using the Brunauer, Emmet, Teller (BET) equation as follows:

$$\frac{p}{V_{ads}(p_0 - p)} = \frac{1}{V_m} c + \frac{c-1}{V_m c} \cdot \frac{p}{p_0}$$

Equation 3 *BET equation*

Where V_{ads} is the adsorbed volume and c is the BET constant [34].

Physisoprtion data were recorded using a Micromeritics TriStar II Plus ASAP2000 analyser analyser, recording the adsorption–desorption isotherms at -196.15 °C. All samples were previously outgassed at 200 °C for 2 h and thermally treated in vacuum at 110 °C for 3 hours, in order to remove all adsorbed species. Surface area information was taken in the 0,05-0,35 p/p_0 range.

2.3.2. Temperature programmed oxidation

Temperature programmed oxidation (TPO) relies on the use of an oxygen-containing gaseous mixture as oxidizing agent to identify the number of sample-adsorbed species, such as carbon or nitrogen residues, and their oxidizing temperature [37]. The experimental setup includes a quartz-reactor, a trap and a Gow-Mac TCD for the gas detection.

For the analysis, 50 mg were placed into a U-shaped quartz reactor and heated in a 5% O2/He mixture, under a 40 mL/min flow and heating rate of 10°C/min from room temperature to 800°C. A soda-lime/magnesium perchlorate ($CaO/NaOH + MgClO_4$) trap was used to remove CO_2 and water for the gas flow. Oxygen consumption is monitored by a Gow-Mac thermal conductivity detector (TCD) and eventually plotted against temperature.

2.3.3. Temperature Programmed Reduction

Temperature programmed reduction (TPR) is widely employed for the characterization of reducible solid and allows to monitor the temperature-dependent course of reduction reaction [38]. Moreover, it is informative of the reduction state of metallic species and of the contribute of metal-oxide interaction, in metal-loaded semiconductors.

For the analysis, 50 mg of samples were heated in a 5% H_2/Ar gas mixture, with a 40 mL/min and heating rate of 10°C/min from room temperature to 800°C. A magnesium perchlorate trap was used to remove water from the gas flow. Hydrogen consumption was monitored by a Gow-Mac thermal conductivity detector (TCD) and plotted against temperature.

2.3.4. Temperature Programmed Desorption

Temperature Programmed desorption (TPD) is employed for the study of adsorbed chemical species on the sample surface, which may desorb by increasing temperature. The technique is used for the determination of kinetic and thermodynamic parameter of desorption and decomposition processes [39].

2.3.4.1. He-TPD

For the experiment, 50 mg of samples were pre-heated at 110 °C for 1 h using a magnesium perchlorate trap to remove water from the sample surface, before being exposed to a He flux of 40 mL/min and heating rate of 10°C/min from room temperature to 800°C, without trap. Gas released were monitored by a Gow-Mac thermal conductivity detector (TCD) and plotted against temperature.

2.3.4.2. CO_2-TPD

Similarly, 50 mg of sample were pre-heated at 110 °C for 1 h using a magnesium perchlorate trap to remove water from the gas flow, before being exposed to CO_2 pulses up to saturation at room temperature, without any trap. A He-TPD followed as aforementioned. Gas released were monitored by a Gow-Mac thermal conductivity detector (TCD) and plotted against temperature.

2.3.5. Photoluminesce measurement

The spontaneous emission of light from a material upon light excitation is known as photoluminescence (PL). PL experiments mainly rely on the interpretation of the detected emission spectrum as indication of the transition energies of bandgap and intra-gap states related to radiative recombination processes. A typical PL instrument is composed by light sources of different nature, a sample holder, a spectrometer and a detector (figure 14). In general, the penetration depth may vary, thereby allowing either surface or bulk states investigation depending on the excitation wavelength and on the type of material (i. e. direct or indirect bandgap semiconductors).

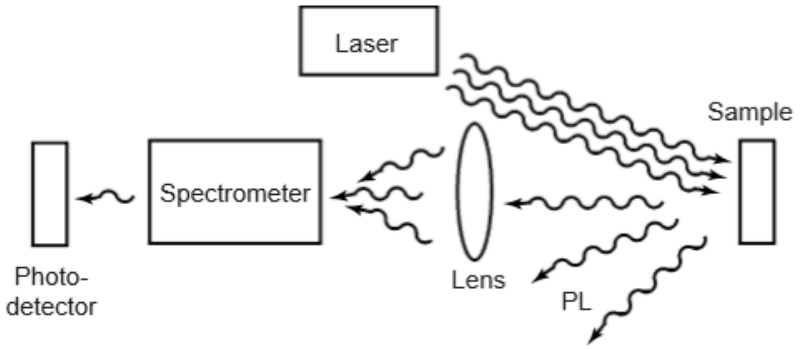

Figure 14 *Typical instrumental set for detection of the photoluminescence*

Moreover, the modulation of the incident light intensity is also employed to study the presence of defects and impurities, as well as the study of interfaces, by influencing the densities of photoexcited electrons and holes [40]. The modulation of the investigating source is also advantageous for time-resolved PL by which the time of decay of radiative emission, as well as the quantum efficiency, can be evaluated.

In time-resolved PL, the electron states of the samples are excited by a laser (or a LED) source, and the emitted photons are detected and plotted against time, to obtain decay curves. The analysis of the decay pattern relies on the comparison of life-time constants B_n and parameters τ_n obtained by the following fitting procedure (equation 4)

$$Fit = A + B_1 e^{-t/\tau_1} + B_2 e^{-t/\tau_2} + B_3 e^{-t/\tau_3}$$

Equation 4 *Tri-exponential fit employed for the visible-emission life-time measurement*

The analysis of the time constants τ_n is employed for the comparison of time decays.

PL analysis was carried out with a spectrofluorometer (Edinburg Instrument FLS-980) by measuring the emission spectra in the range 350-750 nm, using 300 nm as the excitation wavelength. A LED (371.8 nm) was used as the excitation source for life-time measurements by time-resolved PL experiment.

2.3.6. Diffused Reflectance Spectroscopy

Diffuse Reflectance Spectroscopy (DRS) involves the measure light scattered by the sample, which by turn may be related to the absorption and employed for the measurement of the semiconductor's bandgap. The measured reflectance is widely related to the absorption by mean of the Kubelka/Munk function:

$$F(R_\infty) = \frac{(1 - R_\infty)^2}{2R_\infty}$$

Equation 5 *Kubelka-Munk function*

Where R_∞ is the reflectance of a layer *t* whose an increase in thickness do not further affect the reflectance ($t \to \infty$) [41].

The diffused reflectance (R%) spectra of powder samples were measured with a Cary UV-Vis spectrophotometer (Agilent Technology) at room temperature and pressure.

2.3.7. X-ray Diffraction

X-ray diffraction is used to study the crystal structure and atomic spacing of crystalline samples by means of a monochromatic x-ray source.

The incident rays of wavelength λ, interacting with the sample a constructive interference and therefore diffraction according to the Bragg's law (equation 6):

$$2\lambda = 2d_{hkl}sin(\theta)$$

Equation 6 *Bragg's law*

where θ is the diffraction angle and d is the distance between crystal planes. Detection of diffracted radiation results in a typical diffraction pattern, which is unique for each material crystal phase and identified as a series of peaks when plotted against 2θ [42]. Each peak is related to a defined crystal plane d_{hkl} – having the same Miller indices h, k, l – which also allows the evaluation of the lattice constant (*a*, *b* and *c*) and volume. Eventually, the full width at half maximum (β) of the peaks is related to the crystallite size D by Scherrer equation:

$$D = \frac{K\lambda}{\beta cos(\theta)}$$

Equation 7 *Scherrer equation*

Where K is a phase constant and θ is the diffraction angle [43].

X-ray Diffraction (XRD) patterns were collected on a Bruker D8 Advance powder diffractometer with a sealed X-ray tube (copper anode; operating conditions, 40 kV and 40 mA) and a Si(Li) solid state detector (Sol-X) set to discriminate the Cu Kα radiation. Apertures of divergence, receiving, and detector slits were 2.0 mm, 2.0 mm, and 0.2 mm, respectively. Data scans were performed in the 2θ range 5–75◦ with 0.02◦ step size and counting times of 3 s/step. Quantitative phase

analysis and crystallite size determination were performed using the Rietveld method as implemented in the TOPAS v.4 program (Bruker AXS) using the fundamental parameters approach for line-profile fitting. The determination of the crystallite size was accomplished by the Double-Voigt approach and calculated as volume-weighted mean column heights based on integral breadths of peaks.

2.3.8. X-ray Photoelectron Spectroscopy

X-ray Photoelectron Spectroscopy (XPS) is a technique for the determination of the binding and kinetic energy of ejected photoelectrons upon X-ray irradiation, in vacuum. The constant energy of the irradiating source *hv* is related to the kinetic energy of the emitted photoelectron E_K, the electron binding energy E_B with respect to the Fermi level, and to work function φ by the following equation:

$$hv = E_k + E_B + \varphi$$

Equation 8

Being the investigation depth dependent on the kinetic energy of the photoemitted electrons and considering that in general $hv < 1.5\ keV$, the obtained information is mainly related to the study of surfaces and outermost layers (5-10 nm thickness from the surface), as well as of the presence of surface-adsorbed contaminants, which may therefore present high variability within samples. XPS is able to give the composition of the analysed region (in terms of atomic fractions): after the identification of the chemical elements by the EB value of the photoelectronic bands, the evaluation of the band area allows to determine the amount of the different elements, with a detection limit usually around 1%. Moreover, E_B values may be informative about the chemical state of the related element. In case of surface charging, the right value of E_B is generally determined with respect to the E_B of a known chemical group present in the analysed region (or to the C1s signal of carbon surface contamination).

The E_B (eV) peaks area is employed for element quantification, while in spectra composed by multiple peaks, detailed information about the chemical bonding state may be obtained [44].

X-ray photoelectron spectroscopy (XPS) surface analysis of samples I, D, anc C was performed using a Perkin-Elmer Φ 5600ci spectrometer, using non-monochromatic Al Kα radiation (1486.6 eV) in the 10^{-6} Pa pressure range. The analyzed sample area was around 0.5 mm2. In addition to the wide range survey spectrum, single spectra were recorded for Ti 2p, Cu 2p, O 1s, and C

1s regions. All the binding energy (BE) values are referred to the Fermi level. The correct calibration of the BE scale was verified by checking the position of both $Au4f_{7/2}$ and $Cu2p_{3/2}$ bands (from pure metal targets), falling at 84.0 eV and 932.6 eV, respectively. The raw spectra, after a Shirley-type background subtraction, were fitted using a non-linear least-square fitting program adopting Gaussian–Lorentzian peak shapes for all the peaks (XPSPEAK41 software). Because of surface charging, samples presented a shift of the bands toward higher BEs (of around 2 eV): the charging effect was corrected by using an internal reference (Zn $2p_{3/2}$ band centered at 1021.4 eV in ZnO compound). The uncertainty of the determined BE values was not larger than 0.2 eV. The atomic composition of the sample analyzed region (about 10 nm of thickness from the surface) was evaluated using sensitivity factors as provided by θ V5.4A software, after a non-linear least-square fitting process to calculate the area of the different XPS bands. The uncertainty of the atomic composition of the different elements is lower than 10%.

2.3.9. Scanning Electron Microscopy

Scanning Electron Microscopy is widely employed for the analysis of sub-micro-scaled materials and their topography, morphology, chemical composition and crystallography. Electron ejected by an electron gun form an electron beam and are then focused on the sample by magnetic lenses and collected when scattered by an electron detector. While secondary electrons are mainly used for imaging purpose mainly constituting the surface signal, back scattered electrons are related to a bulk signal and may be informative of the elemental composition [45].

The morphology and composition were examined by Field Emission Gun Electron Scanning Microscopy (FE-SEM) LEO 1525 ZEISS, after metallization with chromium. Elemental composition and chemical mapping were determined using a Bruker Quantax EDSFT.

2.3.10. Atomic Absorption Spectroscopy

Atomic Absorption Spectroscopy (AAS) was employed to quantify the metal contents in metal-loaded samples. AAS relies on the detection of the absorption spectrum upon vaporization of the sample, by mean of a flame or a plasma source, followed by light-mediated excitation of electrons from the ground state [46].

Samples were solubilized and desegregated by using milli-Q water and *aqua regia* (3:1 volumetric mixture of HCl and HNO_3), while heating in a reflux condenser-equipped system for 3 h. Solutions were further diluted in milli-Q water and *aqua regia* in milli-Q water (1:19) was used as blank.

Analyses were performed with a Perkin-Elmer Analyst 100 flame atomic absorption spectrometer where flame has been fed by 1:3 acetylene-air mixture and a copper hollow-cathode lamp, by using a λ of 324,8 nm.

Table 1 *Resume of the composition, synthetic procedure, heat treatment and duration of all synthesised samples.*

Sample	Material	Synthetic Method	Heat treatment (ºC)	Duration (h)
4CSZ	ZnO	Wet precipitation	400	4
6CSZ	ZnO	Wet precipitation	600	4
4PNZ	ZnO	Template-mediated hydrothermal synthesis	400	4
Ag4CSZ	Ag/ZnO	Dry impregnation	110	18
Cu4CSZ	Cu/ZnO	Dry impregnation	110	18
AgCu4CSZ	AgCu/ZnO	Dry impregnation	110	18
CCZ20	CeO_2-ZnO	Wet co-precipitation	400	4
CT20	CeO_2-TiO_2	Wet co-precipitation	400	4
SP10	P25/SiO_2	Dry impregnation	110	18
SBP10	P25/SBA-15	Dry impregnation	110	18
T4CSZ	TiO_2/	Dry impregnation	100	18

3. Results and Discussion

3.1 XRD analysis

Figure 15 shows the XRD analysis results of 4CSZ and 6CSZ with the characteristic pattern of zincite and crystal size of 18.02 nm and 42.7 nm, respectively. The analysis reported the lattice constant *a* as 3.2512 Å for 6CSZ and as 3.2509 for 4CSZ, while the constant *c* was 5.209 Å and 5.210 Å respectively, accounting for a *c/a* ratio of 1.6023 and 1.6026 which is commonly attributed to the wurtzite crystal structure with a hexagonal unit cell [47]. As expected, the sample treated at higher temperature (6CSZ) resulted in increased crystallinity when compared to 4CSZ and 4PNZ assumed from the higher signal intensity (figure 15). The broader peaks of 4CSZ with respect to the ones of 6CSZ were related to the smaller crystal dimension. The pattern of 4PNZ, obtained via hydrothermal synthetic method, was also identified as zincite showing lower intensity and a bump at low angle ($2\theta < 20^{o}$), the latter indicating an amorphous component (figure 15) likely due to an inappropriate size-related heat treatment temperature and/or length. Moreover, the absence of a preferential growth oriented towards the *c*-axis in the *002* crystal plane, typical of rod-like structures, was attributed to the microscale dimension of the 4PNZ aggregates, not supporting a mono-dimensional growth (figure 15).

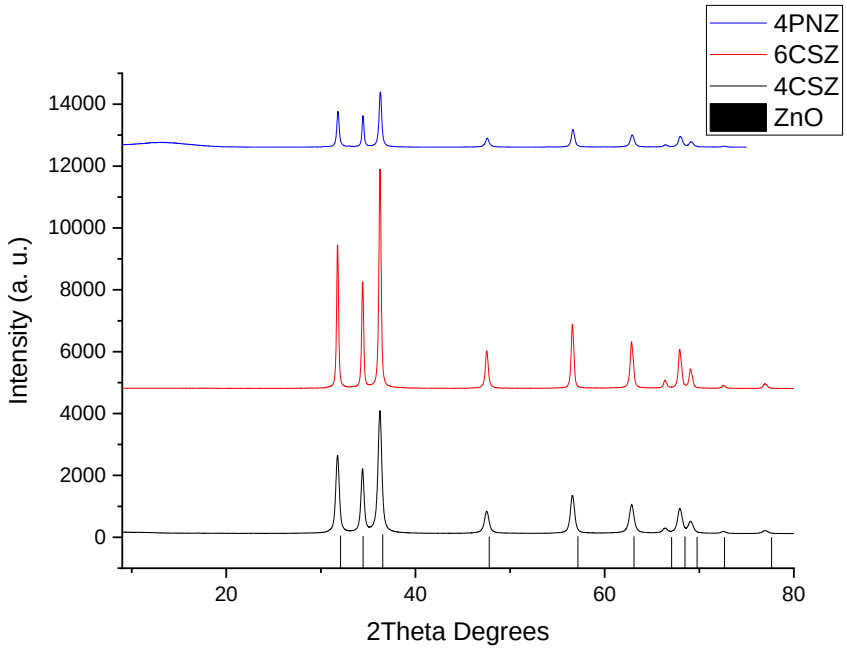

Figure 15 *Comparison of XRD pattern of ZnO-based materials obtained by different synthetic method.*

Figure 16a shows the XRD pattern obtained for CCZ20, confirming both the presence of zincite in the wurtzite phase and of cerianite as cubic fluorite. In general, as no peak shift was detected, the

presence of smaller CeO_2 crystallites dispersed in the ZnO structure was hypothesized. The latter showed an XRD pattern similar to the pure ZnO-based materials (figure 15).

No crystal patterns were detected after XRD analysis of CT20 (figure 12b). The introduction of cerium via co-precipitation had already been reported to affect the crystal phase of TiO_2 [48]. Additionally, an amorphous pattern similar to figure 16b was already reported and attributed to cerium titanate $Ce_xTi_{(1-x)}O_2$ in the TiO_2 phase [48], as result of the hetero-structure.

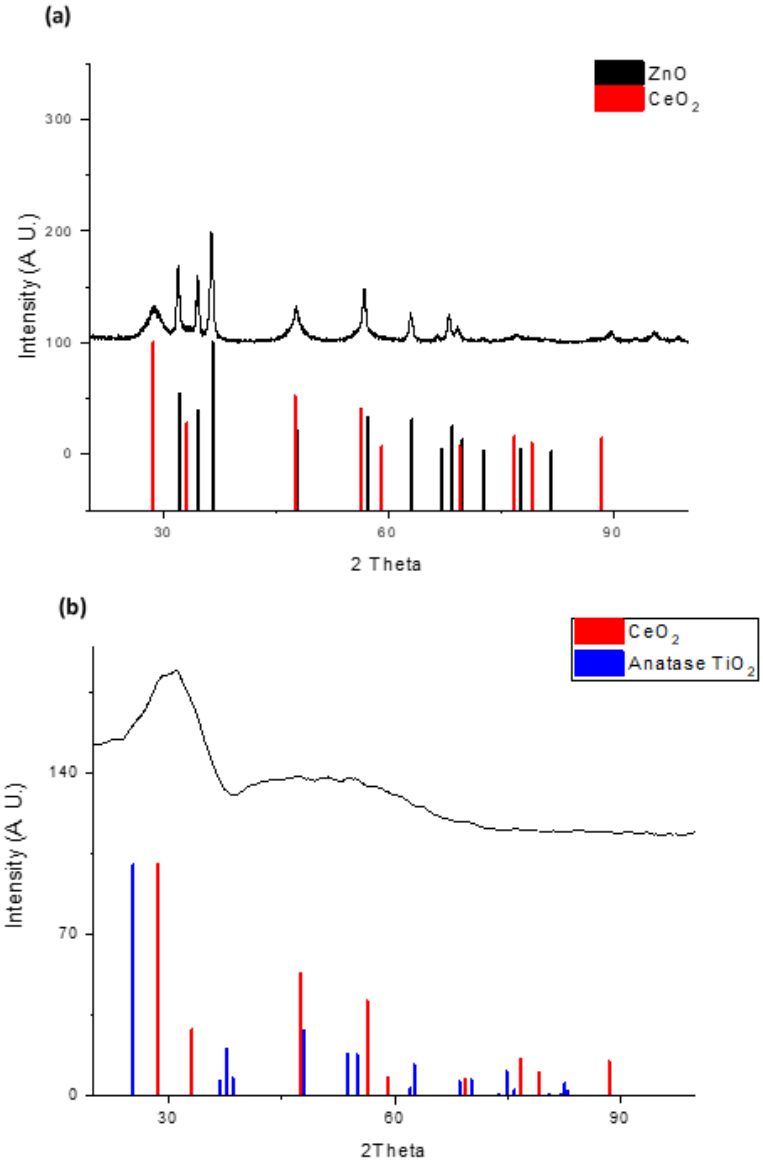

Figure 16 *XRD pattern of (a) CCZ20 and (b) CT20.*

3.2 XPS analysis

The binding energies (BE) of C 1s, O 1s and Zn $2p_{3/2}$ of the different ZnO-based samples 4PNZ, 6CSZ, T4CSZ and 4CSZ were obtained by XPS analysis and compared to commercial ZnO.

The XPS signal of Zn $2p_{3/2}$ are reported in figure 17 and the presence of ZnO was confirmed by the Auger parameter at 2010 eV [49].

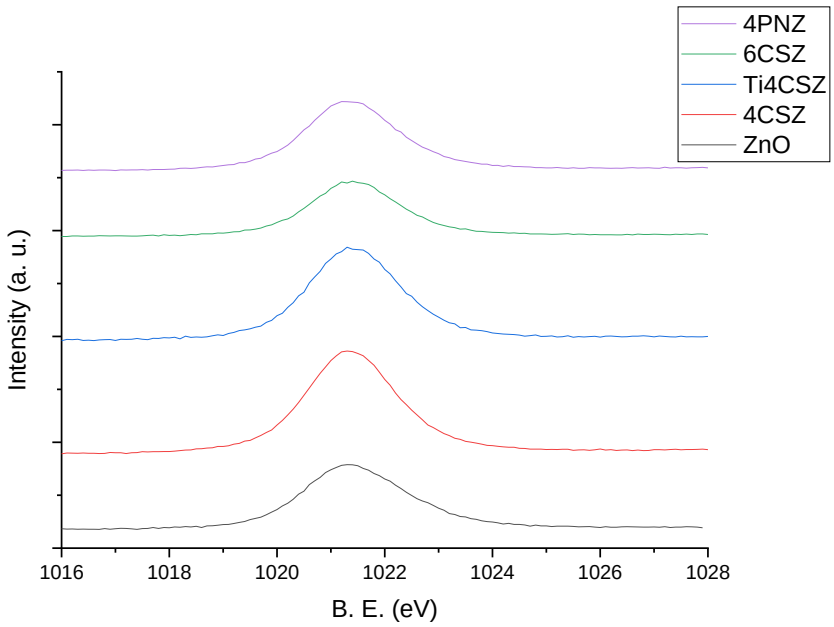

Figure 17 *Zn $2p_{3/2}$ XPS signals of ZnO-based samples*

The analysis showed the presence of carbon in all samples (table 2), identified as C 1s in either C – C, C – O – C or C = O type for the binding detected at 284.7 eV, 286.0 eV and 288.5 eV respectively (figure 18). The signals were mainly related to surface-adsorbed carbon dioxide from atmosphere or other adventitious carbon which was more attenuated for all synthesized samples with respected to commercial ZnO except from 4PNZ (table 2).

The highst amount of adsorbed C (12.4 %C) was found on 4PNZ sample (table 2) and potentially related to residual traces due to the employment of an organic templating agent (PVP) in the synthetic procedure, which was not possible to eliminate during the air annealing procedure.

Table 2 *Oxygen to zinc ratio used as indication of O vacancies defects in ZnO-based materials.*

Sample	C%	O%	Zn%	Ti%	O/Zn
4CSZ	7.5	40.8	51.7		0.79
6CSZ	5.3	50.2	44.5		1.12
T4CSZ	4.6	40.7	53.5	1.2	0.76
4PNZ	12.4	42.0	45.6		0.92
ZnO	9.5	45.2	45.3		0.99

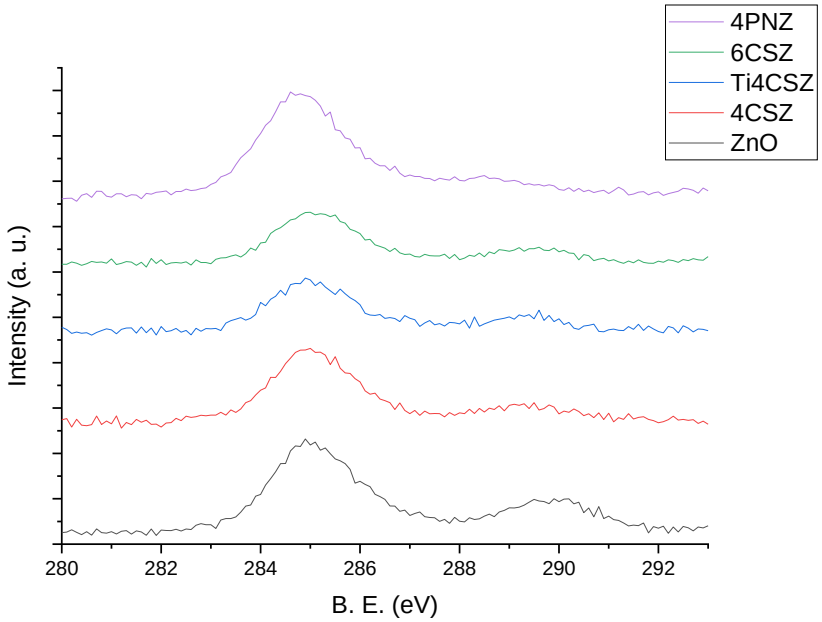

Figure 18 *C 1s XPS signals of ZnO-based samples.*

Figure 19 shows the two peaks of O 1s BE related to reticular oxygen and oxygen vacancies or hydroxyl groups are indicated as (a) and (b) in table 3, respectively. The percentage area of both the oxygen chemical species was determined after fit using a non-linear least-square fitting program adopting Gaussian–Lorentzian peak shapes: the reticular oxygen component was found to be lower in 4PNZ (around 65%), supporting the presence of amorphous regions also detected by XRD analysis (see section 3.1). The variation in oxygen content was evaluated as O/Zn ratio and reported in table 2. The different annealing temperature of 6CSZ and 4CSZ was possibly the main responsible of the difference in oxygen content (table2), evaluated as 1.12 and 0.79 respectively if compared to the zinc content, proposed as the result of increased vacancies filling proportional to the increase in the annealing temperature [50]. An O/Zn ratio of 4PNZ near to stoichiometry was achieved by hydrothermal method, suggesting the potential role of the synthetic method in the modulation of crystal defects.

Table 3 *BE indicated in eV of (a) reticular and (b) defects-related O 1s*

Sample	O 1s (a)	O 1s (b)	% area (a)
4CSZ	530.1	531.7	71
6CSZ	520.2	531.7	67
T4CSZ	530.1	531.7	73
4PNZ	530.1	531.6	65
ZnO	530	531.8	49

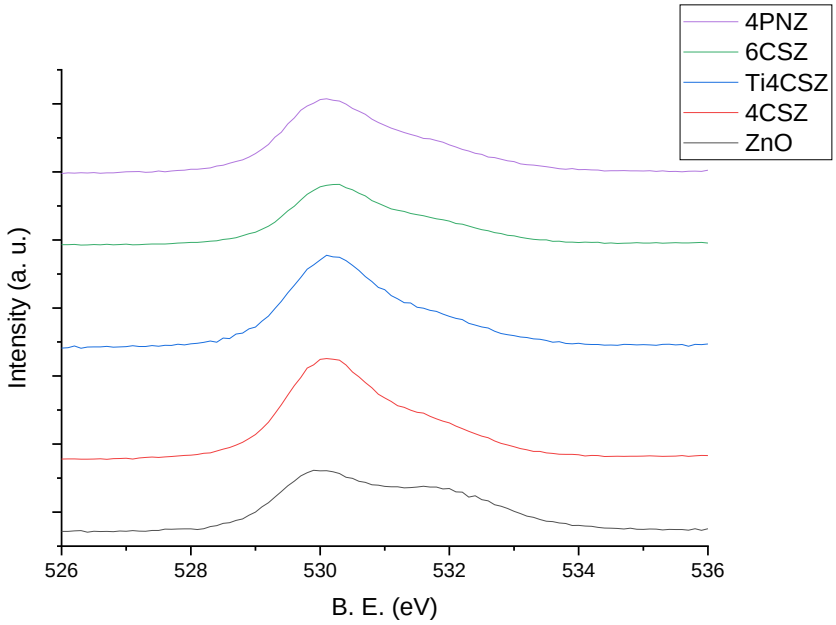

Figure 19 *O 1s XPS signals of ZnO-based samples*

The presence of tetravalent Ti^{4+} in T4CSZ was confirmed by the peak at 458.4 eV of Ti $2p_{3/2}$ in atomic percentage around 1 % (figure 20). A very weak peak at 399.0 eV of N 1s was detected in all samples, corresponding to a very small amount (< 1%) of this element, probably deriving from atmospheric contamination.

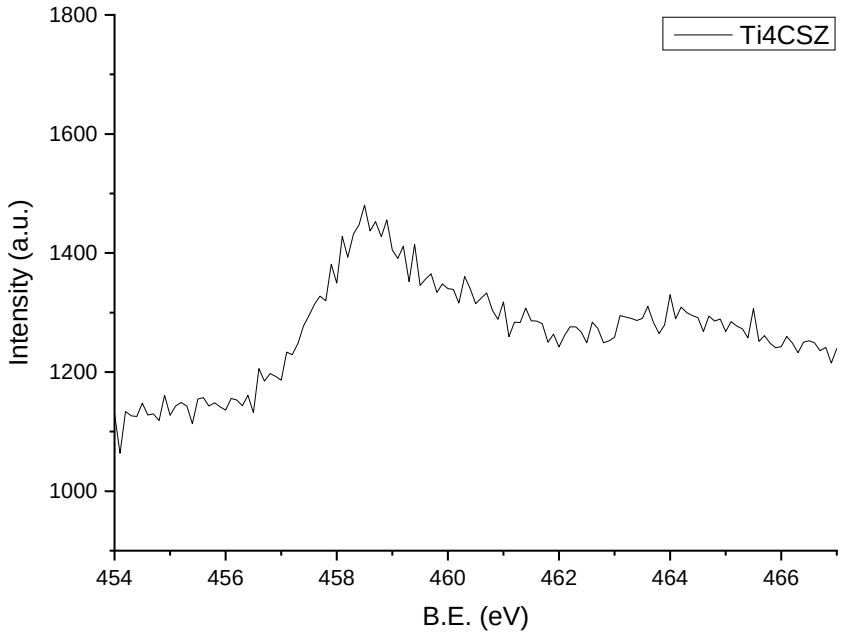

Figure 20 *Ti 2p XPS signal of 4TCSZ*

3.3 SEM-EDX

The scanning electron microscopy (SEM) analysis of 4CSZ is reported in figure 21, shows irregularly shaped aggregates of the order of 2-10 µm composed of smaller nano-sized particles.

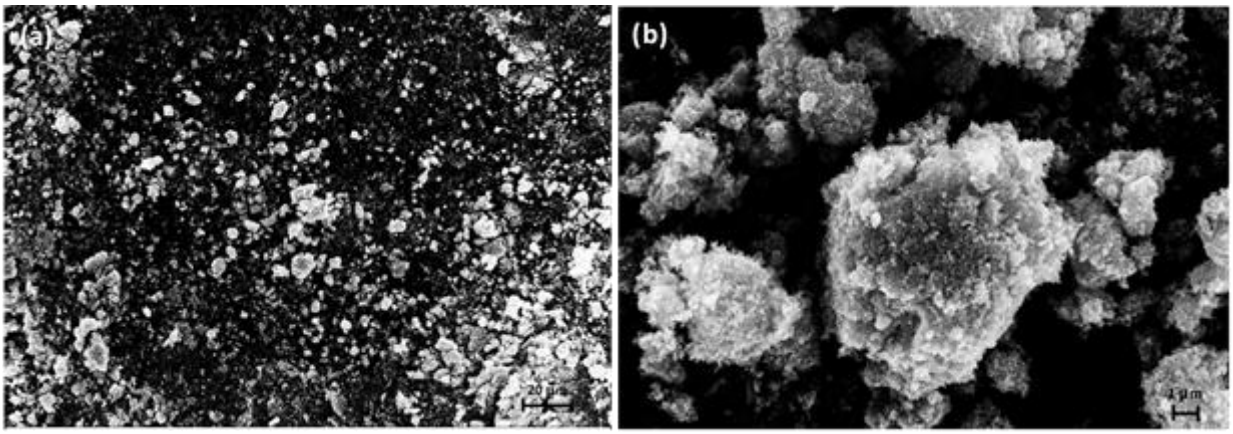

Figure 21 *SEM of 4CSZ showing (a) bigger and (b) smaller aggregates, visible with different magnification.*

The scanning electron microscopy (SEM) analysis of 6CSZ revealed nano-sphere and nano-cylinders ranging from 20 to 50 nm width and length (figure 22a, b), more regularly shaped and homogeneously dispersed than 4CSZ (figure 21). The shape and dimensions were attributed to the

different annealing temperature. The lower annealing temperature (400 ^{o}C) accounted for lower crystallites dimension, which allowed more versatility in shape and size of the particles, while a higher heat treatment temperature (600 ^{o}C) was able to stabilize the formation of bigger crystallites and consequently more stringent condition in the shape and size-related growth, as well as an increased crystallinity (section 3.1).

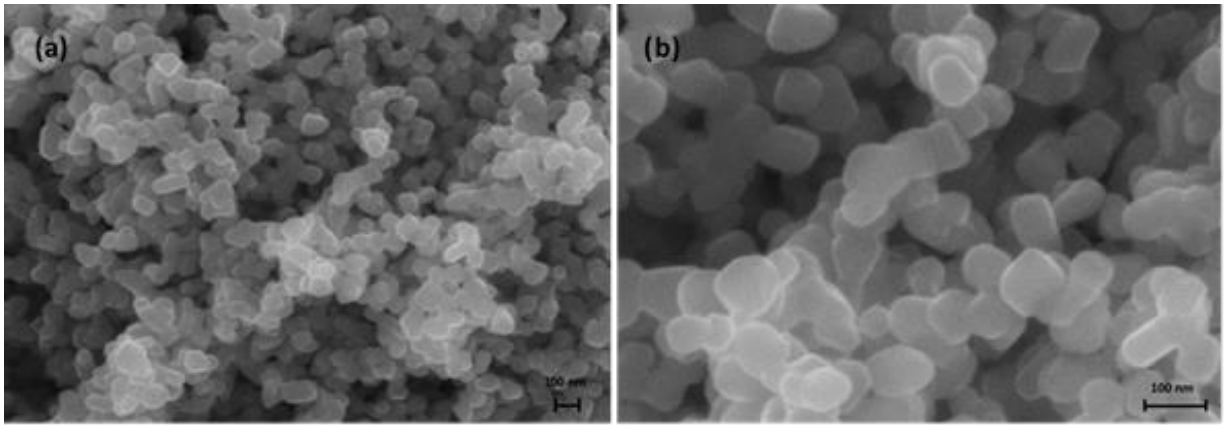

Figure 22 *SEM at different magnifications of nano-spheres and nano-cylinders constituting 6CSZ*

To evaluate the effect of shape on the photocatalytic activity and on the photo-stability of ZnO-based materials, the synthesis of 1D nanorod was attempted by using a hydrothermal method, as elsewhere reported [51]. The SEM analysis of 4PNZ showed an elongated but ellipsoidal shape, with a length ranging from 200 nm to 1 μm (figure 23a, b). Although the effect of pH, pressure and temperature conditions of the aging procedure, as well as the annealing temperature, are well known growth-affecting parameters, the amount of PVP employed was also reported to play a fundamental role in the determination of both the particles shape, length and diameter [52]. Moreover, the mechanism of the PVP-mediated stabilization of Zn^{2+} ions acting as nucleating centres, for further ZnO precipitation and growth, was proposed to occur via coordination by means of N and O electronic doublet [52]. Therefore, the obtained shape (figure 23a, b) was mainly attributed to the concentration of PVP, which resulted too low to grant the stabilization of a completely mono-dimensional and mono-disperse growth. Moreover, it is possible that both the use of $Zn(NO_3)_2$ as precursor, rather than zinc acetate, as well as the big molecular weight of the polymer, interfered in the PVP-mediated ion coordination process, thereby resulting in the stabilization of nucleation centres bigger than expected. Nevertheless, the elongated form validated the ability of PVP to direct the growth, suggesting the role of the shaping agent concentration as effective tool for the size and shape modulation.

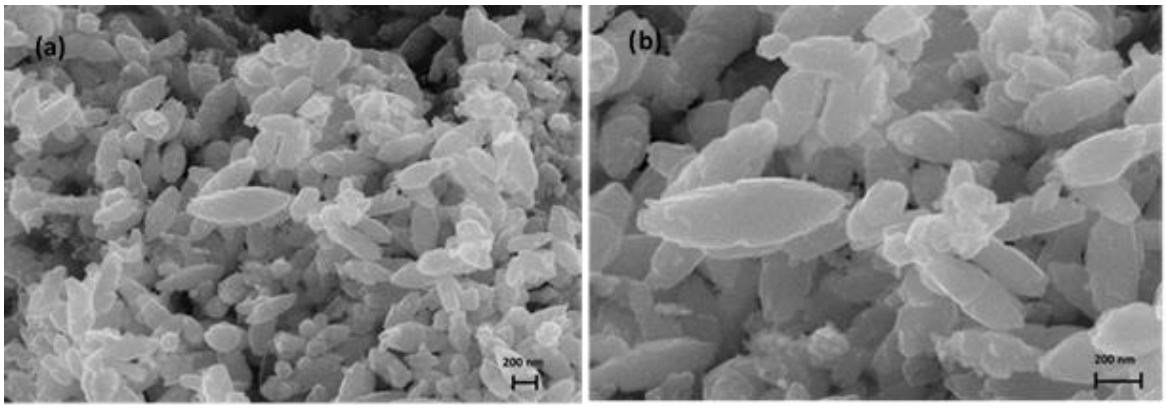

Figure 23 *Ellipsoidal micro- and sub-micro-particles of the sample 4PNZ obtained via hydrothermal method.*

The results of P25 dry impregnation on commercial SiO_2 (SP10) and SBA-15 (SBP10) are shown in figure 24 a-b and c-d, respectively. SP10 consists in big and irregular SiO_2 chunks with on-top broadly distributed P25-containg aggregates (figure 24a, b). Similarly, SBP10 is displayed as aggregates of P25 nanoparticles on top of the micrometre-sized SBA-15 scaffold (figure 24 c, d). Apart from scaffold dimensions, the aggregates size and distribution were inversely related in SP10 and SBP10.

SEM-EDX analysis confirmed the atomic distribution of titanium on top of commercial SiO_2 and SBA-15, as the yellow spots in figure 25 and 26 respectively. The analysis also revealed Ti amount of about 10% in weight for SBP10 (figure 27a) – a bit higher than expected – and of nearly 6% for SP10, which also presented small traces of aluminium and potassium (figure 27b).

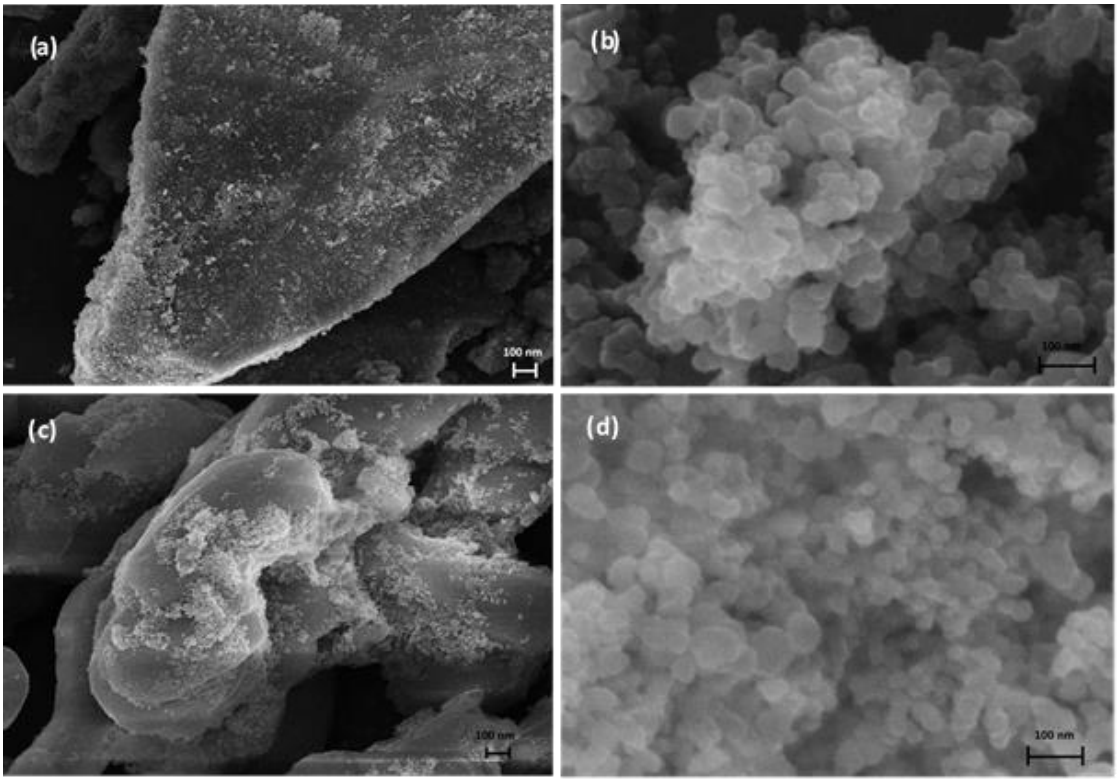

Figure 24 *SEM images of (a) SP10 and (c) SBP10, showing the different dimensions of the P25-based aggregates, in (b) and (d) respectively.*

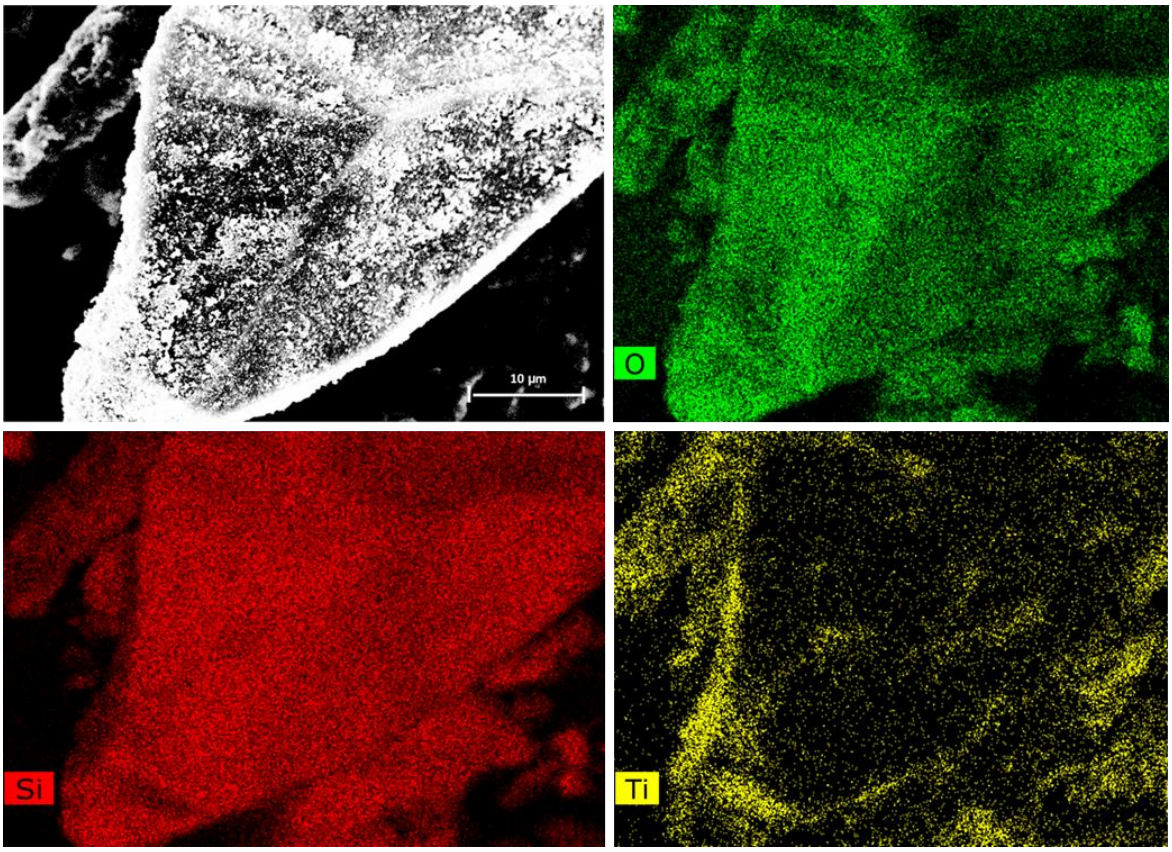

Figure 25 *SEM-EDX analysis of SP10 showing (green) oxygen, (yellow) titanium and (red) Silicon atomic distribution.*

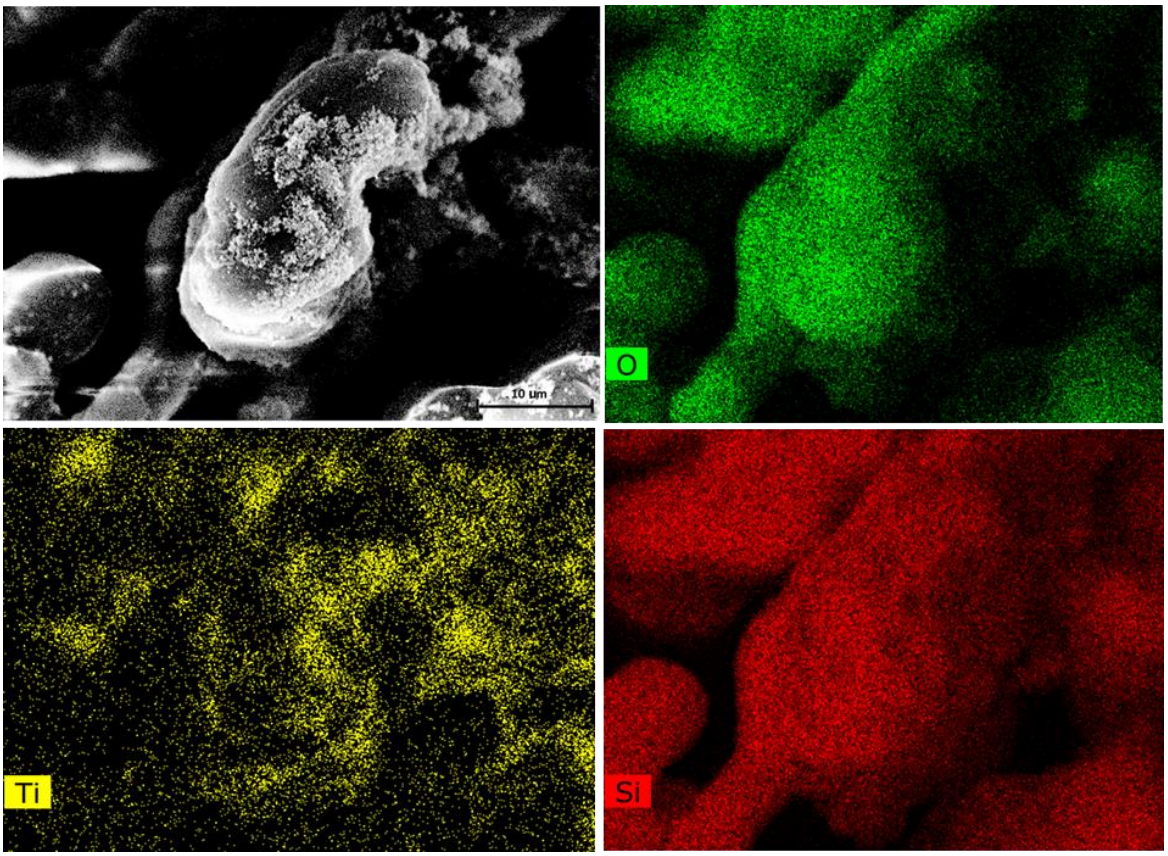

Figure 26 *SEM-EDX analysis of SBP10 showing (green) oxygen, (yellow) titanium and (red) Silicon atomic distribution.*

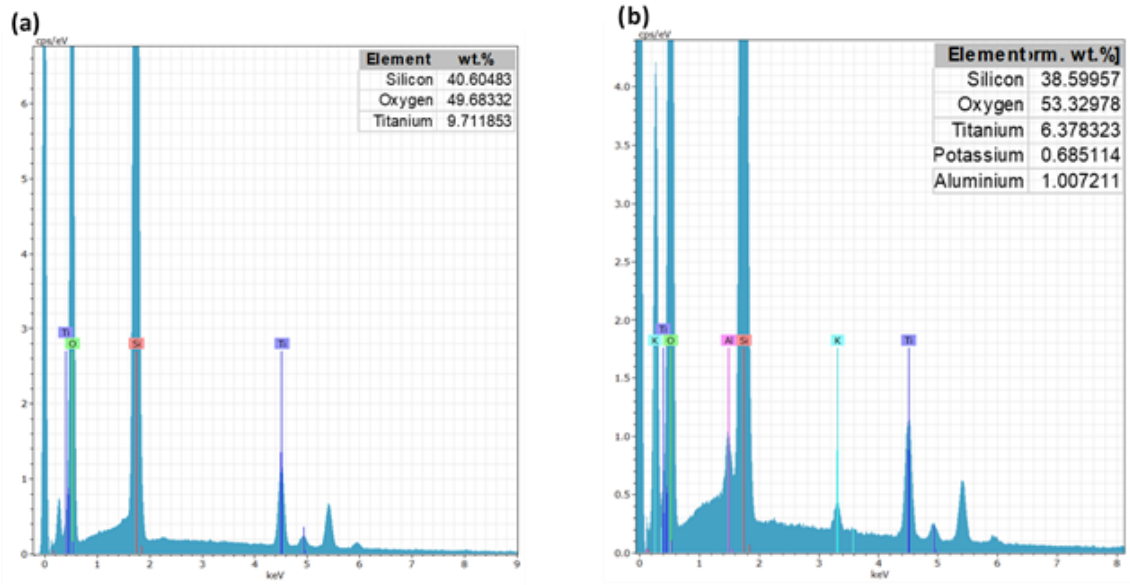

Figure 27 *SEM-EDX spectra of (a) SBP10 and (b) SP10.*

The SEM analysis of cerium-containing composites obtained via co-precipitation method are reported in figure 28 and 29. CCZ20 resulted in spheroidal and cylindrical nano-sized particles, with average diameter of 28 nm and length of 17 nm (figure 28a, b). CT20 composite was also detected as composed by spheroidal particles with average diameter of 12 nm (figure 29a, b). The morphological properties were mainly ascribed to the employed synthetic technique and to the different Zn or Ti interactions with Ce^{4+} ions, which therefore led to two different reticular structures. In fact, the sample precipitated by means of NaOH (CT20) resulted in nanoparticles of smaller size thus preventing the formation of single TiO_2 and CeO_2 crystallites, thereby supporting the formation of an amorphous hetero-structure, as also suggested by XRD analysis (see section 3.1). Conversely, the bigger nanoparticle obtained by using Na_2CO_3 as precipitating agent led to bigger nanoparticles for CCZ20, which accounted for the stabilization of detectable ZnO and CeO_2 single crystallites. Eventually, the different size and orbital structure of Ti^{4+} and Zn^{2+} ions were also hypothesized to play a relevant role in the transition metal-to-lanthanide interaction.

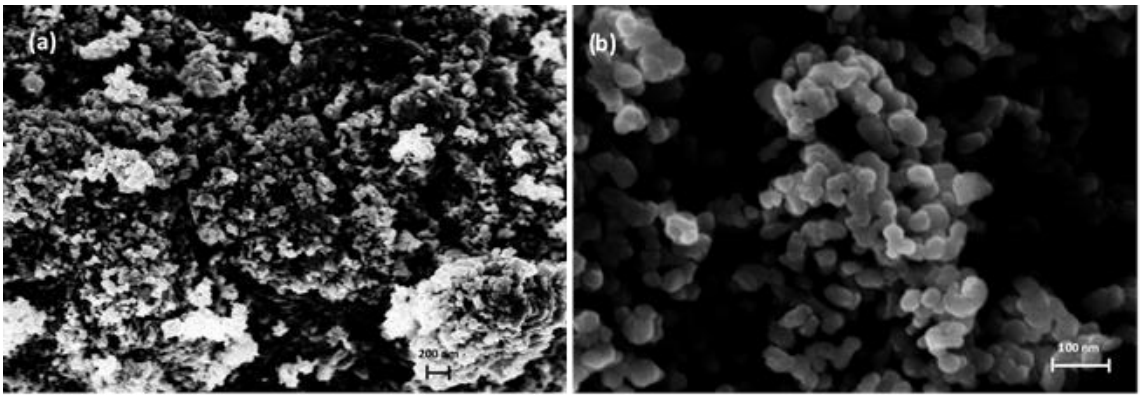

Figure 28 *SEM analysis of CCZ20 showing (a) bigger and (b) smaller clusters of spheroidal nanoparticles with 28.53 nm average diameter.*

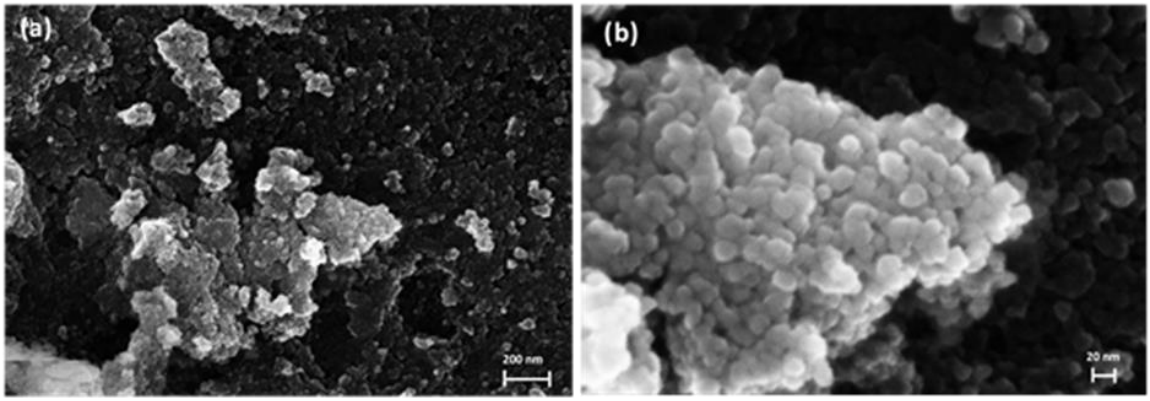

Figure 29 *SEM analysis of CT20 showing (a) bigger and (b) smaller clusters of spheroidal nanoparticles with nearly 12 nm average diameter.*

SEM-EDX showed the atomic distribution of Ce, O and Ti or Zn in CT20 and CCZ20 displayed in figure 30 and 31 respectively. Notably, the atomic percentage resulted to be about 7% for CCZ20 (figure 32a) and 4% for CT20 (figure 32b), which were nearly as expected as indicated by a Ce/Zn and Ce/Ti ratio of ∼0.2 (figure 31a-b).

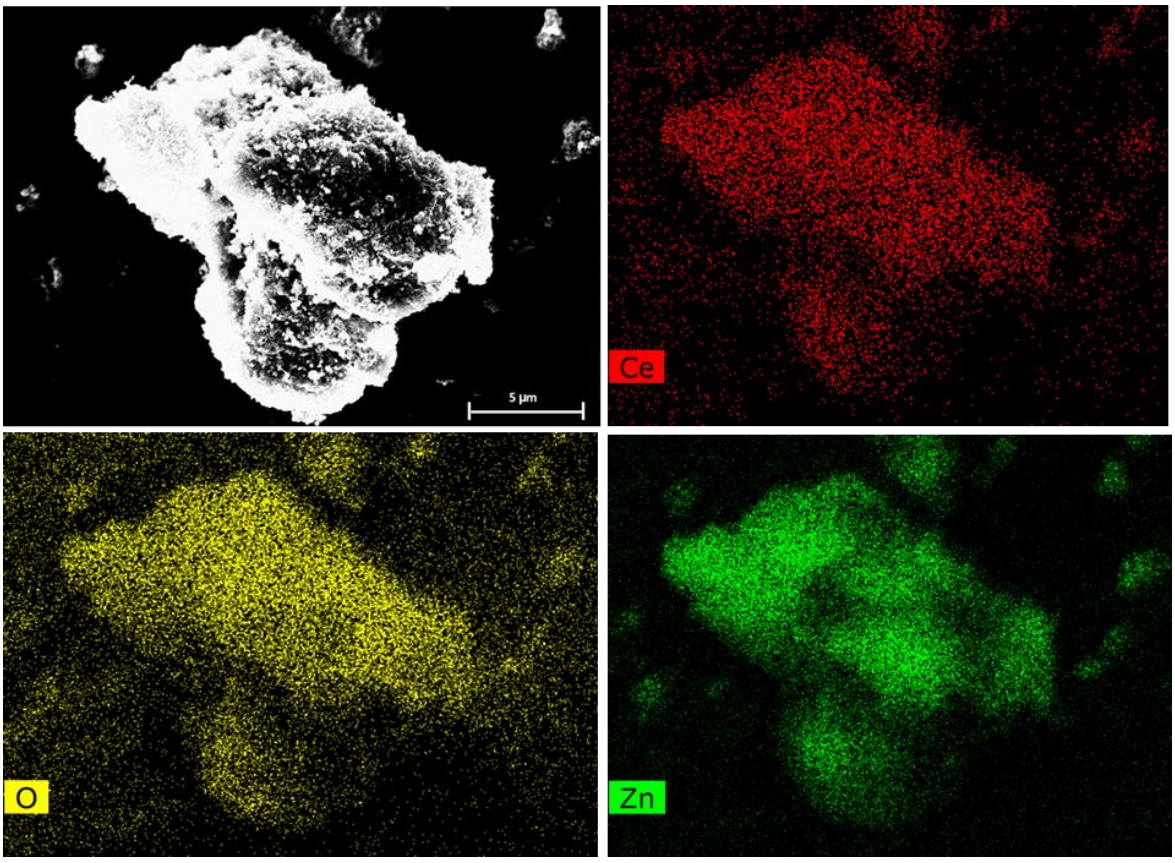

Figure 30 *SEM-EDX analysis of CCZ20 showing the atomic distribution of (red) cerium, (yellow) oxygen and (green) zinc.*

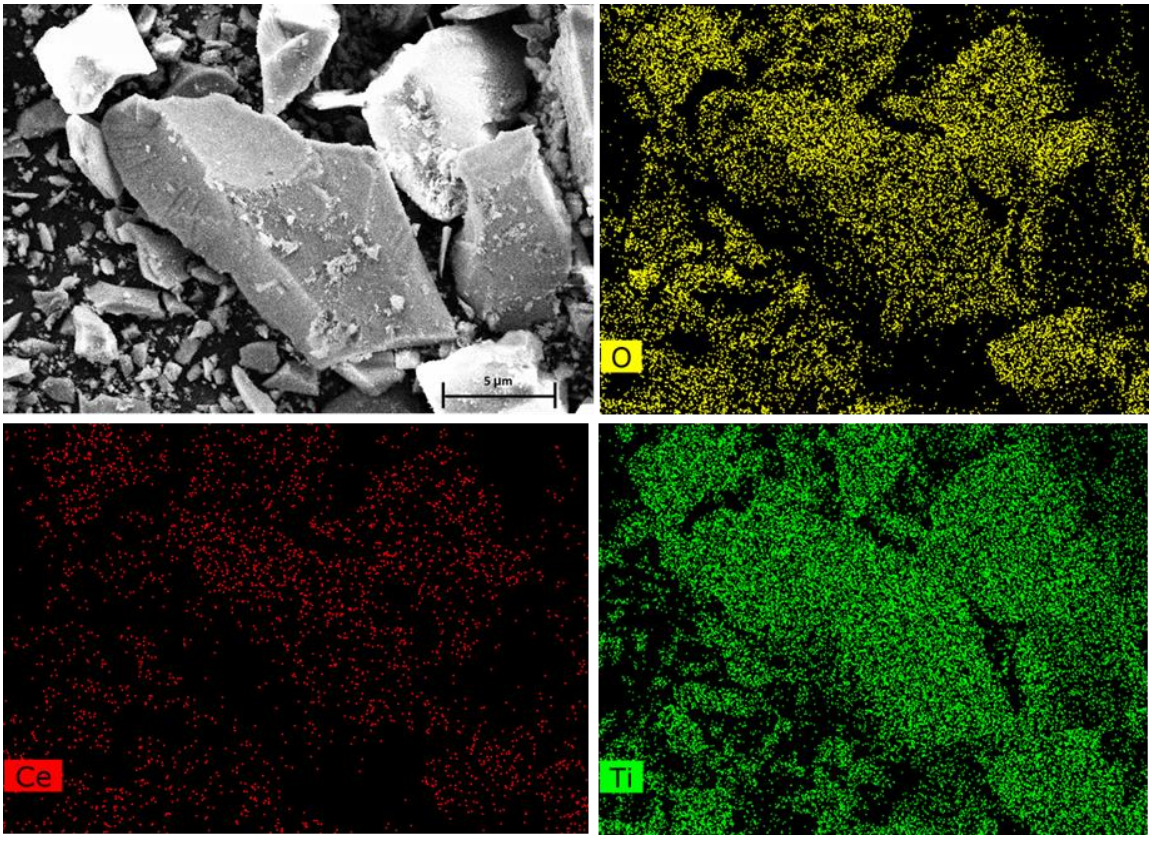

Figure 31 *SEM-EDX analysis of CT20 showing the atomic distribution of (red) cerium, (yellow) oxygen and (green) titanium.*

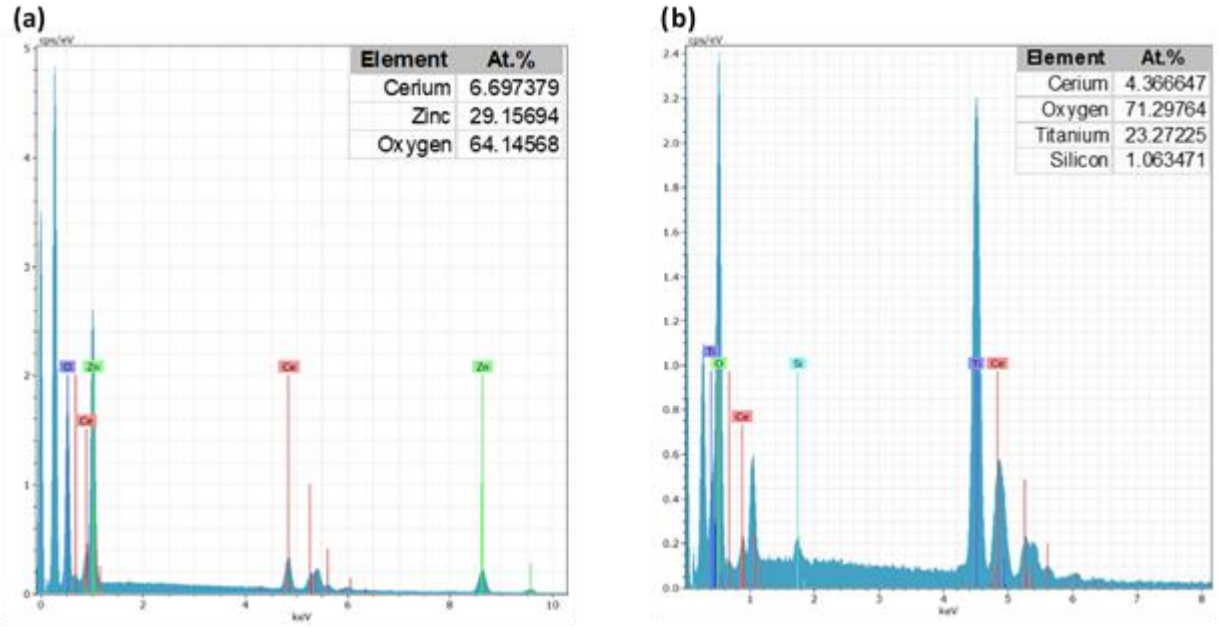

Figure 32 *SEM-EDX spectra of (a) CCZ20 and (b) CT20.*

3.4 Nitrogen Physisorption

BET analysis after N_2 physisorption experiment showed a surface area of 12.3 m^2/g and of 35 m^2/g for 6CSZ and 4CSZ respectively, which were slightly higher than the one measured for commercial ZnO 4.9 m^2/g. The resulting isotherms suggested a macro-porous (figure 33a, b). The presence of Titanium in T4CSZ did not seem to affect the isotherm shape of 4CSZ (figure 32c) with a comparable surface area of 32.7 m^2/g.

The physisorption analysis of 4PNZ revealed a similar isotherm (figure 33d), although BET calculation resulted in a surface area of 6.5 m^2/g, much lower than the one of samples otherwise obtained (i. e. 4CSZ and 6CSZ). The decrease in surface has been related to the increased size of the elongated particles, as shown by SEM analysis (see section 3.3).

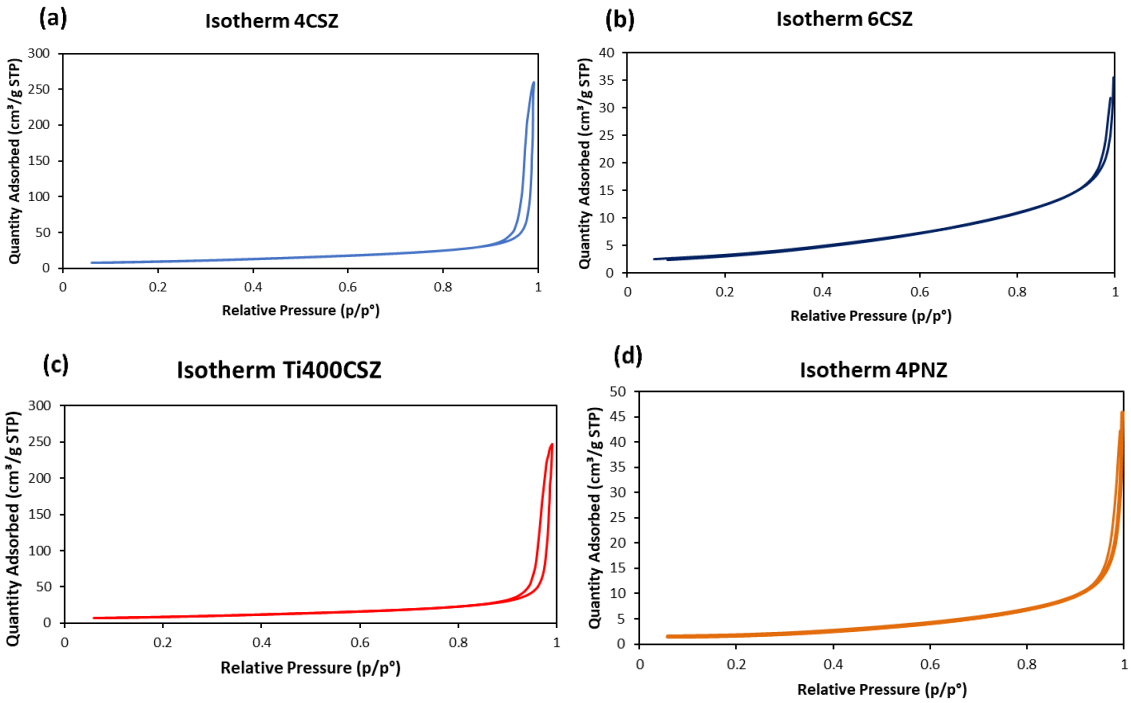

Figure 33 *Nitrogen physisorption isotherms of (a) 4CSZ, (b) 6CSZ, (c) T4CSZ and (d) 4PNZ.*

Figure 34 shows the type IV isotherm of commercial P25, typical of mesoporous materials with a surface area of 50 m^2/g.

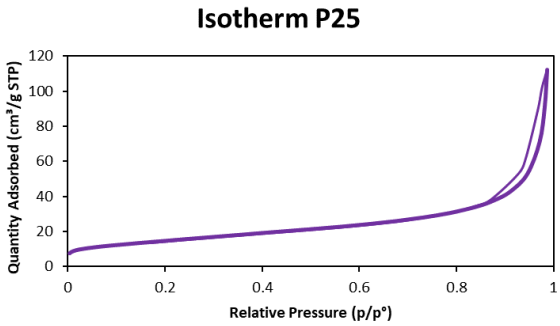

Figure 34 *Isotherm resulting from nitrogen physisorption analysis of P25.*

The collected isotherm of commercial SiO_2 was identified as a type III isotherm lacking hysteresis (figure 36a), suggesting a mainly non-porous material as confirmed by the very low value of surface area 1.5 m²/g (figure 35a). Conversely, SBA-15 had a type IV isotherm with a type-H2 hysteresis loop, typical of meso-porous materials with cylindrical pores (figure 35b) [53], and with reported surface area of 1024 m²/g and average pore diameter of 6.2 nm (figure 35c).

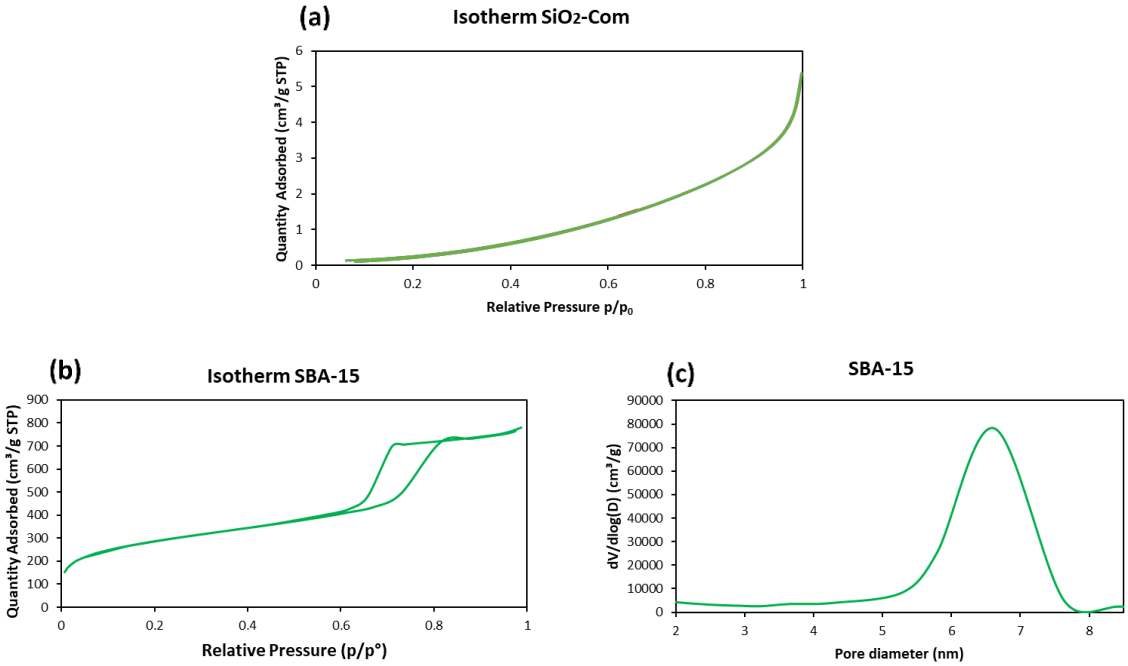

Figure 35 *Nitrogen physisorption results reporting isotherms of (a) SiO_2, (b) SBA-15 and pore radius distribution of (c) SBA-15.*

In Cerium-containing composites, the measured surface area of 41.8 m²/g and 162.4 m²/g for CCZ20 and CT20 respectively. The surface area of CCZ20 was found increased with respect to all synthesized ZnO-based materials, as well as the one of CT20 when compared to P25. Both materials showed a type IV isotherm. However, CCZ20 was identified as a micro-porous, with the possible presence of

macro pores, as suggested by the wide range of the pore size distribution (figure 36a, c). Conversely, CT20 showed a more ordered porous distribution and an average pore radius of 7.67 nm (figure 36d), which confirmed the meso-porous structure. Eventually, the given results were well in agreement with the different particle dimensions displayed by SEM analysis (see section 3.3)

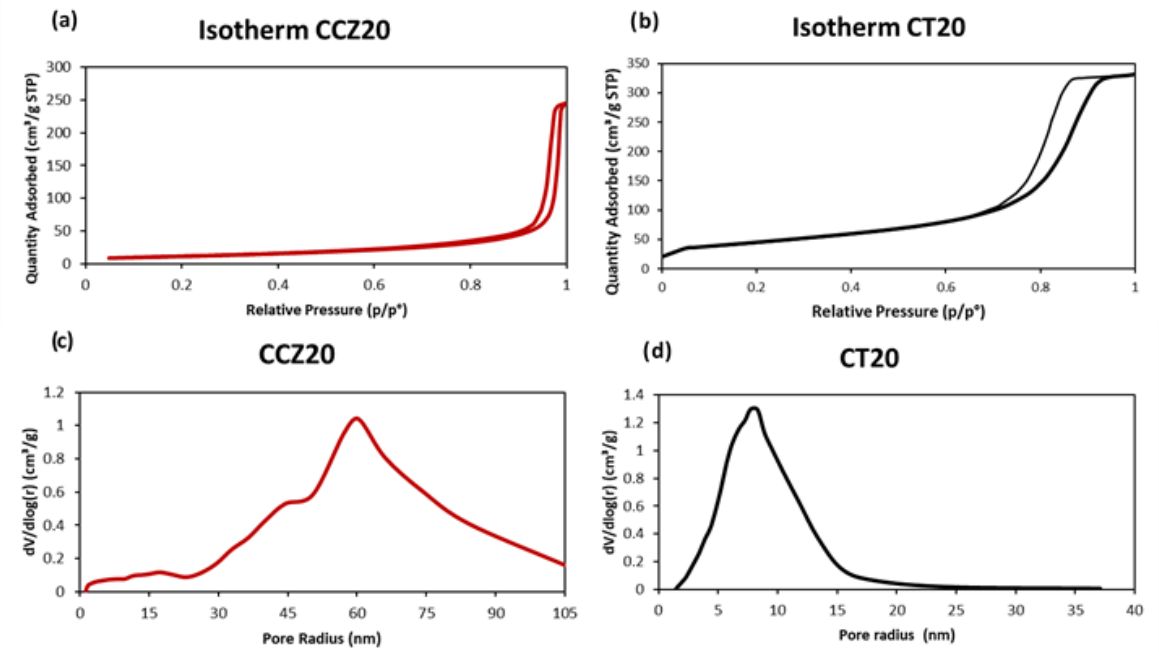

Figure 36 *Nitrogen physisorption results reporting isotherms of (a) CCZ20, (b) CT20 and pore radius distribution in (c) CCZZ0 and (d) CT20.*

3.5 Photoluminescence spectroscopy

Comparison of PL spectra of synthesized ZnO-based samples is reported in figure 38a. The emission spectra showed a visible light emission centred at 650 nm (red) and a UV near band edge emission (figure 37b), which is characteristic of ZnO [54]. The visible light emission is generally related to the presence of defects of different nature and is therefore dependent on doping, synthetic method and heat treatment [50]. The analysis of the visible/UV emission ratio reported in figure 38, showed a decrease in relative intensity, which was attributed to an increase in the UV emission of 6CSZ, when compared to 4CSZ. This result was attributed to the higher crystallinity of the former sample and expected decreased defect content. The introduction of Titanium also resulted in a decrease in defect-related emission in T4CSZ, if compared to 4CSZ. The latter feature was explained by either a physical shielding or an interaction between the two semiconductors, which improved the UV emission as already suggested [54]. Notably, the sample 4PNZ showed the highest visible emission (figure 38), which was attributed to the presence of an amorphous phase, which had been already detected by the XRD and XPS analysis, which would also be supported by the lower UV emission (figure 37b). These hypothesis would suggest that the ZnO emission at 650 nm is not likely related to oxygen vacancies, as already proposed [50], but more likely attributed to other types of defects, or a combination of differently emitting defects such as Zn vacancies, anti-site oxygen and oxygen interstitial [50, 54], forming intra-gap states in ZnO. In fact, the O/Zn ratio is considerably lower for 4CSZ than 6CSZ, while the same consideration is not valid for 4PNZ, which shows the highest emission with an O/Zn ratio lower than 6CSZ but not than 4CSZ (see section 3.2).

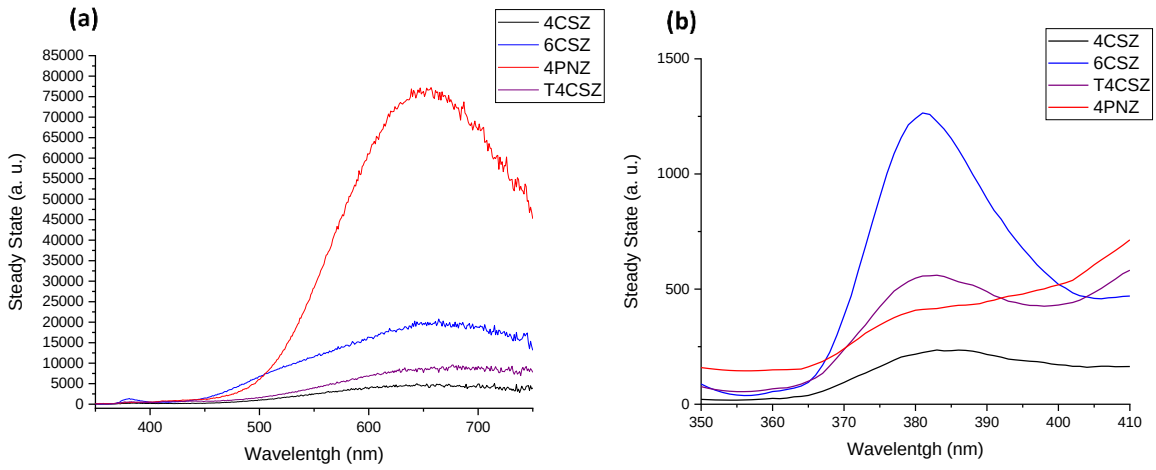

Figure 37 *PL emission spectra of all ZnO-based samples showing (a) the whole wavelength range and (b) and inset with UV emission. The investigating wavelength used was 300 nm.*

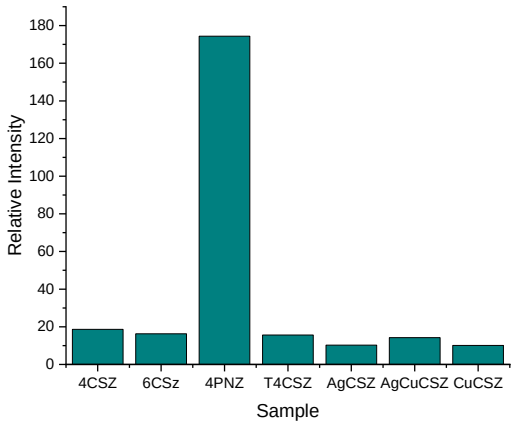

Figure 38 *Relative intensity given by visible/UV emission ratio of all samples.*

The effect of metal-loading on the PL spectrum was also evaluated. The visible emission was centred at 650 nm only for 4CSZ and AgCu4CSZ, while it was slightly blue-shifted (645 nm) or further red-shifted (690 nm) for Cu4CSZ and Ag4CSZ, respectively (figure 39a). As shown in figure 38, the presence of metals in Ag4CSZ and Cu4CSZ quenched the visible light emission and increased the UV photoluminescent response as already reported and attributed to either a surface plasmon resonance (SPR) effect [56, 57] or to the presence of a SC-metal or a SC-SC junction [58]. In the latter case, which an electron transfer from the metal oxide CuO or AgO to the CB of ZnO would likely increase the probability of the UV radiative decay, while intra-gap states electrons would be either deviated in the metal semiconductor VB or otherwise suppressed. Notably, the quenching effect was more attenuated for AgCu4CSZ, suggesting a possible synergistic effect restoring the visible light emission. Eventually, the nature of a visible peak around 430 nm was not clarified, as not elsewhere reported.

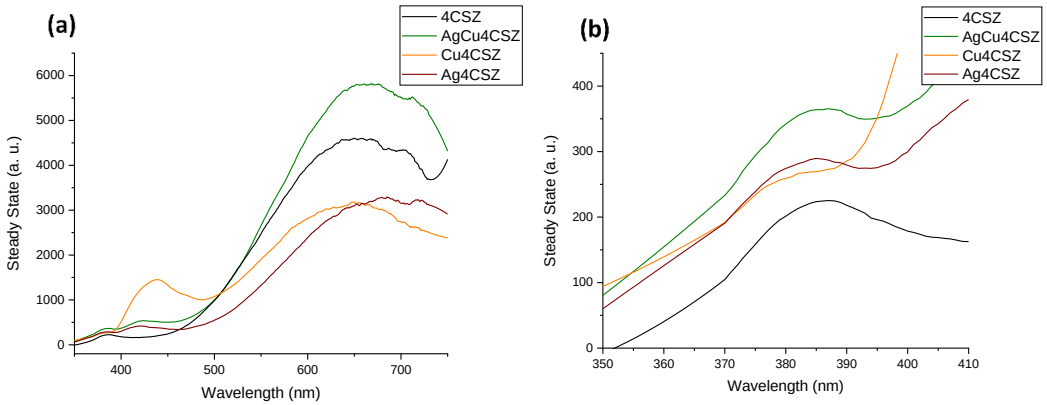

Figure 39 *PL emission spectra of metal-loaded ZnO-based samples showing (a) the whole wavelength range and (b) and inset with UV emission. The investigating wavelength used was 300 nm.*

The PL emission spectra of CCZ20 and its life-time decay are reported in figure 40a-b. The Ce-Zn composite showed a decreased visible emission with respect to the UV response (figure 41) which was attributed to either a lower number of defects, owed to the presence of Ce, or to a SC-SC junction electron exchange. The photoexcited electrons in ZnO would be transferred from the CB – or likely from near-CB intra-gap states – to the CB of CeO_2, thereby preventing the radiative decay of defect-related intra-gap states. In this hypothesis, the hole transfer from the CeO_2 VB to the ZnO VB would further favour the UV emission from ZnO. Notably, the time-resolved PL analysis seemed to show a shorter life-time decay (figure 40b) than 4CSZ, supporting an increase in faster – such as the UV-related – decays.

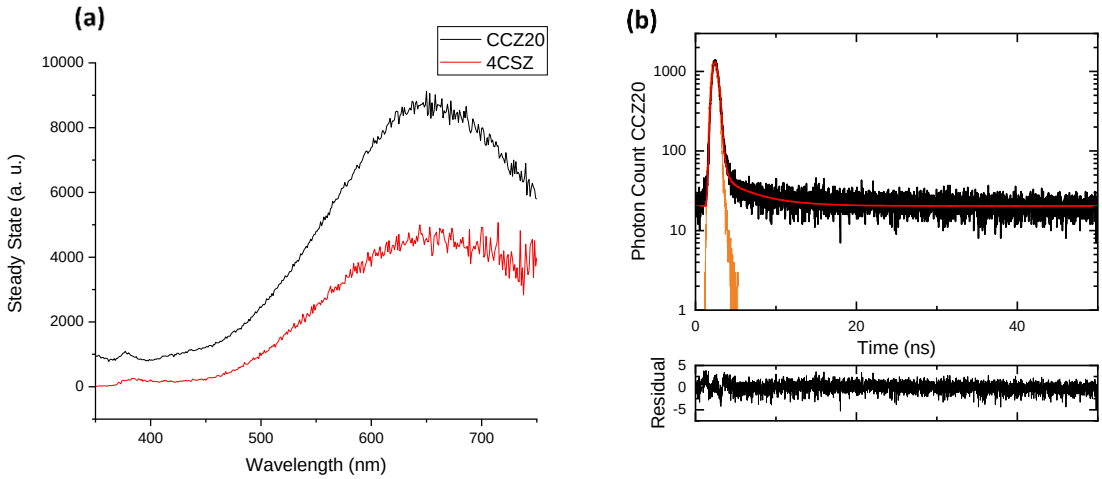

Figure 40 *(a) PL emission spectra of CCZ20 and 4CSZ and (b) time-resolved PL of CCZ20, measured using as excitation wavelength 300 nm and a LED emitting at 371.8 nm, respectively.*

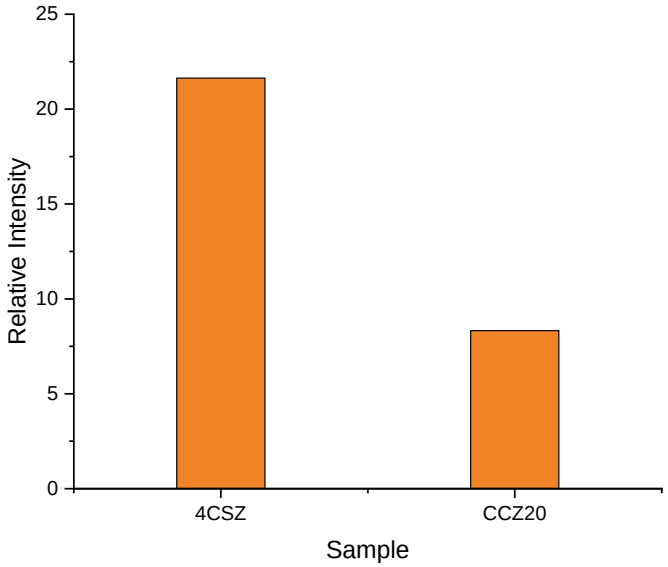

Figure 41 *Relative intensity given by visible/UV emission ratio*

The life-time of the visible emission was collected at 640 nm for all ZnO-based materials. The χ^2 value has been considered as measure of reliability when approaching unity (χ^2=1).

The investigated samples exhibited a tri-exponential decay (figure 42a-d), whose three time constants τ_{1-3} with their relative distribution are reported in table 4.

The PL photoluminescence and time decays were reported to vary with size, shape and defect content [59].

By comparison, the time constants of 4CSZ were much lower than the 6CSZ ones (table 4). The faster decay of 4CSZ was attributed to the higher defect density than 6CSZ, with the possible presence of non-radiative decay, as already suggested [59]. The latter effect seemed to be attenuated in 6CSZ, possibly owed to the improved crystallinity, thereby showing a slower decay and an increase of radiative recombining events (figure 42a-b). The radiative recombination was dominant in 4PNZ, which exhibited much higher time constants than 4CSZ and 6CSZ (figure 43a-b, d and table 4), which was instead attributed both to the presence the amorphous phase and to the increased particle size, which was reportedly related to increased time constants [59]. The presence of Ti on 4CSZ also resulted in elongated emission life-time, suggesting a possible exchange of photogenerated electrons between ZnO and TiO_2 semiconductors, with the consequent decrease of non-radiative recombination events (figure 42c) at the benefit of other radiative ones, such as the UV emission (figure 37a-b and 38).

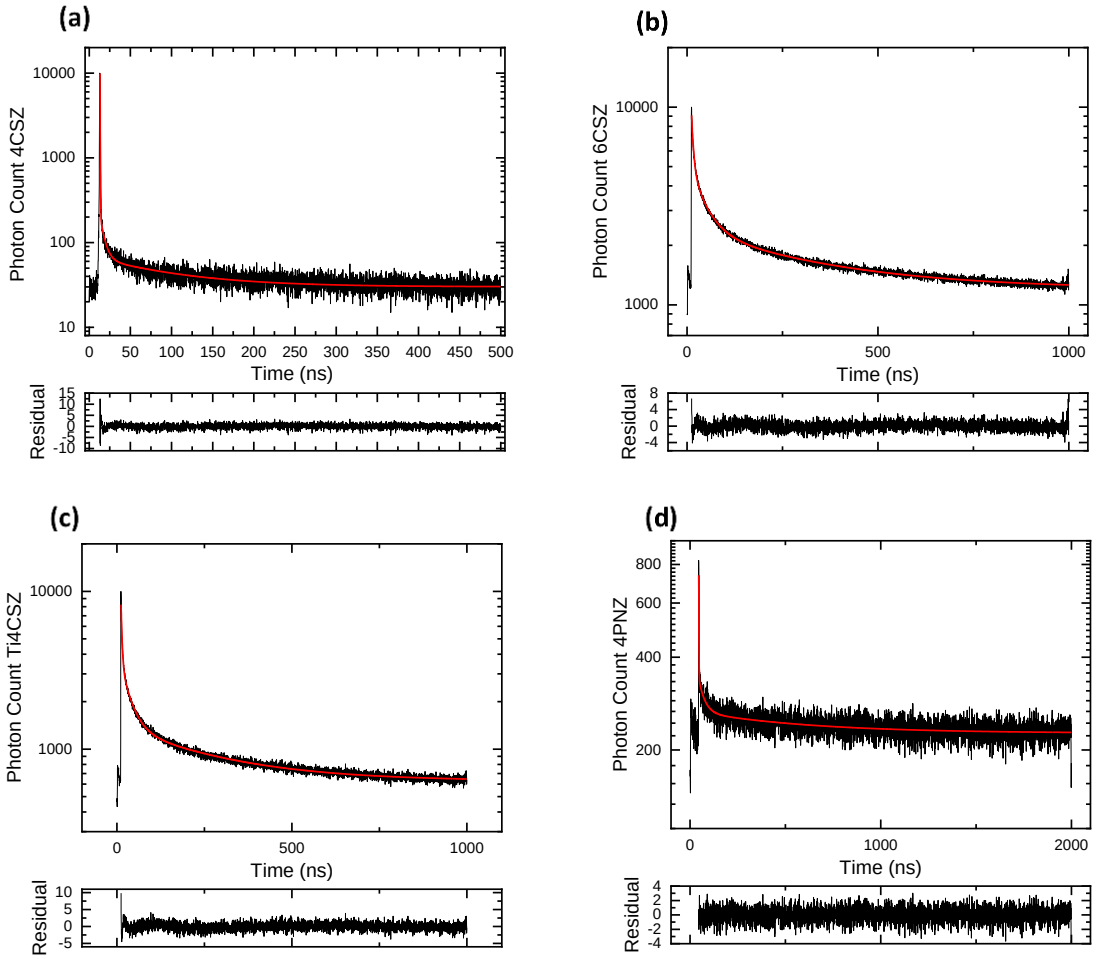

Figure 42 *Time-resolved PL of (a) 4CSZ, (b) 6CSZ, (c) Ti4CSZ and (d) 4PNZ. LED of 371.8 was used as the excitation source.*

Metal-loaded materials exhibited an overall faster decay with decreased time constants, with respect to all the other ZnO-based materials (table 4). The introduction of a Cu and Ag individually, resulted in a faster recombination rate which was related to the promotion of UV emission, as already reported [58], while the appearance of non-radiative decays was suggested to explain the a metal-SC charge exchange as responsible for the decreased visible-emission. Notably, AgCu4CSZ showed a slower decay compared to Ag4CSZ and Cu4CSZ (figure 43), suggesting the presence of a possible synergistic effect owed to the metal-metal and SC-metals interactions [60]. Longer life-times – or slower decays – were in accordance with the slightly higher visible emission of AgCu4CSZ, compared to the other metal-loaded samples (figure 38).

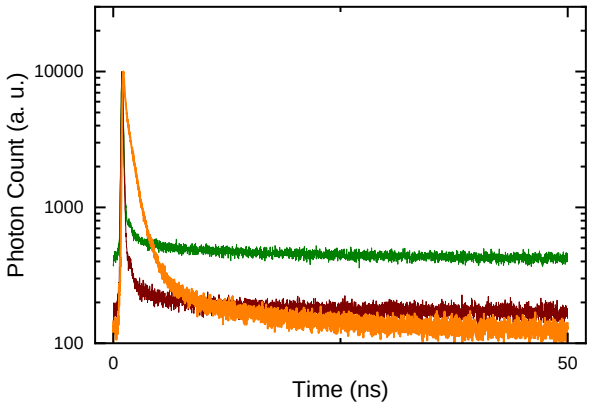

Figure 43 *Time-resolved PL comparison of metal-loaded ZnO as (green) AgCu4CSZ, (orange) Cu4CSZ and (dark-red) Ag4CSZ.*

Table 4 *Life-time parameters of samples investigated by time-resolved PL*

Sample	χ^2	τ_1 *(ns)*	*1Rel%*	τ_2 *(ns)*	*2Rel%*	τ_3 *(ns)*	*3Rel%*
4CSZ	1.165	0.23	48.85	5.19	9.89	93.76	41.26
6CSZ	1.125	5.09	4.42	38.21	18.84	325.92	76.75
4PNZ	1.009	0.99	2.53	31.04	9.37	587.66	88.10
T4CSZ	1.211	2.89	5.51	27.33	20.88	264.69	73.61
Cu4CSZ	1.113	0.16	7.61	0.97	71.60	8.40	20.79
AgCu4CSZ	1.074	0.04	55.01	1.65	5.93	16.10	39.05
Ag4CSZ	1.171	0.05	74.50	2.00	5.50	14.75	20.00

3.6 Reflectance spectroscopy

DRS performed on metal-sensitized 4CSZ is reported as the Kubelka-Munk function in figure 44. The analysis showed an increase in the visible absorption in presence of Ag in As4CSZ, which was more attenuated in AgCu4CSZ, possibly owed to the presence of Ag oxides species. A progressive towards blue-light absorption was also observed in Cu4CSZ, AgCu4CSZ and Ag4CSZ, for which it was more marked.

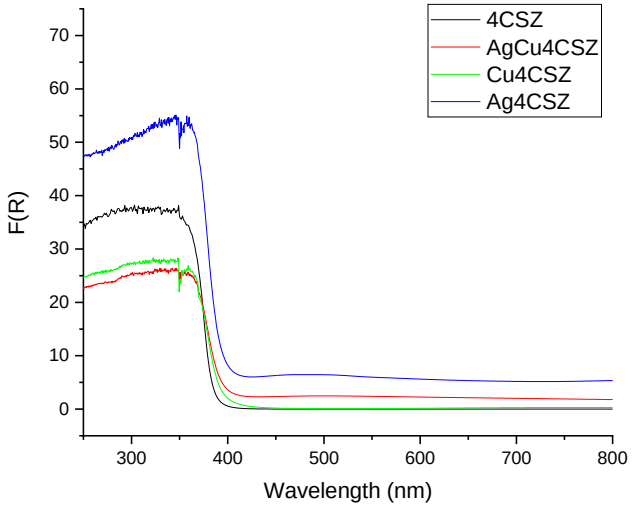

Figure 44 *Kubelka-Munk function obtained by DRS analysis of metal-sensitized samples.*

The introduction of cerium via co-precipitation method in the synthesis of CCZ20, resulted in a red shift of the absorption, indicated by the small tail in the blue region resulting from DRS analysis (figure 45). The latter shift was attributed to the presence of CeO_2, as confirmed by XRD analysis (see section 3.1). Conversely, DRS analysis of CT20 displayed a broader visible absorption band which was related to the achievement of TiO_2 band gap engineering, and likely related to the formation of a $Ce_xTi_{1-x}O_2$ mixed oxide (see section 3.1).

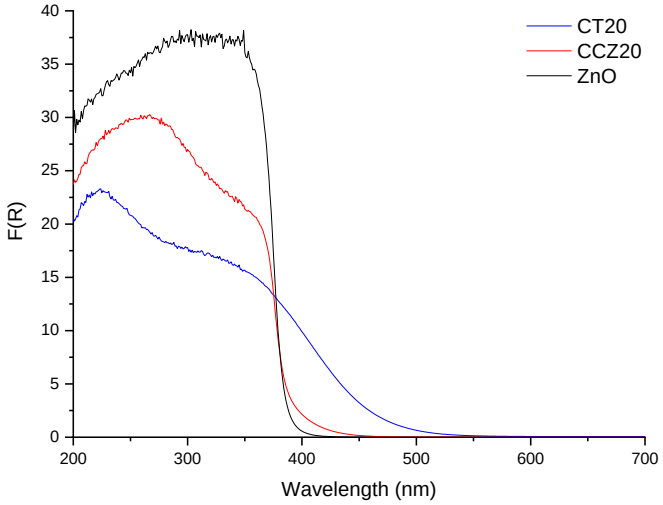

Figure 45 *Kubelka-Munk function obtained by DRS analysis of Ce-doped samples.*

3.7 TPD, TPR and TPO analysis

The results of He-TPD analysis of ZnO-based samples is reported in figure 45. The detected peak at 200 ^{o}C for 4CSZ, was attributed to surface-adsorbed carbonates released with the temperature increase. Above 600 ^{o}C the signal rises with the rising temperature, owed to the ZnO thermal decomposition in Zn and O_2 for the high temperature. The presence of Titanium in T4CSZ modified the releasing behaviour of adsorbed species, which seemed to be progressively released with the rising temperature. In this case the release was attributed both CO_2, H_2O and O_2. The TPD of CCZ20 showed three detectable peaks (figure 46). The first peak was likely related to the delivery of adsorbed carbonates, while the down-coming peak centred at 500 ^{o}C was related to the temperature-dependent reduction of superficial Ce^{4+} state into Ce^{3+} with consequent O_2 release and (see also figure 49b). Both T4CSZ and CCZ20 showed an increase in the signal related to the ZnO thermal decomposition only above 750 ^{o}C, indicating an increased stability of the materials.

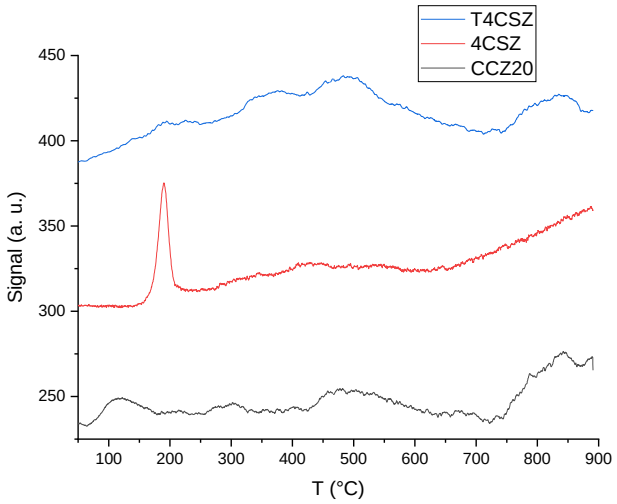

Figure 46 *He-TPD comparison of ZnO-based samples, pre-treated at 110 ºC for 1 h.*

The He-TPD performed on CT20, previously exposed to a CO_2 flux up to saturation, is reported in figure 47. The analysis showed 4 main peaks, which were identified as CO_2, N_2 or nitrates (NO_x) and H_2O at 100 ºC, 200 ºC and 300 ºC respectively. The less intense peak at 600 ºC was likely attributed to the O_2 release as reported [61].

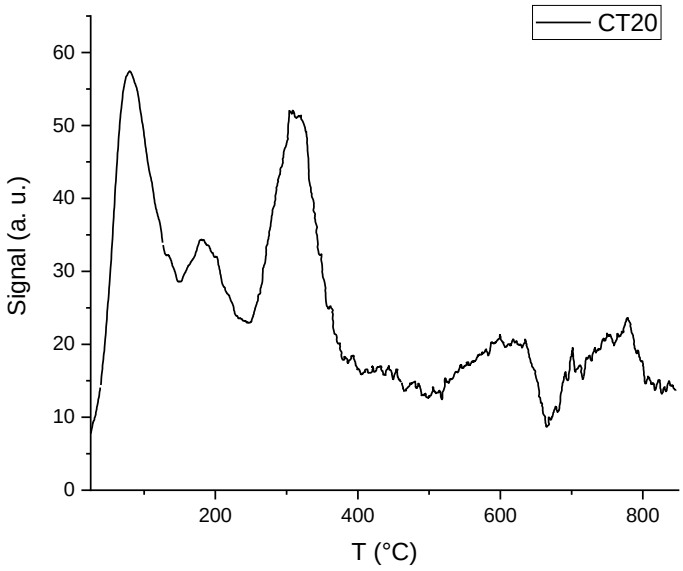

Figure 47 *He-TPD of CT20 previously exposed to a CO2-rich environment for 1 h at room temperature.*

TPO was performed for 4PNZ to assess the presence of surface-bound contaminants. However, of the release of organic compounds was not clear (figure 48).

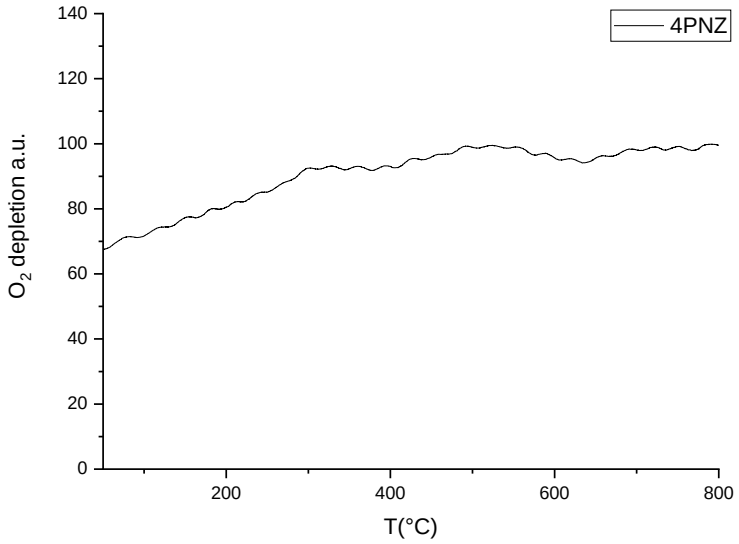

Figure 48 *TPO of 4PNZ, pre-treated at 110 ^{o}C for 1 h.*

Results of H_2-TPR analysis of ZnO-based sample is reported in figure 49 and was employed to elucidate some structural-dependent differences amongst samples. The weak peaks around 600 ^{o}C and above 800 ^{o}C of 4CSZ and 6CSZ were previously attributed to surface [62] and bulk Zn reduction. Moreover, T4CSZ and 4CSZ showed a negative peak, which is absent in 6CSZ, possibly related to residual H_2O interacting with non-stoichiometric ZnO and whose decomposition resulted in H_2 release. T4CSZ showed no peak at 600 ^{o}C, and a down-shifted peak above 800 ^{o}C, suggesting a possible effect of TiO_2-ZnO interaction on the surface-related reductive tendency of ZnO. Eventually, the behaviour of 4PNZ was still different when compared to the other ZnO-based materials, supporting the different nature of superficial and reticular O in ZnO.

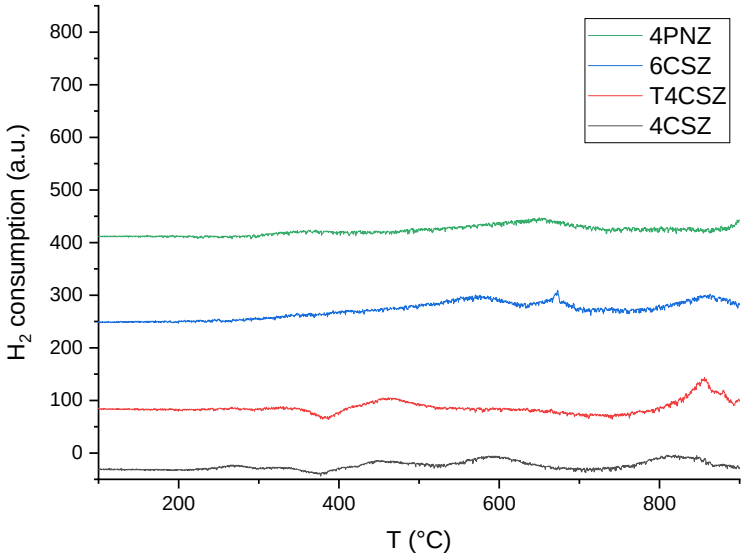

Figure 49 *H_2-TPR of ZnO-based samples, pre-treated at 110 ^oC for 1 h.*

The H_2-TPR results of CCZ20 was compared to 4CSZ (figure 50a), showing a pronounced peak at 400 ^oC, attributed to CeO_2 reduction. Notably, the typical CeO_2 reduction reaction presents on peak above 800 ^oC and a broader peak around 500 ^oC (figure 50b). The latter was attenuated in the CCZ20 pattern (figure 50a), suggesting an interference due to the presence of ZnO. In fact, it is possible that CeO_2 would reduce at the expenses of ZnO, as suggested both by the more pronounced peak at 400 ^oC and the absence of a peak at 600 ^oC, the latter attributed to surface located ZnO reduction (figure 50a). The peak at 800 ^oC was attributed to either bulk ZnO or CeO_2 reduction.

The effect of CeO_2 and TiO_2 combined interaction on the reducibility was also investigated and shown in figure 50b. Three main peaks were detected at 500 ^oC, 600 ^oC and 700 ^oC, and attributed to CeO_2, a mixed CeO_2-TiO_2 phase and TiO_2 reduction, respectively. In this case, the CeO_2-related peaks were reduced to a unique peak centred around 500-550 ^oC, while the peak attributed to the TiO_2 reduction was slightly upshifted. Therefore, the interaction resulted in increased reducibility for TiO_2 and decreased tendency to reduce of CeO_2, thereby supporting the existence of a CeO_2-TiO_2 mixed phase, as supported by XRD analysis (see section 3.1) in which the presence of Ce^{3+} and Ce^{4+} ions significantly affect the orbital structure of TiO_2, and *viceversa*.

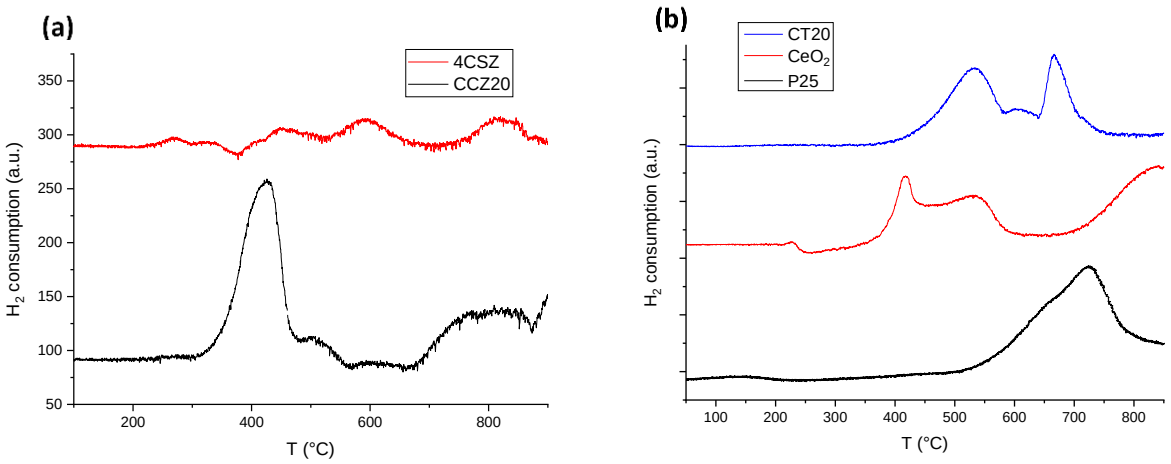

Figure 50 *H_2-TPR comparison of (a) CCZ20 and ZnO or (b) CT20, CeO_2 and TiO_2.*

The presence of metals on ZnO-based materials and their reducing behaviour was assessed by H_2-TPR analysis (figure 51). The reducing peak at 200 °C in Ag4CSZ and AgCu4CSZ was attributed to Ag^+ reduction to Ag^0, while the peak at about 250 °C in Cu4CSZ was previously attributed of monovalent copper, in CuO species [63]. The presence of Cu affected the reductive tendency of superficial ZnO as also suggested by PL analysis (see section 3.5), but not the bulk one, identified above 800 °C. However, the peak around 600 °C re-appeared in presence of Ag in Ag4CSZ, which conversely attenuated the peak at 800 °C. The latter was restored in AgCu4CSZ, suggesting an inter-metal interaction, able to affect both Cu and ZnO, comporting a respective decrease and increase of their reductive behaviours.

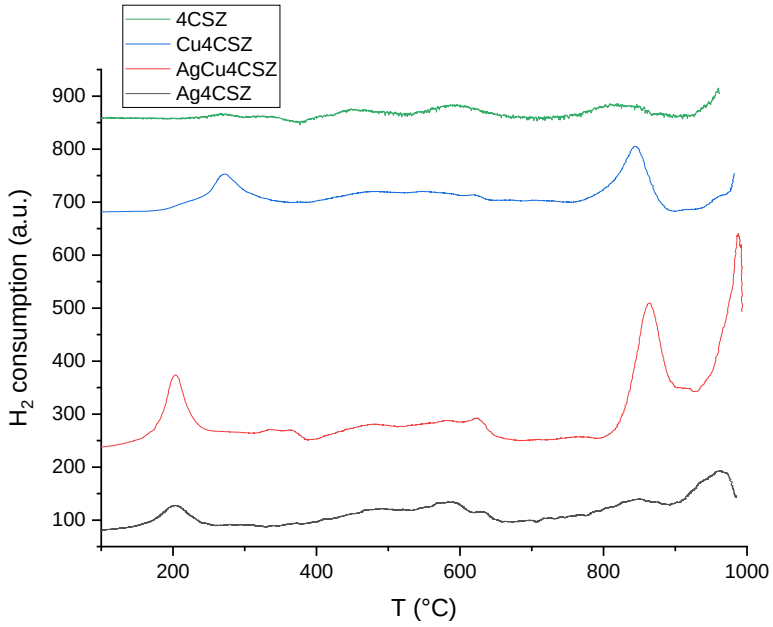

Figure 51 *H_2-TPR results and comparison of metal-loaded ZnO-based samples.*

3.8 Photo-catalytic conversion of CO_2

The photo-catalytic activity of all samples was measured in a 6 h-long experiment under UV light irradiation and CO_2/H_2O mixed gas flux in mild temperature and pressure conditions. Blank tests were performed before the activity tests, in order to avoid misinterpretations. The photo-catalytic performance was evaluated by comparison of CH_4 and O_2 yield (μmol· g_{cat}^{-1}). The detection of excess oxygen (non-stoichiometric) was employed as tool for the qualitative evaluation of the photo-stability of the material [64].

The photo-catalytic performance of ZnO-based materials with different synthetic parameters was evaluated and compared (figure 52). 6CSZ showed a slightly lower CH_4 production (0.12 μmol· g_{cat}^{-1}) compared to 4CSZ (0.16 μmol· g_{cat}^{-1}), but an improved photo-stability with decreased excess oxygen (figure 51), both attributed to the improved crystallinity. The decreased photo-activity was suggested as dependent by a decreased amount of surface defects, able to act as active sites for the reaction [65].

A remarkable photo-protection was achieved also by sensitizing with TiO_2, which decreased the extra oxygen production from 1.41 μmol· g_{cat}^{-1} for 4CSZ to 0.73 μmol· g_{cat}^{-1} for T4CSZ. Eventually, the synthetic hydrothermal method employed for the synthesis of 4PNZ was found detrimental for the photo-conversion performance, which overall showed the lowest CH_4 yield and the highest amount of excess oxygen (figure 52). The presence of amorphous islands, together with the low surface area and the increased recombination, suggested by PL data (see section 3.5), were considered responsible for the worsening of the catalytic activity and the overall charge mobility.

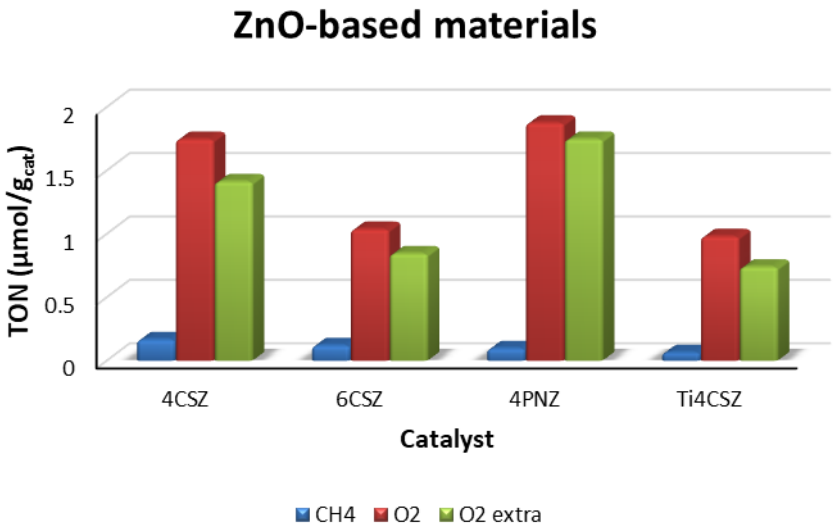

Figure 52 *Calculated TON of ZnO-materials exposed to 6 h UV illumination in a 13.33 CO_2/H_2O ratio flux.*

The effect of metal sensitising on ZnO photo-catalytic activity is reported in figure 53. The individual introduction of Cu or Ag resulted in an overall improved photo-stability, and a CH_4 yield of 0.06 μmol· g_{cat}^{-1} and 0.11 μmol· g_{cat}^{-1} respectively. The lowered performance was mainly attributed to the presence of residual NO_3^- species, able to interfere with the electron transfer and therefore to affect the formation of radical species involved in CH_4 formation. The formation of p-n junction between CuO and ZnO was reported to photo-catalytic properties of the material for organic compound degradation [58] and to favour the CO_2 photo-conversion [66], supporting that an electron transfer from CuO to ZnO would likely increase the recombination probability, as supported by the PL analysis (see section 3.5), thereby affecting the photo-oxidative ability of ZnO as otherwise suggested by H_2-TPR analysis (section 3.7). However, it is also possible that other forms of the metal, such as oxy-hydroxyl-metal, were present in the material, thereby further modifying the metal-SC interaction. In fact, the oxidation state of the metal was reported to affect the photocatalytic performance [67]. Notably, introduction of both Ag and Cu to ZnO in AgCu4CSZ led both to an increased production of excess oxygen and CH_4 yield, if compared to Ag4CSZ and Cu4CSZ individually. This result suggested a synergistic effect by means of a charge transfer effect, also supported by PL and TRP analysis (section 3.5 and 3.7).

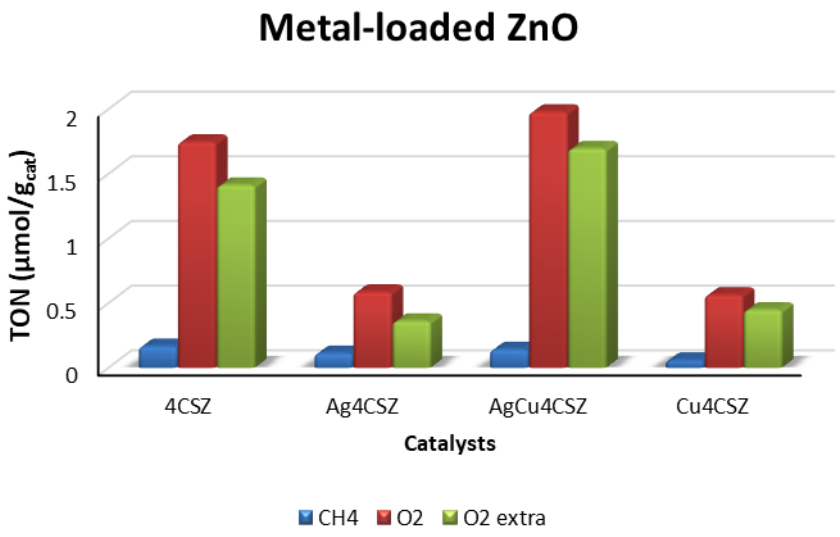

Figure 53 *Calculated TON of ZnO-materials exposed to 6 h UV illumination in a 13.33 CO_2/H_2O ratio flux.*

P25 produced 0.41 μmol· g_{cat}^{-1} of CH_4 in mild reaction conditions (figure 54). The presence of a SiO_2-based scaffold in SP10 and SBP10 were found to increase the photo-catalytic activity, despite the presence of only 10% in weight of P25, which resulted in a CH_4 yield of 0.67 μmol· g_{cat}^{-1} and 1.15 μmol· g_{cat}^{-1} respectively. As the increase was directly proportional to both the scaffold surface area and the pores density, it was suggested that the light had a major role in boosting P25 photo-catalytic performance. Moreover, the presence of SBA-15 seemed to also able modify the intermediate selectivity,

confirmed by the production of H_2, as side effect of H_2O oxidation. The latter effect is generally attributed to a faster HER evolution, with respect to CO_2 photo-conversion, which would support an increased hydrophilicity of the system. Notably, no H_2 production was detected when commercial SiO_2 was used as scaffolding material (figure 54). Eventually, TiO_2 was already reported as able to affect the release of oxygen via retention by oxygen vacancies [64]. A similar contribution in the oxygen retention by SiO_2 was proposed to explain the negative value of excess oxygen in both SP10 and SBP10, possibly favoured by the presence of – OH groups on the surface and by the more complex porous structure.

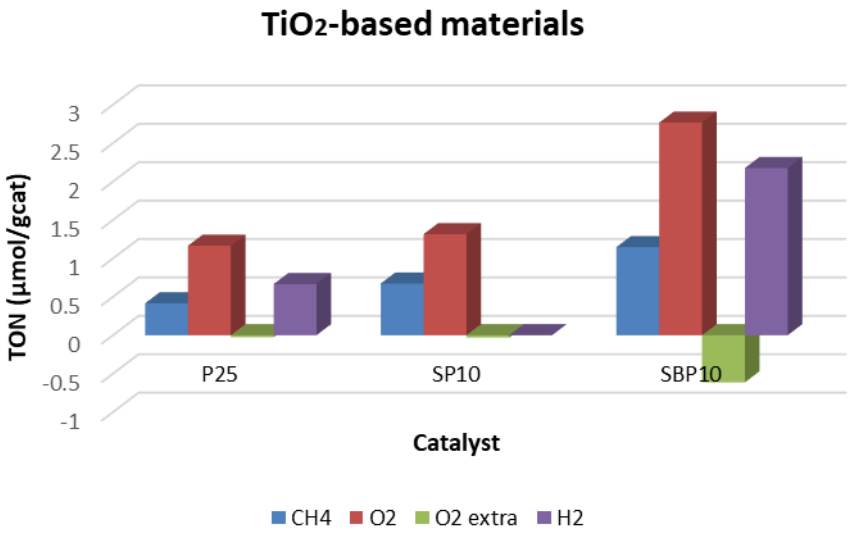

Figure 54 *Calculated TON of TiO_2-materials exposed to 6 h UV illumination in a 13.33 CO_2/H_2O ratio gas flux.*

As suggested by figure 55, the presence of Cerium in TiO_2 and ZnO structure suppressed the photocatalytic activity. The latter feature was attributed to the effect of the charge transfer at the Ce-Zn hetero-junction, which possibly resulted in the increase of non-radiative recombining events, as supported by the long decay, despite the reduced surface- and defect-related radiative emission in PL analysis (see Chapter 2). It is also possible that the photogenerated electrons led to the reduction of surface located Ce^{4+} centres at the expanses of the reaction intermediates, thereby resulting in oxygen release as reported in figure 55 and thus preventing the direct conversion of surface-adsorbed CO_2.

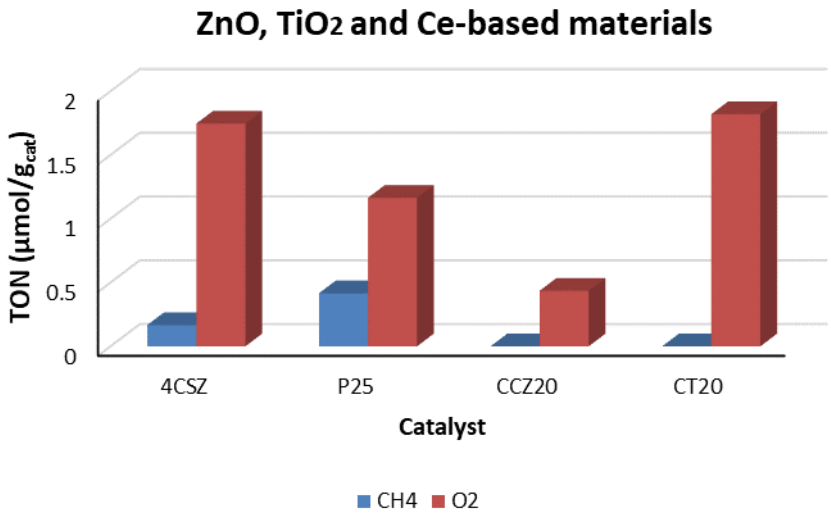

Figure 55 *Calculated TON of ZnO-materials exposed to 6 h UV illumination in a 13.33 CO_2/H_2O ratio flux.*

Owed to its intrinsic basic properties, ZnO was proposed for the combined CO_2 absorption and catalysis [68] and therefore tested in the CO_2 photo-conversion, in mild conditions. However, as shown in the the comparison of all synthesized samples (figure 56), TiO_2 showed a superior photo-catalytic performance over ZnO-based materials, which also affected the release of non-stoichiometric oxygen in the reaction medium. The lower activity of ZnO was explained as the effect of relatively strongly adsorbed carbonaceous intermediates, proposed as able to suppress the photo-catalytic activity [79]. For this reason, a series of techniques aiming to increase the photo-activity and/or improve the photo-stability, as well as to elucidate the driving mechanism, were explored to allow the design of more suitable photocatalysts.

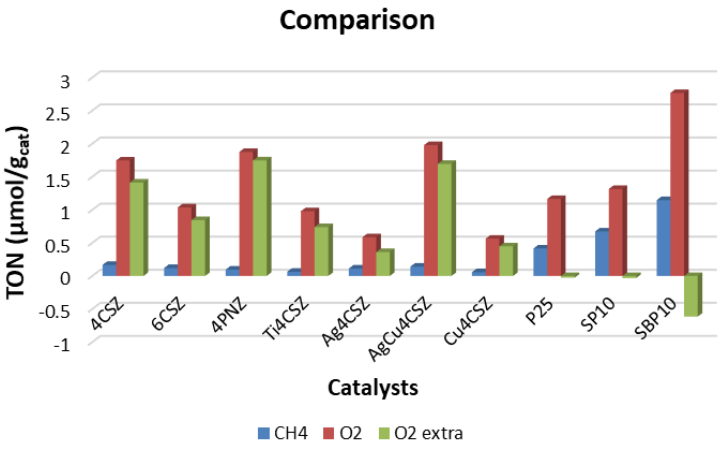

Figure 56 *Calculated TON of ZnO-materials exposed to 6 h UV illumination in a 13.33 CO_2/H_2O ratio flux.*

4. Conclusions

The effect of the crystallinity and morphology on the photocatalytic performance of ZnO and TiO_2 semiconductors was investigated, by employing different synthetic and annealing methods. Therefore, doping and metal sensitization by means of lanthanides, semiconductors or metals aimed to explore the exploitation of SC-SC and metal-SC as tools for the design of a more effective photo-catalyst, mainly by means of bandgap engineering and co-catalysis. Furthermore, optical and functional characterization were used for the investigation and elucidation of the possible reaction mechanism. The heating temperature, as well as the synthetic method employed were proved to affect both the visible photoluminesce and the photocatalytic properties via proposed structural and defect content modulation. The introduction of small amount of Titanium improved ZnO photo-corrosion by preserving the photocatalytic activity. The presence of metals, such as Ag and Cu, affected the optical properties of ZnO, by modifying the photoluminescent behaviour, and supporting a metal-SC charge exchange. The presence of Cu also affected the reducing ability of ZnO, in comparison with the bare counterpart. Moreover, the individual presence of the metals was found to better favour the photocatalytic performance and the photo-stability of ZnO – but still not with respect to bare ZnO – when compared to the multiple Ag-Cu sensitisation. Eventually, the introduction of Cerium via co-precipitation method in a 20:80 molar ratio had a different effect on either ZnO or TiO_2 materials, which was attributed to a diverse lanthanide-metal interaction. The structural characterization supported the presence of cerianite and wurtzite crystal phases in the CeO_2-ZnO composite, while a new and amorphous phase appeared in in CeO_2-TiO_2 mixed materials. As consequence, the latter showed a pronounced visible-light shift of the absorption, which suggested the achievement of bandgap engineering, as well as the ability to adsorb CO_2. However, none of the Cerium-doped materials was able to convert CO_2 into CH_4 in mild conditions, by also suggesting the importance of the role of the hydrophilicity of the system for a successful light-mediated conversion, when employing a n-type semiconductor. The latter conclusion was further supported by the SiO_2-mediated scaffolding of TiO_2, able to boost the CH_4 production both via increased light scattering and H_2O affinity, which also resulted in H_2 production. In conclusion, the too high affinity for CO_2 was proposed as the limiting factor for the ZnO-mediated CO_2 photoconversion which also relies on the efficient H_2O oxidation in order to occur.

5. Bibliography

[1] P. K. J. Robertson, Semiconductor photocatalysis: an environmentally acceptable alternative production technique and effluent treatment process, Journal of Cleaner Production (1996) 4(3, 4), 203-212

[2] Severin N. Habisreutinger, Lukas Schmidt-Mende and Jacek K. Stolarczyk, Photocatalytic Reduction of CO2 on TiO2 and Other Semiconductors, Angew. Chem. Int. Ed. (2013) 52, 7372–7408

[3] V. Subramanian, E. E. Wolf and P. V. Kamat, Catalysis with TiO2/Gold Nanocomposites. Effect of Metal Particle Size on the Fermi Level Equilibration, Am. Chem. Soc. (2004) 126(15), 4943-4950

[4] A. Tanaka, K. Hashimoto and H. Kominami, Visible-Light-Induced Hydrogen and Oxygen Formation over Pt/Au/WO3 Photocatalyst Utilizing Two Types of Photoabsorption Due to Surface Plasmon Resonance and Band-Gap Excitation, Am. Chem. Soc. (2014) 136(2), 586-589

[5] W. Tu, Y. Zhou, Q. Liu, S. Yan, S. Bao, X. Wang, M. Xiao and Z. Zou, Hybrid Nanosheets: Graphene-Promoted Selectivity of Photocatalytic-Driven Hydrogenation and Coupling of CO2 into Methane and Ethane, Weinheim Adv. Funct. Mater. (2013) 23, 1743–1749

[6] E. M. Andrews, J. Flake and Y. Fang, CO2 Electrocatalytic Reduction at Gold and Copper Electrodes: Role of Particle Size and Surface Chemistry, ECS Transactions (2015) 66, 22(3)

[7] W. Zhang, Y. Hu, L. Ma, G. Zhu, Y. Wang, X. Xue, R. Chen, S. Yang and Z. Jin, Progress and Perspective of Electrocatalytic CO2 Reduction for Renewable Carbonaceous Fuels and Chemicals, Adv. Sci. (2018) 5, 1700275, 1-24

[8] B. Han, J. Wang, C. Yan, Y. Dong, Y. Xu, R. Nie, H. Jing, The photoelectrocatalytic CO2 reduction on TiO2@ZnO heterojunction by tuning the conduction band potential, Electrochimica Acta (2018), doi: 10.1016/j.electacta.2018.07.216

[9] M. Fu, Y. Li, S. Wu, P. Lu, J. Liu, F. Dong, Sol-gel preparation and enhance photocatalytic performance of Cu-doped ZnO nanoparticles, Applied Surface Science (2011) 268, 1587-1591

[10] A. Kubacka, M. Fernandez-Garcia, G. Colon, Advanced Nanoarchitectures for Solar Photocatalytic Applications, Chem. Rev. (2012) 112, 1555–1614.

[11] A. Olivo, E. Ghedini, P. Pascalicchio, M. Manzoli, G. Cruciani and M. Signoretto, Sustainable Carbon Dioxide Photoreduction by a Cooperative Effect of Reactor Design and Titania Metal Promotion, Catalysts (2018) 8, 41, 1-22

[12] L. Zhu, H. Li, Pengfei Xia, Z. Liu and D. Xiong, Hierarchical ZnO Decorated with CeO2 Nanoparticles as the Direct Z-Scheme Heterojunction for Enhanced Photocatalytic Activity, ACS Appl. Mater. Interfaces (2018) 10, 39679−39687

[13] Severin N. Habisreutinger, Lukas Schmidt-Mende and Jacek K. Stolarczyk, Photocatalytic Reduction of CO2 on TiO2 and Other Semiconductors, Angew. Chem. Int. Ed. (2013) 52, 7372–7408

[14] P. Fageria, S. Gangopadhyay and S. Pande, Synthesis of Au/Zno and Ag/ZnO nanoparticle and their photocatalytic application using UV and visible light, RSC Adv (2014) 4, 24962–24972

[15] S. Wang, B. Zhu, M. Liu, L. Zhang, J. Yu, M. Zhou, Direct Z-scheme ZnO/CdS hierarchical photocatalyst for enhanced photocatalytic H2-production activity, Applied Catalysis B: Environmental (2018)

[16] R. Mohan, K. Krishnamoorthy and S. Kim, Enhanced photocatalytic activity of Cu-doped ZnO nanorods, Solid State Comunication (2012) 152, 375-380

[17] K. Reinhardt and H. Winkler, Cerium Mischmetal, Cerium Alloys, and Cerium Compounds, Wiley-VCH Verlag GmbH & Co. KGaA, (2012) 8, 41-54

[18] A. Mclaren, T. Valdes-Solis, G. Li and S. C. Tsang, Shape and Size Effects of ZnO Nanocrystals on Photocatalytic Activity, J. AM. CHEM. SOC. 2009, 131, 12540–12541

[19] G.-C. Yi, C. Wang and W. Il Park, ZnO nanorods: synthesis, characterization and applications, Semicond. Sci. Technol. (2005) 20, S22–S34

[20] S. Tsunekawa, J.-T. Wang and Y. Kawazoe, Lattice constant and electron gap energies of nano- and subnano-sized cerium oxides from the experiments and from first-principles calculation, Journal of Alloys and Compounds (2006) 408–412, 1145–1148

[21] Lianjun Liu, Ying Li, Understanding the Reaction Mechanism of Photocatalytic Reduction of CO2 with H2O on TiO2-Based Photocatalysts: A Review, Aerosol and Air Quality Research, 14: 453–469, 2014

[22] H. Wei, Y. Wu, N. Lun, C. Hu, Hydrothermal synthesis and characterization of ZnO nanorods, Materials Science and Engineering A (2005) 393, 80–82

[23] M. R. Parra and F. Z. Haque, Structural and optical properties of poly-vinylpyrrolidone modified ZnO nanorods synthesized through simple hydrothermal process, Optik (2014) 125, 4629–4632

[24] H. Wey, Y. Wu, N. Lun and C. Hu, Hydrothermal synthesis and characterization of ZnO nanorods, Materials Science and Engineering A 393 (2005) 80–82

[25] N. Lepot, M. K. Van Bael, H Van den Rul, J. D'Haen, R. Peeters, D. Franco and J. Mullens, Synthesis of ZnO nanorods from aqueous solution, Materials Letters (2007) 61, 2624 –2627

[26] M. R. Parra and F. Z. Haque, Structural and optical properties of poly-vinyl-pyrrolidone modified ZnO nanorods synthesized through simple hydrothermal method.

[27] T. Y. Ma, Z. Y. Yuan and J. L. Cao, Hydrangea-Like Meso-/Macroporous ZnO-CeO2 Binary Oxide Materials: Synthesis, Photocatalysis and CO Oxidation, Eur. J. Inorg. Chem. (2010) 716–724716

[28] Lianjun Liu, Ying Li, Understanding the Reaction Mechanism of Photocatalytic Reduction of CO2 with H2O on TiO2-Based Photocatalysts: A Review, Aerosol and Air Quality Research, 14: 453–469, 2014

[29] E. D. Sherly, J. J. Vijaya and L. J. Kennedy, Effect of CeO2 coupling on the structural, optical, and photocatalytic properties of ZnO nanoparticles, Journal of Molecular Structure (2015) 1099, 114-125

[30] Anushree, S. Kumar and C. Sharma, Synthesis, characterization and catalytic performance of ZnO–CeO2 nanoparticles in wet oxidation of wastewater containing chlorinated compounds, Appl. Nanosci. (2017) 7, 567–575

[31] H. Abdullah, M. R. Khan, M. Pudukudy, Z. Yaakob, N. A. Ismail, CeO2-TiO2 as a visible light active catalyst for the photoreduction of CO2 to methanol, Journal Of Rare Earths, (2015) 33(11), 1155-1161

[32] S. Rajendran, M. M. Khan, F. Gracia, J. Qin, V. K. Gupta and S. Arumainathan, Ce3+-ion-induced visible-light photocatalytic degradation and electrochemical activity of ZnO/CeO2 nanocomposite, Scientific Reports (2016) 6(31641), 1-11

[33] A. Olivo, W. A. Thompson, E. R. B. Bay, E. Ghedini, F. Menegazzo, M. Maroto-Valer, M. Signoretto *Investigation of process parameters assessment via design of experiments for CO2 photoreduction in two photoreactors*, Journal of CO_2 Utilization (2020) 36, 25-32

[34] P. C. Hiemenz and R. Rajagopalan, *Principles and Colloids Surface Chemistry,* Third Edition, Marcel Dekker Inc. (1997), Ch. 9, 405-439

[35] K. S. W. Sing, *Reporting Physisorption Data For Gas/Solid Systems,* Pure & Appl.Chem. *(1982) 54(11), 2201-2218*

[36] A. D. McNaught and A. Wilkinson, *IUPAC. Compendium of Chemical Terminology*, 2nd ed. (the "Gold Book"). Blackwell Scientific Publications, Oxford (1997).

[37] J. van Doorn, J. L. Bosch, R. J. Bakkum and J. A. Moulijn, *Temperature Programmed Oxidation as an Analysis Technique for Deactivated Hydrotreating Catalysts*, Studies in Surface Science and Catalysis (1987) 34, 391-402

[38] M. A. Reiche, M. Maciejewski, A. Baiker, Characterization by temperature programmed reduction, Catalysis Today (2000) 56(4), 347-355

[39] S. L.M. Schroeder and M. Gottfried, *Temperature-Programmed Desorption (TPD) Thermal Desorption Spectroscopy (TDS)*, Advanced Physical Chemistry Laboratory, FU Berlin (2002), 1-22

[40] T. H. Gfroerer, *Photoluminescence in Analysis of Surfaces and Interfaces*, Encyclopedia of Analytical Chemistry R.A. Meyers (Ed.) © John Wiley & Sons Ltd, (2000), 1-21

[41] H. G. Hecht, *The Interpretation of Diffuse Reflectance Spectra*, Journal Of Research of the National Bureau of Standards-A, Physics and Chemistry (1976) 80A(4), 567-582

[42] A. A. Bunaciu, E. G.a Udriştioiu and H. Y. Aboul-Enein, *X-Ray Diffraction: Instrumentation and Applications*, Critical Reviews in Analytical Chemistry, (2015) 45(4), 289-299

[43] F. T. L. Muniz, M. A. R. Miranda, C. M. dos Santos and J. M. Sasaki, *The Scherrer equation and the dynamical theory of X-ray diffraction,* Acta Cryst. (2016), A72, 1-6

[44] H. Konno, *Materials Science and Engineering of Carbon Characterization*, (2016) 8, 153-171

[45] T. Berhanu, Working principle of scanning electron microscope (2018), https://www.researchgate.net/publication/328019994_WORKING_PRINCIPLE_OF_SCANNING_ELECTRON_MICROSCOPE/citations

[46] Perkin-Elmer Corporation, *Analytical Methods for Atomic Absorption Spectroscopy,* © The Perkin-Elmer Corporation (1996), 1-5

[47] Ü. Özgür, Ya. I. Alivov, C. Liu, A. Teke, M. A. Reshchikov, S. Doğan, V. Avrutin, S.-J. Cho, and H. Morkoç, *A comprehensive review of ZnO materials and devices*, J. Appl. Phys. (2005) 98, 041301

[48] A. M. T. Silva, C. G. Silva, G. Drazic, J. L. Faria, *Ce-doped TiO_2 for photocatalytic degradation of chlorophenol,* Catalysis Today (2009) 144, 13–18

[49] [link] https://srdata.nist.gov/xps/

[50] C. Chandrinou, N. Boukos, C.Stogios and A.Travlos, PL study of oxygen defect formation in ZnO nanorods, Microelectronics Journal (2009) 40(2), 296-298

[51] K. M. Koczkur, S. Mourdikoudis, L. Polavarapu and Sara E. Skrabalak, Polyvinylpyrrolidone (PVP) in nanoparticle synthesis, Dalton Trans., (2015) 44, 17883–17905

[52] M. R. Parra and F. Z. Haque, Structural and optical properties of poly-vinylpyrrolidone modified ZnO nanorods synthesized through simple hydrothermal process, Optik (2014) 125, 4629–4632

[53] E. Ghedini, F. Menegazzo, M. Signoretto, M. Manzoli, F. Pinna and G. Strukul, Mesoporous silica as supports for Pd-catalyzed H_2O_2 direct synthesis: effect of textural properties of the support on the activity and selectivity, Journal of Catalysis (2010) 273, 266–273

[54] W. Shana, W. Walukiewicz, J. W. Ager and K. M. Yu, *Nature of room-temperature photoluminescence in ZnO*, Appl. Phys. Lett. 86, 191911 (2005)

[55] C. W. Zou, X. D. Yan, J. Han, R. Q. Chen, J. M. Bian, E. Haemmerle and W. Gao, Preparation and enhanced photoluminescence properties of ordered ZnO/TiO_2 bottlebrush nanostructures, Chemical Physics Letters (2009) 476, 84–88

[56] M. Mahanti and D. Basak, Cu/ZnO nanorods' hybrid showing enhanced photoluminescence properties due to surface plasmon resonance, Journal of Luminescence (2014) 145, 19-24

[57] B.J. Lawrie, R.F. Haglund Jr and R. Mu, *Enhancement of ZnO photoluminescence by localized and propagating surface plasmons, Optic Express (2209) 17(4), 2565-2572*

[58] K. Mageshwari, D. Nataraj, T. Pal, R. Sathyamoorthy and J. Park, *Improved photocatalytic activity of ZnO coupled CuO nanocomposites synthesized by reflux condensation method,* Journal of Alloys and Compounds (2015) 625, 362-370

[59] W. M. Kwok, A. B. Djurišić and Y. H. Leung, *Time-resolved photoluminescence from ZnO nanostructures,* Appl. Phys. Lett. (2005) 87, 223111

[60] O. Lupan, T. Pauporté, T. Le Bahers, B. Viana and Ilaria Ciofini, *Wavelength-Emission Tuning of ZnO Nanowire-Based Light-Emitting Diodes by Cu Doping: Experimental and Computational Insights*, (2011), https://doi.org/10.1002/adfm.201100258

[61] S. Watanabe, X. Ma and C. Song, *Characterization of Structural and Surface Properties of Nanocrystalline TiO_2-CeO_2 Mixed Oxides by XRD, XPS, TPR, and TPD,* J. Phys. Chem. C (2009), 113, 14249–14257

[62] M. Liang, W. Kang and K. Xie, *Comparison of reduction behaviour of Fe_2O_3, ZnO and $ZnFe_2O_4$ by TPR technique*, Journal of Natural Gas Chemistry (2009) 18, 110–113

[63] T. P. Maniecki, P. Mierczynski, W. Maniukiewicz, K. Bawolak, D. Gebauer and W. K. Jozwiak, *Bimetallic Au–Cu, Ag–Cu/CrAl3O6 Catalysts for Methanol Synthesis,* Catal. Lett. (2009) 130, 481–488

[64] A. Olivo, E. Ghedini, P. Pascalicchio, M. Manzoli, G. Cruciani and M. Signoretto, *Sustainable Carbon Dioxide Photoreduction by a Cooperative Effect of Reactor Design and Titania Metal Promotion,* Catalysts (2018) 8(41), 1-22

[65] F. Liu, Y. H. Leung, A. B. Djurišić, A. M. Ching Ng, W. K. Chan, *Native Defects in ZnO: Effect on Dye Adsorption and Photocatalytic Degradation,* J. Phys. Chem. C (2013) 117(23), 12218-12228

[66] T. P. Y. Taraka, A. Gautam, S. L. Jain, S. Bojja and U. Pal, *Controlled addition of Cu/Zn in hierarchical CuO/ZnO p-n heterojunction photocatalyst for high photoreduction of CO_2 to MeOH*, Journal of CO_2 Utilization (2019) 31, 207– 214

[67] Jianping Xiao and T. Frauenheim, *Theoretical Insights into CO_2 Activation and Reduction on the Ag (111) Monolayer Supported on a ZnO (0001) Substrate,* Phys. Chem. C (2013) 117(4), 1804-1808

[68] MYCS 2018: ZnO photocatalysts for enhanced CO2 conversion Danny Zanardo, Federica Menegazzo, Michela Signoretto, and Giuseppe Crucianib ISBN 978-88-86208-92-5

[69] A. Olivo, *Development of titanium dioxide based photocatalytic systems for CO2 photoreduction,* PhD Thesis, Ca'foscari University and Trieste University (2017)

Chapter 2

Nanostructured ZnO and TiO_2-based materials for the oxygen evolution reaction in photo-driven water splitting

1. Introduction

The development of renewable energy (RE) sources has been identified as one of the key factors both for the mitigation of climate change, aiming to lower fossil fuel-derived greenhouse gases (GHG) emission [1], and to respond the world's energy consumption, in order to face the challenge of increasing energy demand [2]. Although RE recently showed an increasing trend, the overall usage is still much lower than the evaluated potential [3] while features as efficiency, storage, costs and applicability still remain to be faced [3, 4].

Hydrogen (H_2) has been proposed as a promising alternative fuel, in virtue of its abundancy and energy yield, although transport and storage are still limiting factors to its practical employment [4]. In this regard, photocatalytic (PC) and photo-electrochemical (PEC) water splitting may provide both a fossil fuel-free alternative and a more versatile hydrogen generation [4].

In general, water splitting refers to a redox reaction involving water molecules followed by H_2 and oxygen (O_2) generation (equation 1, step I and II):

$$H_2O + 2h^+ \rightarrow 2H^+ + \frac{1}{2}O_2 \qquad E^0_{ox} = -1.23\ V \quad \text{(I)}$$

$$2H^+ + 2e^- \rightarrow H_2 \qquad E^0_{red} = 0.00\ V \quad \text{(II)}$$

Equation 1

PC water splitting relies on the use of a light-irradiated catalyst whose photo-generated electron-hole pairs are enough energetic to either oxidize or reduce water, or both. When the valence band (VB) of the catalyst is more positive than the water oxidation potential ($E_{O_2/H_2O} = 1.23\ V\ vs\ NHE$) or/and the conduction band (CB) is more negative than the hydrogen reduction potential ($E_{H^+/H_2} = 0.00\ V\ vs\ NHE$), the oxygen evolution (OER) and the hydrogen evolution (HER) reactions respectively occur [4]. When the photo-generated electron-hole pairs reach the semiconductor's surface, a difference of potential is generated at the solid-liquid interface and the charge transfer occurs in presence of an electron donor sacrificial agent [4].

In a PEC water splitting experiment, the light-irradiated semiconductor is generally used as either photo-anode or photo-cathode and coupled to an electrode able to catalyse the counter reaction (counter electrode, CE), with the addition of a reference electrode (RE) when studying the half reaction. Moreover, the presence of an electrolyte in the reaction medium is required to ensure the

closure of the circuit and to avoid any drop of the potential [4, 5, 6]. In virtue of their photo-excitable band gap, many transition metal oxides, such as TiO_2, ZrO_2, $KTaO_3$, $SrTiO_3$, ZnO as well as Fe_2O_3 were extensively studied and employed for both the PC and PEC water splitting [4, 5, 6]. Beside the band structure, several parameters were reported to affect the charge transfer process and therefore the photocatalytic performance, such as charge mobility, rate of electron-hole recombination and diffusion length, defect content, crystallinity and crystallite size, orbital structure, number of surface's active sites, size and shape of the material. Modulation of these properties have been largely attempted by mean of doping and/or the development of multicomponent materials [4, 5, 6]. However, much attention was also devoted to the study of nanostructured materials, for increased surface and facet exposure, as well as to the role of hetero-junctions – or bilayers – in the charge transfer process for the PC and PEC water splitting [6, 7]. As already reported [6], the coupling of two semiconductors may result in both improved charge exchange and mobility, with consequent modified photo-oxidation or reduction ability of the material, photoconversion efficiency and recombination rate. Bilayers are also used to enlarge the light absorption range or to increase the stability of the material. Owed to their low cost and large availability, TiO_2 and ZnO were widely studied for PC water splitting and proposed as photoanodes for PEC water oxidation [5, 8, 9]. However, being photo-corrosion one of the main limitations for ZnO-based materials, approaches like doping or thin layer deposition have been proposed to improve stability and/or to enhance the photocatalysis, such as ZnO/CdS composites or TiO_2@ZnO core@shell systems [9, 10, 11], the latter also showing an improved photocurrent when employed in PEC systems [10].

Cerium is a rare-earth element whose oxides are mainly present as CeO_2 with a cubic fluorite and Ce_2O_3 with a hexagonal structure. The CeO_2-TiO_2 mediated photocatalytic water splitting for the OER was reported in presence of a Pt-based co-catalyst and an electron acceptor [12], while electrocatalytic properties were proved for metal oxide-based CeO_2-containing systems – such as CeO_2/Co_3O_4 – showing a strong catalytic activity at low overpotential for the OER in water splitting applications, and higher current densities (at 1 V vs Ag/AgCl, in 0.1 M KOH electrolyte solution) when compared to other Co_3O_4-based systems containing Ni, TiO_2 or Fe_2O_3 [13].

Therefore, the synthesis of photo-active TiO_2 and ZnO-based nanostructured materials on FTO electrodes and their structural, optical, PC and PEC characterization aimed to clarify their potential in the OER under UV-Visible light illumination, as well as to assess the presence and the role of an IETP.

2. Materials and Methods

2.1. Experimental Procedure

2.1.1. Synthesis of rutile TiO_2 nanorods via hydrothermal method

2.1.1.1. Reagents

- Titanium butoxide, $Ti(OCH_2CH_2CH_2CH_3)_4$ (assay > 97 %) Sigma-Aldrich
- Absolute Ethanol, C_2H_6O Sigma-Aldrich
- Acetic acid, CH_3CO_2H Sigma-Aldrich
- Hydrochloric acid (36 %), HCl Sigma-Aldrich
- Distilled water
- Fluorine-doped tin oxide glass, FTO

2.1.1.2. Procedure

A TiO_2 seed layer has been prepared by using a 0.09 M titanium butoxide solution, containing 10 mL absolute ethanol and 2 mL acetic acid, which was then stirred for 2 h and aged for 24 h at room temperature. The as prepared solution was deposited on the conductive face of FTO glass by the use of a spin-coater (Ossila) alternating a 10-minutes-long heat treatment at 120 °C after each deposition for 4 cycles. Six replicates (T 1-6) were prepared and then annealed in air at 450 °C for 1 h in a thermal plate heater.

For TiO_2 nanorods (NR), a solution of 36% HCl and distilled H_2O in a 1:1 (V:V) ratio was prepared and stirred for 5 minutes (500 rpm). After the dropwise addition of titanium butoxide to obtain a 0.03 M solution and 10 minutes stirring (400 rpm), the solution was poured into a Teflon tube. Samples in series in a sample holder were then immersed in the solution and sealed into an autoclave for an aging process of 5 h at 150 °C. Samples were then cooled down, washed with distilled H_2O and stored.

2.1.2. Synthesis of ZnO nanorods via hydrothermal method

2.1.2.1. Reagents

- Zinc acetate dihydrate, $(CH_3COO)_2Zn{\cdot}2H_2O$ Sigma-Aldrich
- Absolute Ethanol, C_2H_6O Sigma-Aldrich
- Hexamethylenetetramine, $C_6H_{12}N_4$ (assay ≤ 99 %) Sigma-Aldrich
- Fluorine-doped tin oxide glass, FTO

2.1.2.2. Procedure

A 0.01 M solution of zinc acetate dihydrate in absolute ethanol was prepared and deposited on the conductive face of fluorine doped tin oxide (FTO) glass alternating seed layer deposition with a spin-coater and drying cycles at 120 °C, for 4 times. Samples were annealed in air at 450 °C for 1 h. For the hydrothermal synthesis of ZnO nanorods (NR), a solution of 0.1 M zinc nitrate hexahydrate (Sigma-Aldrich) and 0.1 M hexamethylenetetramine in H_2O was prepared and poured into a Teflon tube with the layered FTO samples, then transferred into an autoclave and treated at 95 °C for 3 h. Once cooled down, samples were extracted, washed with distilled H_2O and labelled Z 1-6. All samples were annealed in air for 2 h at 450 ° C in a furnace.

2.1.3. Adsorption of MB on Ce-Ti and Ce-Zn composites

2.1.3.1. Reagents

- Methylene Blue, $C_{16}H_{18}ClN_3S$ Sigma-Aldrich
- Distilled water

2.1.3.2. Procedure

A mother solution of $1 \cdot 10^{-3}$ M Methylene blue (MB) has been diluted up to the order of ~10^{-5} M in 50 mL of distilled H_2O. Henceforth, 25 mg of the catalyst (0.5 g/L), either CeO_2-ZnO (CCZ20) or CeO_2-TiO_2 (CT20), were dispersed in the MB solution under stirring (250 rpm) for a total of 3,5 h and 1,5 h respectively in dark conditions. At different times 2 mL aliquots were withdrawn and measured for UV-visible absorption. CT20 and CCZ20 had been previously synthesized (see Chapter 1, section 2.1.5).

2.1.4. TiO_2 layer deposition by atomic layer deposition (ALD)

Previously synthesized ZnO nanorods (batch 4) were exposed to 100, 200 and 800 cycles in a Ultratech Cambridge nanotech simply ALD instrument with G2 Savannah TiO_2 thermal program using tetrakis(dimethylamido) titanium (TDMAT) as precursor. Deposition occurred in presence of H_2O and with a deposition rate of 0.4 Angstrom/Cycle. Samples were labelled as $1TiO_2$@ZnO, $2TiO_2$@ZnO, $8TiO_2$@ZnO accordingly.

2.1.5. Cerium layer deposition via spin-coating

2.1.5.1. Reagents

- Ammonium Cerium(IV) nitrate, $Ce(NO_3)_6(NH_4)_2$ Sigma-Aldrich
- Ethanol 95%

2.1.5.2. Procedure

A 10^{-3} M mother solution of Cerium ammonium nitrate [CAN, $Ce(NO_3)_6(NH_4)_2$] and 95% ethanol solution has been further diluted up to 10^{-5} M and both solutions were used for layer deposition on previously synthesized ZnO (batch 3) and TiO_2 nanorods. By mean of a spin coater, 125 µL of each solution was gently poured on the nanorods, dried at 3000 rpm for 1 minute and annealed at 120 °C. The use of different concentrations aimed to obtain the deposition of different amount of Cerium and the coating procedure was repeated twice per sample. Samples were labelled as high (H) and low (L) according to the concentration used, namely HCe-Zn and LCe-Zn for ZnO NR, HCe-Ti and LCe-Ti for TiO_2 NR and air annealed for 2 h at 450 °C (see table 1).

2.1.6. Photocatalytic test for MB degradation

2.1.6.1. Reagents

- Methylene Blue, $C_{16}H_{18}ClN_3S$ Sigma-Aldrich
- Distilled water
- Sodium hydroxide, NaOH Sigma-Aldrich

2.1.6.2. Procedure

A mother solution of Methylene blue (MB) $1 \cdot 10^{-3}$ has been diluted (pH~7) in 100 mL of distilled H_2O. Henceforth, 50 mg of catalyst (0.5 g/L), either CCZ20 or CT20, were dissolved in the MB solution under stirring (250 rpm) conditions and exposed to a total of 30 minutes of dark before 3 h and 1,5 h of light respectively, with a solar spectrum simulator (LOT-Quantum design) at 1 kW/m^2 irradiance (AM1.5G). At different times 2 mL aliquots were withdrawn and the absorption was measured with a UV-Vis spectrophotometer (Cary5000, Agilent technologies). The used catalysts were recovered by centrifuging the original reaction solutions, containing either CCZ20 or CT20, at 4000 rpm for 2 minutes. The supernatant was discarded, and samples were let to dry overnight (18 h) at room temperature. Therefore, samples were weighted and then re-dispersed into a 1 M NaOH solution for 5 minutes, before being centrifuged and washed in distilled water once. Both NaOH- and water-based supernatants were collected and analysed in a spectrophotometer.

2.1.7. Photo-electrocatalytic test for MB degradation

2.1.7.1. Reagents

- Sodium sulphate, Na_2SO_4 Sigma-Aldrich
- Distilled water

2.1.7.2. Experimental

A 10^{-5} M MB (pH=7.6) aqueous solution was prepared using a 0.5 M Na_2SO_4 water solution as both solvent and electrolyte. The photo-electrocatalytic tests were run in a 50 mL quartz electrochemical cell with a three-electrode set up using Pt foil as CE and SCE as RE, with or without the application of a 0.2 V (0.44 V vs RHE) bias in both dark and light conditions. The effect of Pt wire as WE was also evaluated.

2.2. Characterization

2.2.1. Optical and structural characterization

The diffused reflectance (R%) spectra of powder samples and absorption spectra were measured with a Cary 5000 UV-Vis spectrophotometer (Agilent Technology). Photoluminescence analysis was carried out with a spectrofluorometer (Edinburg Instrument FLS-980) using 300 nm as the investigating wavelength, at room temperature. Time resolved photoluminescence (TRP) of the visible emission (550 nm and 600 nm) was measured using a LED (371.8 nm) as investigating light source and the time decays were fitted as previously reported (see chapter 1), to obtain the lifetime parameters.

SEM-EDX analysis was performed with FEI Magellan 400 SEM instrument. XRD spectra were collected with a Panalytical Empyrean XRD Diffractometer and analysed by High Score Plus software followed by Rietvield refinement.

2.2.2. Rutherford Backscattering Spectrometry

Rutherford Backscattering Spectrometry (RBS) is a technique widely employed for the study of surface layers. The analysis relies on the use of protons bombarded on a solid target, with energies ranging from 0.5 to 4 MeV and angles between 150-170°. The energy E_1 of the backscattered protons is related to the energy of the incident particle E_0 by

$$E_1 = KE_0$$

Equation 2

In which K is a kinematic factor function of the nuclear mass of the target at rest and of the scattering angle, thereby allowing the quantitative determination of the composition of the material and depth profiling of individual elements. The technique has a variable investigating depth ranging from 2 to 20 µm, and the major drawback of low sensitivity for light elements [14].

RBS analysis was performed by using $^4H^+$ particles with incident energy of 2.0 MeV and an angle of 160°, using SiO_2 as the calibration standard.

2.3. Photo-electrochemical test for water oxidation

All PEC experiments were performed into a 50 mL photoelectrochemical quartz cell containing 20 mL of reaction medium with 0.5 M Na_2SO_4 as electrolyte. The measured current density (A/cm^2) were normalized to the surface of the WE. All data were analysed with a XM/ECS Software.

2.3.1. Linear sweep and cyclic voltammetry

Voltammetry methods relies on the measure of the current produced by applying a defined voltage profile as function of time, by mean of a potentiostat. A variable voltage is therefore applied between a working electrode (WE) and a reference electrode (RE) in solution. The measured current is function of the electrode type, working surface, applied voltage and solution conductivity. In fact, aqueous solutions generally require electrolytes to grant the current flow, by completing the electrochemical circuit. Voltammetry technique are commonly employed to investigate the electrochemical and surface properties of working electrodes, for the evaluation of the electrochemical bandgap and to elucidate the role of a system in an redox reaction [3].

Linear sweep voltammetry (LSV) and cyclic voltammetry (CV) are two of the most employed voltammetry techniques. The potential *E* is changed in time, and the change rate is defined as the scan rate v and measure in $V \cdot s^{-1}$

$$v = \frac{dE}{dt}$$

Equation 3

In an LSV experiment, the potential is linearly changed from an initial E_i to a final E_f potential, while in CV the potential is scanned in one direction and then reversed up to E_i, in a defined range. The charging I_c and a Faradaic I_F current contributions determines the current response *I*, and respectively related to the electrode interfacial charging and to the electron transfer at the electrode surface,

$$I = I_c + I_F = vC_{DL} + I_F$$

Equation 4

where C_{DL} is the capacitance of the double layer [15]. The latter can be evaluated by CV experiments, as the proportionality constant of the average current function of the scan rate, according to the following relationships [16, 17, 18]:

$$i = Cv \qquad \text{(I)}$$

$$\frac{I_a - I_c}{2} = C_{DL}\frac{dE}{dt} \qquad \text{(II)}$$

Equation 5

Where in general i is the current, C the capacitance and v the scan rate, while Ia and Ic.
Eventually, in CV experiments, the current versus potential plot at different scan rates is also indicative of the stability of the material which can be evaluated with a potential versus time plot. The cathodic or anodic current-to-voltage curve is sometimes used to evaluate the stability of the material, at a fixed scan rate, over a high number of consecutive cycles [19].

Photo-electrochemical (PEC) characterization was performed with a potentiostat (ModulabXM, Solartron analytical). Linear sweep voltammetry (LSV) was performed in a three-electrodes configuration using ZnO NR/FTO- or TiO2 NR/FTO-based samples as photoanodic working electrodes (WE), a Platinum foil as counter electrode (CE) and a saturated calomel electrode (SCE) as reference electrode (RE). The oxygen evolution reaction (OER) was studied both in dark and light conditions (UV-Vis range AM 1.5G) in the potential range from 0.68 to 2.08 V (vs RHE).
LSV of all samples was measured in both dark and upon UV-visible light illumination with a scan rate of 10 mV/s. The current produced was used to evaluate and compare the oxidising properties of the materials.

Cyclic voltammetry (CV) was performed within the potential window 0.6-1.0 V (vs RHE) by using different scan rates starting from 20 to 200 mV/s, in both light and dark conditions. The potential applied was converted into V vs RHE according to equation 6 [19]

$$E_{RHE} = E^0_{SCE} + E_{SCE} + 0.059 \cdot pH$$

Equation 6

where E_{SCE} is the applied potential versus the RE while E^0_{SCE} is the standard potential (vs RHE) of the RE.

2.3.2. Electrochemical impedance spectroscopy

Electrochemical impedance spectroscopy (EIS) is widely used to evaluate the resistance to the current flow of an electrochemical system. The techniques relies on the measure of the system response to the application of a small amplitude AC potential, at different frequencies. In these conditions, the sinusoidal perturbation result perturbation results in a sinusoidal response signal shifted in phase. EIS analysis is informative on the interface behaviour and structure and may be employed for the evaluation of the resistance to the current flow, as well as of the double layer capacitance [17]. The resistance R is defined by the Ohm law as:

$$R = \frac{V}{I}$$

Equation 7

Where I and V are the current and voltage, respectively. The impedance Z is the analogous of the resistance in a real circuit, in which the applied potential E_t and the response signal I_t are expressed as periodic function of time

$$Z = \frac{E_t}{I_t} = \frac{E_0 sin(\omega t)}{I_0 sin(\omega t + \varphi)} = Z_0 \frac{sin(\omega t)}{sin(\omega t + \varphi)}$$

Equation 8

In which ω is the frequency, E_0 is the amplitude of the signal, and I_0 is the amplitude of the signal response I_t, with a shifted phase φ.

By expressing the impedance as a complex function, by means of Euler relationship, the following expression is obtained (equation 9),

$$Z(\omega) = \frac{E_0 sin(j\omega t)}{I_0 sin(j\omega t - \varphi)} = Z_0(cos\varphi + jsin\varphi)$$

Equation 9

In which the impedance is a complex number, with a real $cos\varphi$ and an imaginary $jsin\varphi$ component. The characteristic semicircle obtained by plotting the imaginary versus the real part is known as Nyquist plot (figure 57) [20].

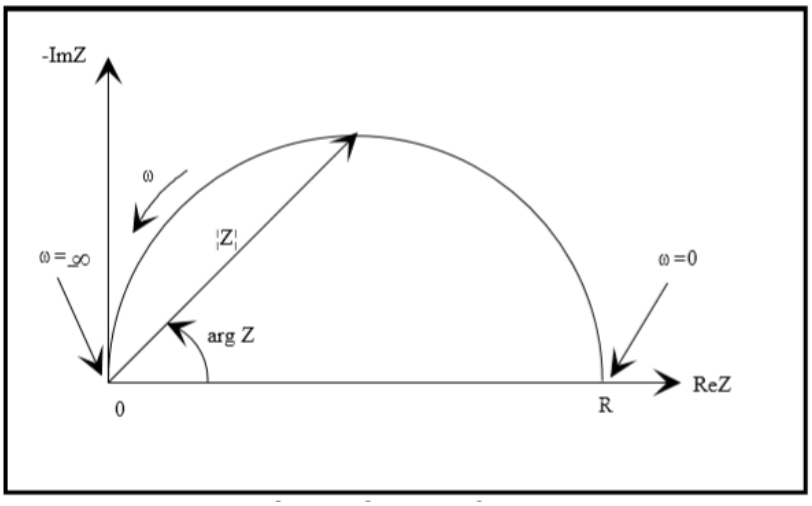

Figure 57 *Nyquist plot obtained by plotting the negative imaginary part ImZ versus the real part ReZ.*

The diameter of the semicircles in the Nyquist plot is proportional to the resistance [19].
For the evaluation of the resistance and of the double layer capacitance, a simplified Randles cell composed by a solution resistance (resistor 1, R_1), a charge transfer resistance (resistor 2, R_2) and a double layer capacitance, was used as equivalent circuit to fit the Nyquist plots (figure 58).

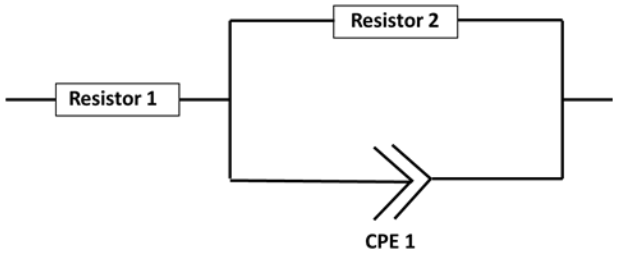

Figure 58 *Equivalent circuit*

However, several factors such as surface roughness, reactivity, porosity and inhomogeneity generally result in a non-linear capacitor behaviour [21, 22, 23]. In such a case, the capacitance is accounted by a constant phase element (CPE) and related to the impedance as follow:

$$Z_{CPE} = \frac{1}{Q(\omega j)^{\alpha}}$$

Equation 10

Where Q is the capacitance of the CPE, ω is the frequency and the exponent α is 1 for an ideal capacitor and less (0> α >1) otherwise [21, 22, 23]. The double layer capacitance C_{DL}^{α} is usually estimated according to the equation

$$C_{DL}^{\alpha} = \frac{Q}{\left({}^{1}/_{R_p}\right)^{1-\alpha}}$$

Equation 11

In which R_p indicates the resistance parallel to the CPE, which is R_2 in this case. However, a different model was proposed for heterogeneous catalysts in which the double layer capacitance is given by equation 12 as

$$C_{DL}^{\alpha} = \left[Q\left(\frac{1}{R_1} + \frac{1}{R_2}\right)^{\alpha-1}\right]^{1/\alpha}$$

Equation 12

With R_1 and R_2 as previously described and as displayed in figure 58. The latter model was therefore employed for the evaluation of C_{DL}^{α} [24].

Electrochemical impendence spectroscopy (EIS) measurement were performed at an applied bias of 0.2 V (or 0.44 V vs RHE) and a frequency range of 10^5 and 10^{-2} Hz using a Ag/AgCl electrode as RE. The Nyquist plots obtained were analysed with a simulation software RelaxIS 3.0.13.18 (impendance spectrum analysis) and compared to an equivalent RC circuit to obtain the resistance and the capacitance.

2.3.3. Chrono-amperometry

The chrono-amperometry experiment was employed to evaluate the photo-stability and the photo-driven current response of the material, which is collected while alternating light and dark cycles for constant time intervals. The transient photocurrent obtained may be related to photo-

electrons passing from the valence to the conductive band as well as to the charge accumulation at the solid-liquid interface [19].

The chrono-amperometry experiment was run by measuring the transient photocurrent i_{ph} for a period of 1.5 min of light and dark with or without the application of a constant bias for 20 minutes, followed by LSV investigation. The 1.5 minute-interval has been purposely chosen to relate the current depletion to the stability of the material, as indicative of ongoing photo-corrosion, and to the presence of defects [19].

Table 5 *Resuming of synthesized materials.*

Sample	Composition	Synthetic method	Heat Treatment (°C)	Duration (h)
ZnO NR	ZnO	Hydrothermal method	450	2
TiO_2 NR	TiO_2	Hydrothermal method	450	2
1TiO_2@ZnO	100 cycles TiO_2 on ZnO nanorods	ALD	-	-
2TiO_2@ZnO	200 cycles TiO_2 on ZnO nanorods	ALD	-	-
8TiO_2@ZnO	800 cycles TiO_2 on ZnO nanorods	ALD	-	-
HCe-Ti	high CeO_2 molar concentration on TiO_2 nanorods	Spin-coating deposition	450	2
LCe-Ti	low CeO_2 molar concentration on TiO_2 nanorods	Spin-coating deposition	450	2
HCe-Zn	high CeO_2 molar concentration on ZnO nanorods	Spin-coating deposition	450	2
LCe-Zn	low CeO_2 molar concentration on ZnO nanorods	Spin-coating deposition	450	2
CT20	CeO_2-TiO_2 composite	Co-precipitation via wet chemistry	400	4
CCZ20	CeO_2-ZnO composite	Co-precipitation via wet chemistry	400	4

3. Results and Discussion

3.1. Catalytic activity of CCZ20 and CT20 in dark and light conditions

As showed in figure 59, CT20 resulted able to adsorb MB in dark conditions. In fact, over the 60% of MB was adsorbed in the first 10 minutes, although apparently released back into the reaction mixture after 15 minutes, as it may be common in adsorption-desorption processes in non-equilibrium conditions. Nevertheless, it is possible that a partially degraded or modified molecule is released, as suggested by the change in the absorption spectra in figure 4a. Conversely, CCZ20 showed a different behaviour, with slight increase in the absorption which was attributed to an experimental artefact (figure 59, 60b). Both CCZ20 and CT20 resulted in MB photodegradation upon UV-vis light exposure, although with different rates (figure 61, 62).

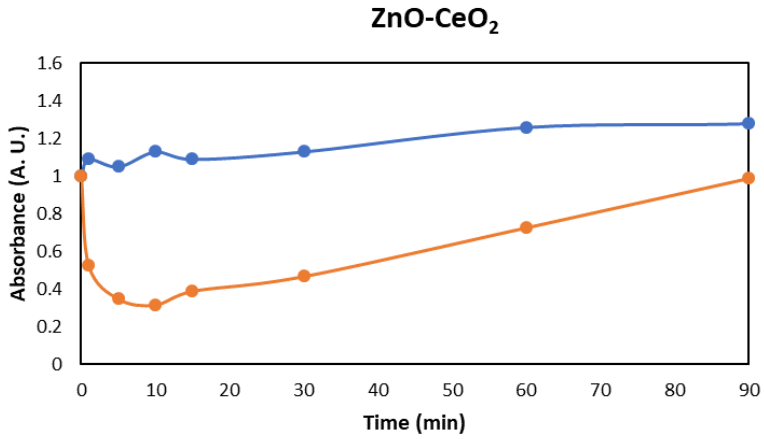

Figure 59 *The MB uptake in presence of CT20 and CCZ20 in dark conditions.*

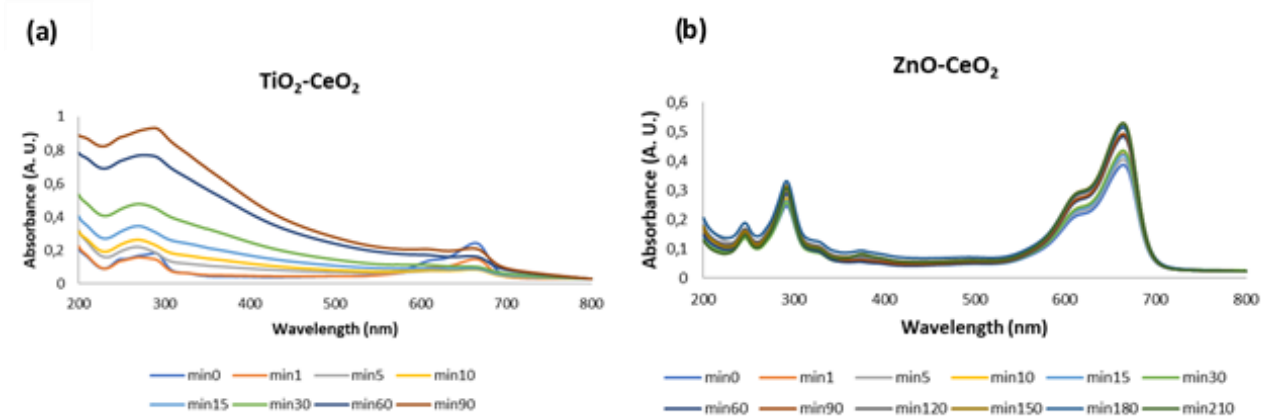

Figure 60 *Time-dependent UV-Vis absorption spectra of MB in presence of (a) CT20 and (b) CCZ20 in dark conditions. In the legend the time intervals are reported.*

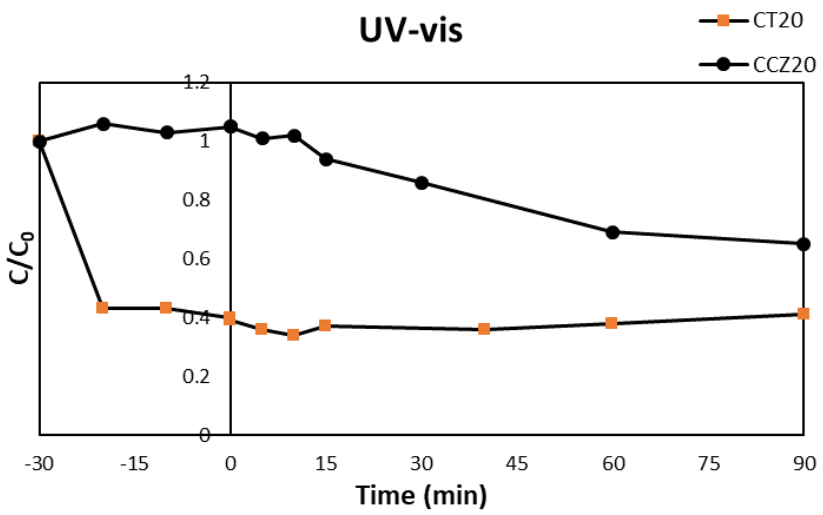

Figure 61 *Time-dependent MB relative concentration in presence of CT20 and CCZ20 upon UV-vis light exposure*

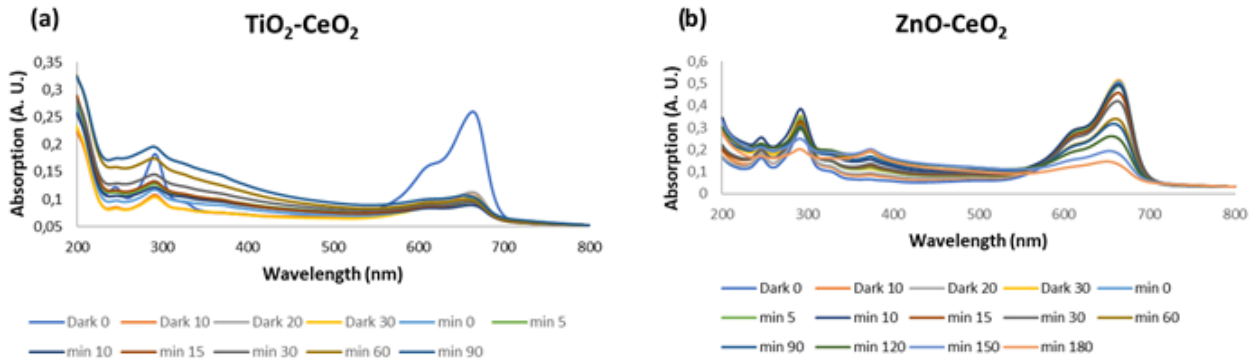

Figure 62 *UV-Vis spectra of MB in presence of (a) CT20 or (b) CCZ20 at different time intervals upon UV-light exposure showing the photocatalytic degradation of MB.*

In order to quantify the amount of detached MB on the catalysts' surface, the latter were washed with NaOH first and then with H_2O, centrifuged and the supernatant was collected and analysed. After 10 minutes treatment, MB was detected only in the CT20 NaOH-based supernatant, but not in the CCZ20 one (figure 63a). Additionally, residual MB was still present, as suggested by the supernatant's absorption analysis after H_2O washing (figure 63b). The spectra of both NaOH and H_2O-based supernatants were compared to the one of MB in 1 M NaOH (figure 63c). After 10 minutes treatment, the MB peak at 664 is blue shifted, suggesting a partial degradation and or coordination of the molecule attributed to NaOH, also responsible for the blue shift in the absorption spectrum of residual molecules recovered from CT20 (figure 63a) when compared to the same residuals, but in H_2O medium (figure 63b). No residual MB was found after the washing procedure of CCZ20.

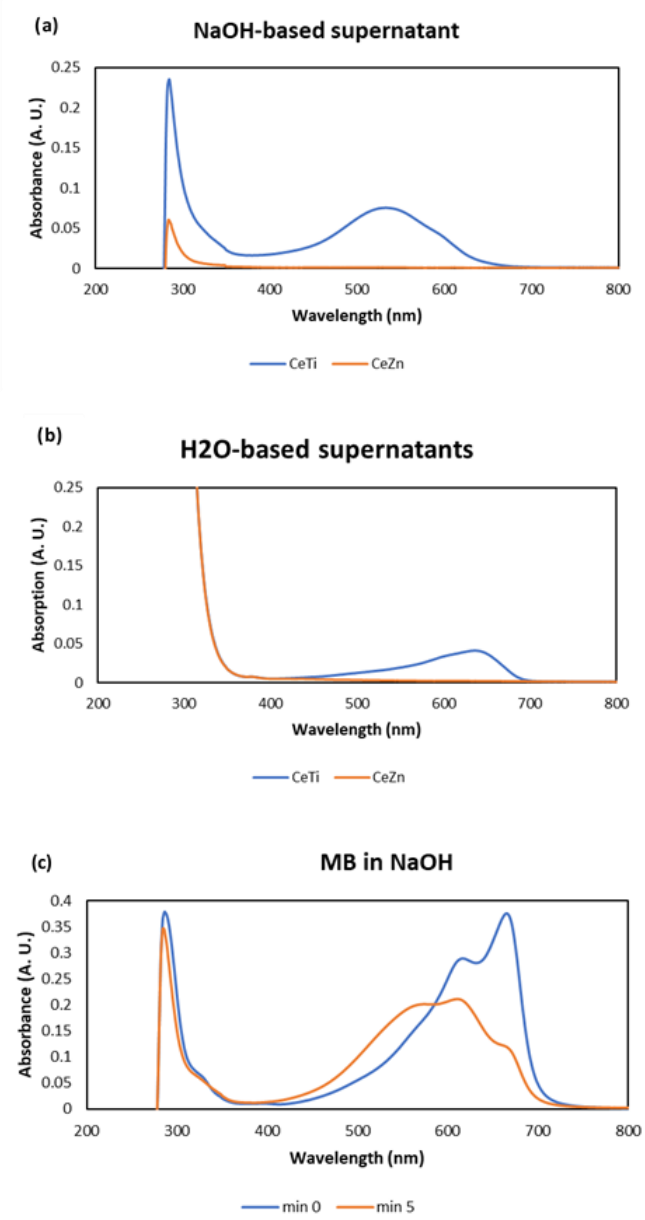

Figure 63 *Absorption spectra of CT20 and CCZ20 supernatants in (a) NaOH and (b) H_2O followed by (c) absorption spectrum of MB at 0 and 10 minutes of NaOH treatment.*

3.2. XRD analysis

Figure 64a shows the XRD pattern obtained for CCZ20, confirming both the presence of ZnO in the wurtzite phase and CeO_2, with the latter in minor quantity as suggested by the broader peaks and by the Rietveld analysis. In general, broad peaks are attributed to either very small size of the crystallites or poor crystallinity. The introduction of Cerium via co-precipitation had already been reported to affect the crystal phase of TiO_2 [19]. Additionally, an amorphous pattern similar to figure 64b, was also reported and attributed to cerium titanate $Ce_xTi_{(1-x)}O_2$ in the TiO_2 phase [25]. Conversely, the XRD analysis of Ce-Zn composites confirmed the presence of both ZnO as wurtzite and CeO_2 as cerianite crystal phase (Figure 64a).

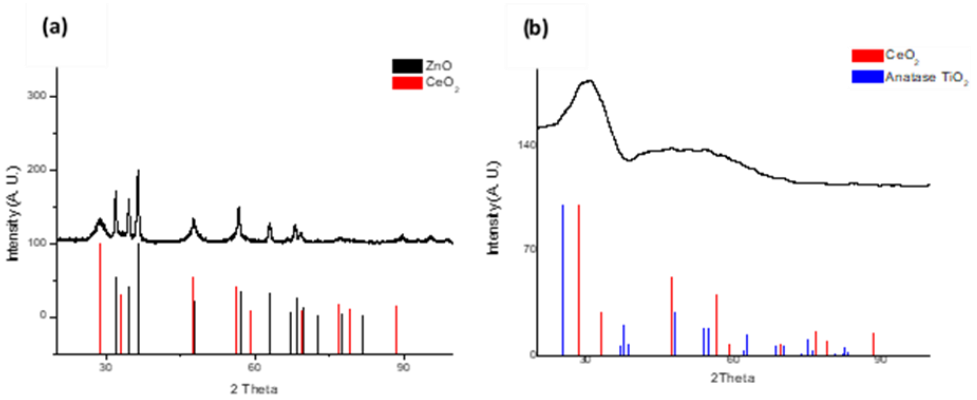

Figure 64 *XRD pattern of (a) CCZ20 and (b) CT20 powder samples. The insets indicate wurtzite and anatase phase, respectively.*

ZnO nanorods showed the characteristic wurtzite phase, in which the higher intensity of the peak at 34.4 (2θ) was attributed to the rod-like shape with preferential crystal growth along the c-axis (002) (figure 65a). TiO_2 nanorods via hydrothermal method resulted in the rutile phase (figure 9b). After the deposition, neither CeO_2 nor TiO_2 was clearly detected, as shown in figure 65c, d.

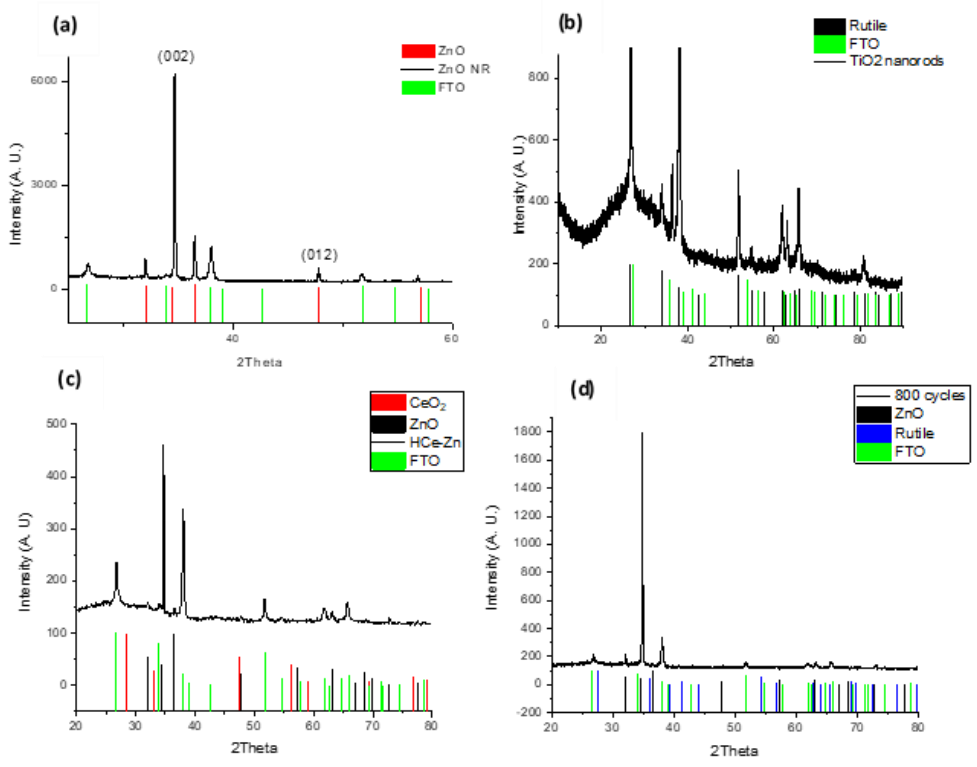

Figure 65 *XRD pattern of (a) ZnO nanorods wurtzite phase, (b) TiO_2 nanorods rutile phase, (c) HCe-Zn and (d) 8TiO_2@ZnO on FTO glass.*

3.3. SEM-EDS analysis

In total, 3 batches of ZnO on FTO glass were synthesised via hydrothermal method, aiming to obtain ZnO nanorods. However, flower-like ZnO structures were obtained in the first batch (B1) (figure 66).

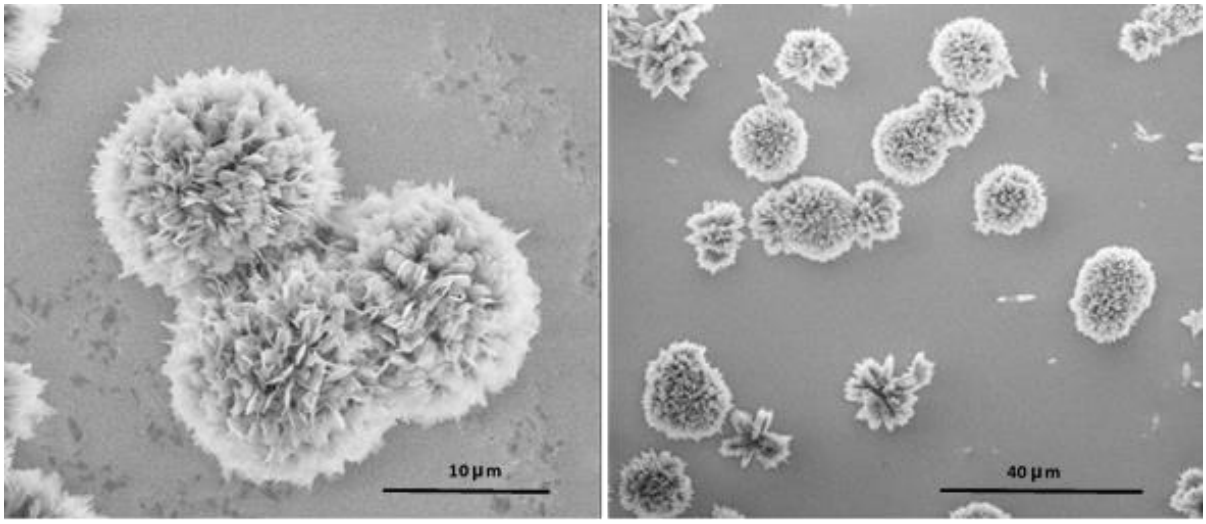

Figure 66 *First batch (B1) of ZnO nanorods via hydrothermal method.*

A possible explanation was a poorly grown seed layer, attributed to the use of a 95% ethanol solution rather than absolute ethanol, with consequent lowered solubility together with the presence of impurities, possibly affecting the growth. Nevertheless, the successful synthesis of ZnO nanorods was achieved in the second (B2) and the third (B3) batches, which resulted in a top average diameter ($\bar{d}$) of 66.02 nm and 73.81 nm respectively (figure 67).

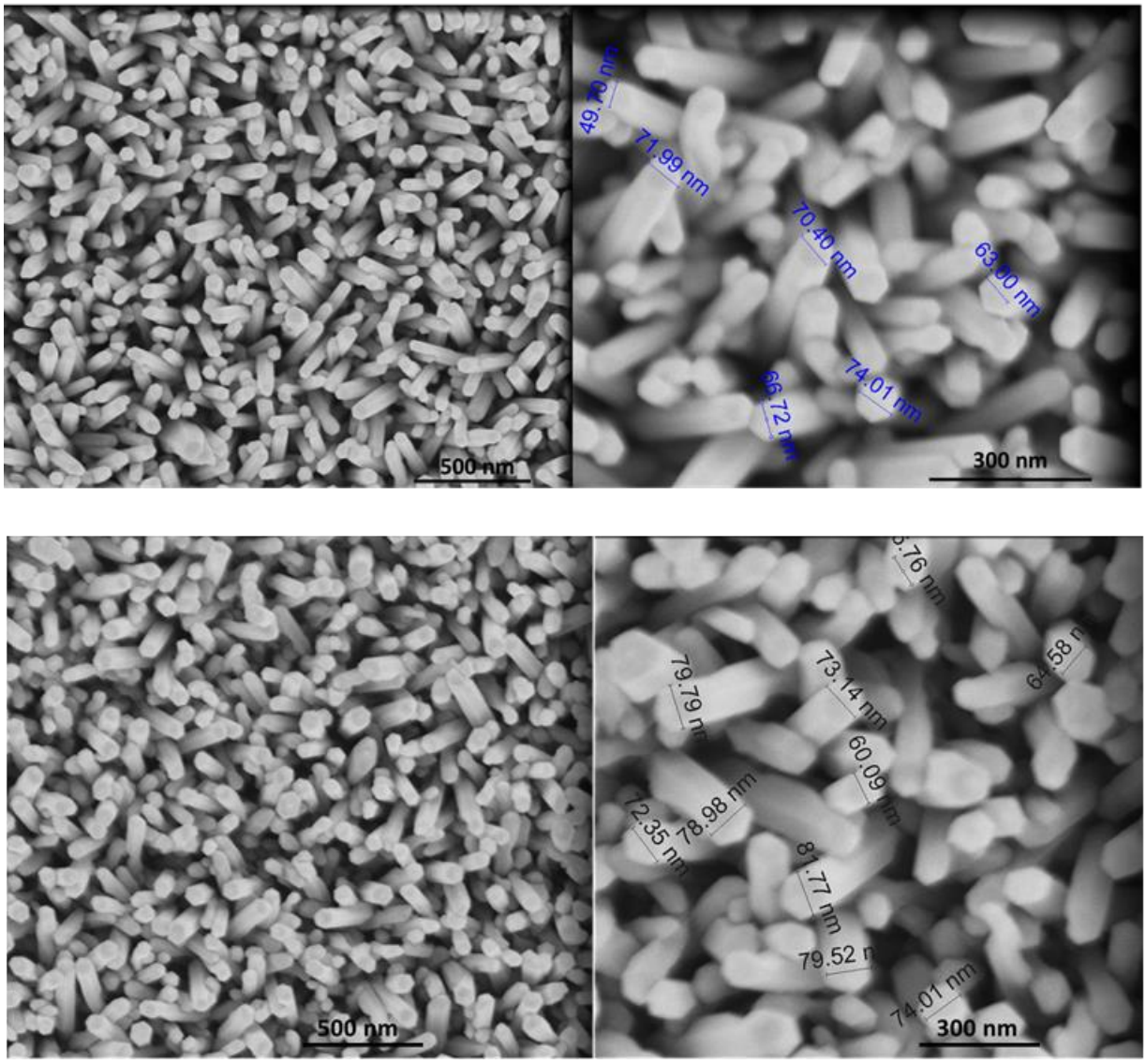

Figure 67 *SEM imaging of the 2nd batch (B2) of ZnO nanorods obtained via hydrothermal method with $\bar{d}$=66.02 nm (top) and of ZnO nanorods from the 3rd batch (B3) obtained via hydrothermal method with $\bar{d}$=73.01 nm (bottom).*

After ALD on ZnO nanorods, the deposited layer was visually detectable by SEM analysis as homogeneous coverage only after 800 cycles (figure 68a-c). The latter resulted in an average diameter of $\bar{d}$=156.74 nm, accounting for a layer thickness of roughly 40 nm. Ti was detected by EDX mapping only for the 200 and 800 cycles (figure 69 a-b), while no detection occurred for the 100-cycle deposition. Figure 14a shows the nano-particles (5-10 nm) detected on top of spin-coated ZnO nanorods belonging to the H batch and detected as Cerium by EDX mapping (figure 70b).

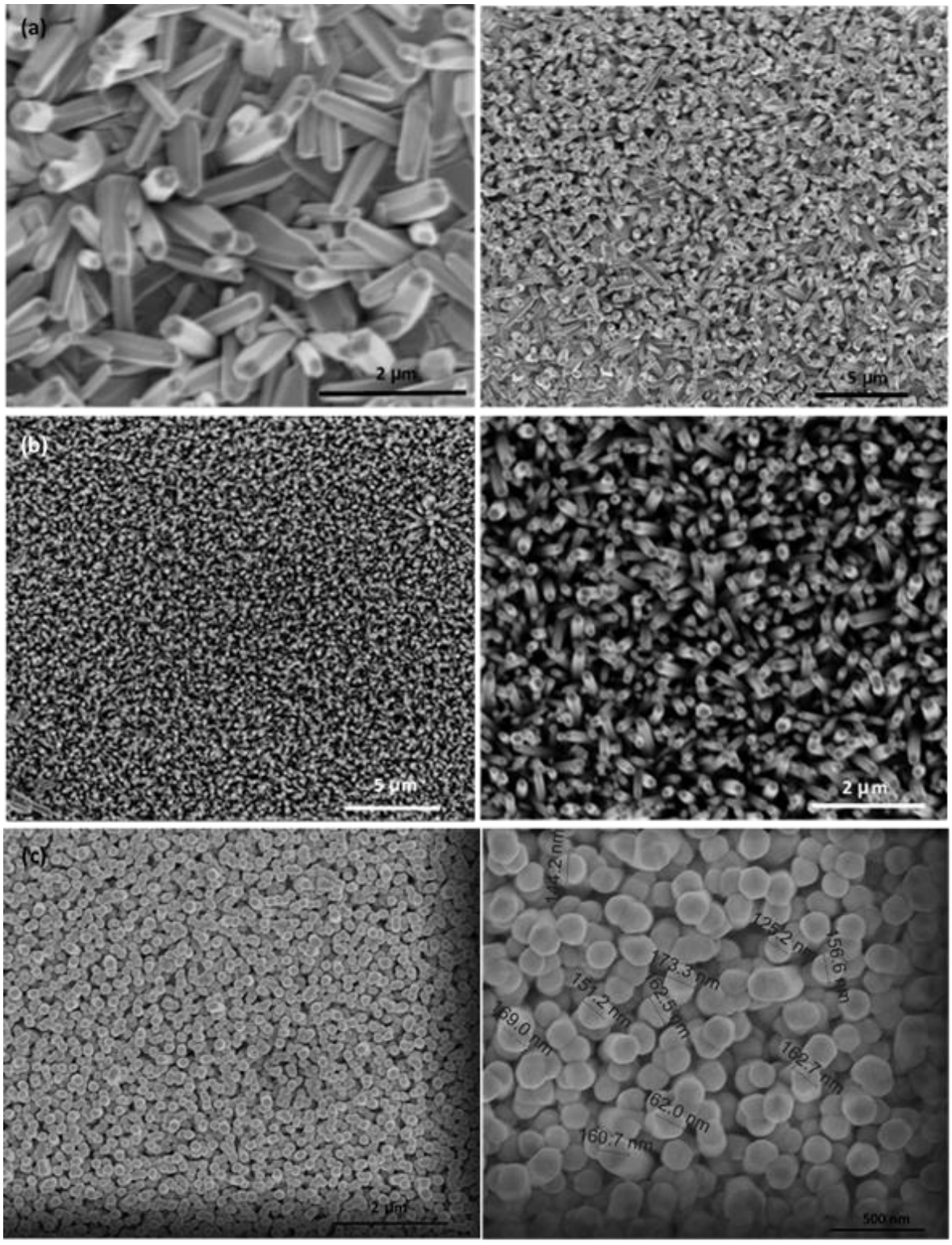

Figure 68 *SEM imaging of ZnO nanorods from after (a) 100, (b) 200 and (c) 800 cycles ($\bar{d}$=156.74 nm) of TiO_2 deposition via ALD*

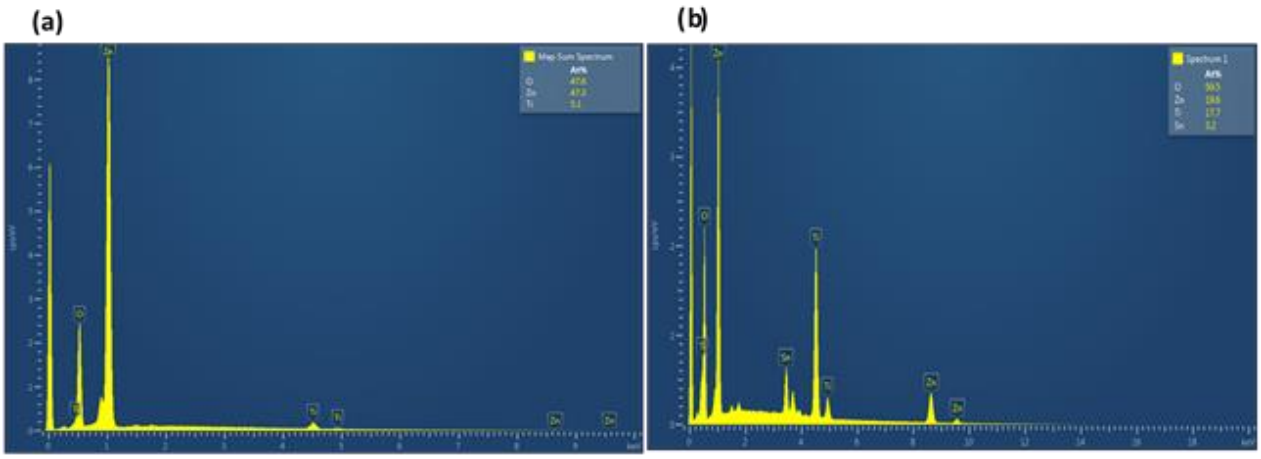

Figure 69 *EDX mapping of ZnO nanorods after (a) 200 cycles and (b) 800 cycles of TiO_2 via ALD*

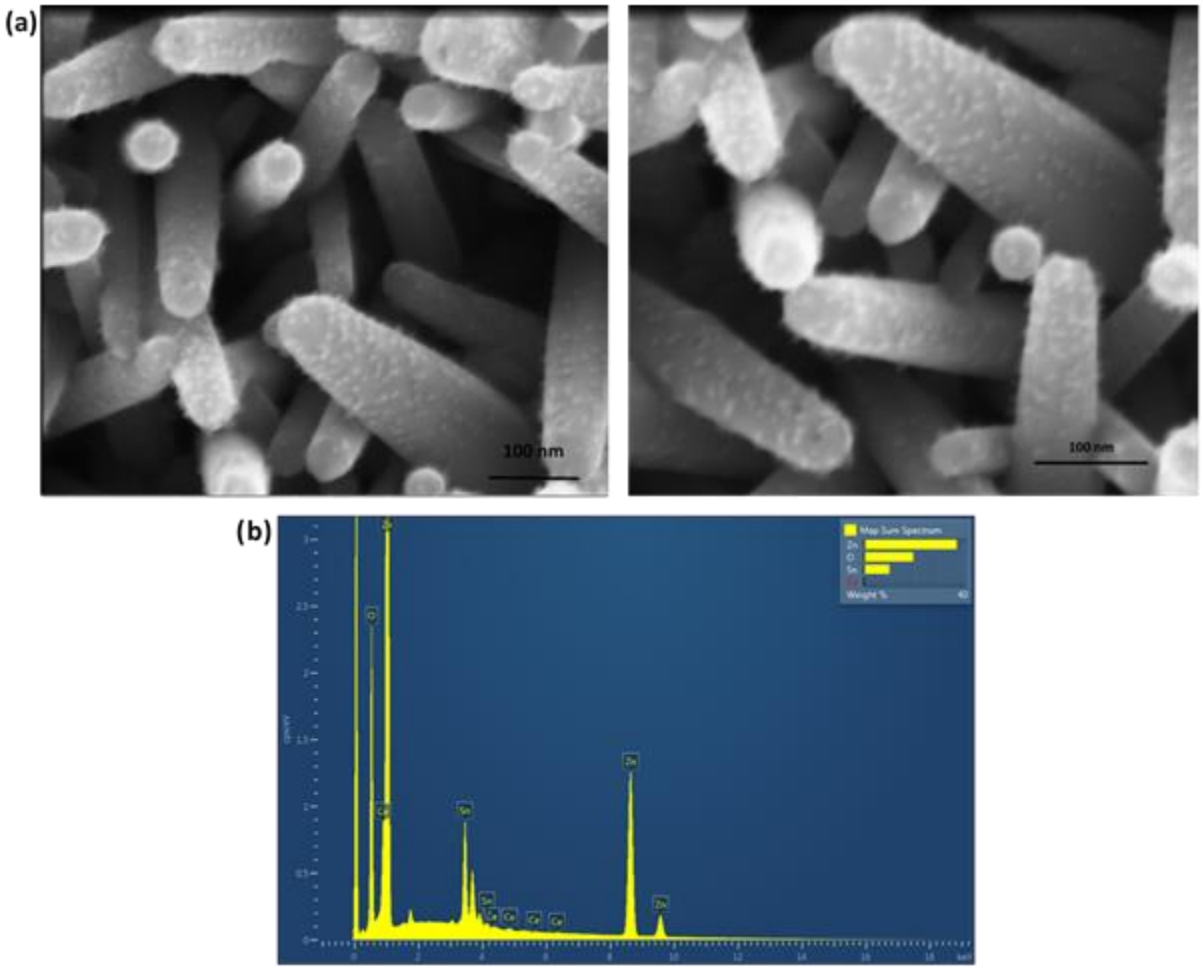

Figure 70 *(a) Cerium nanoparticles on the surface of ZnO nanorods (B3) after spin-coating and (b) Result of the EDX mapping on HCe-Zn. The reason of low Ce detection was attributed to the small size of the nanoparticles.*

TiO_2 nanorods obtained via hydrothermal methods are shown in figure 71a. Similarly, Cerium nanoparticles were detected on the H batch of the nanorods (figure 71b) after the spin-coating procedure.

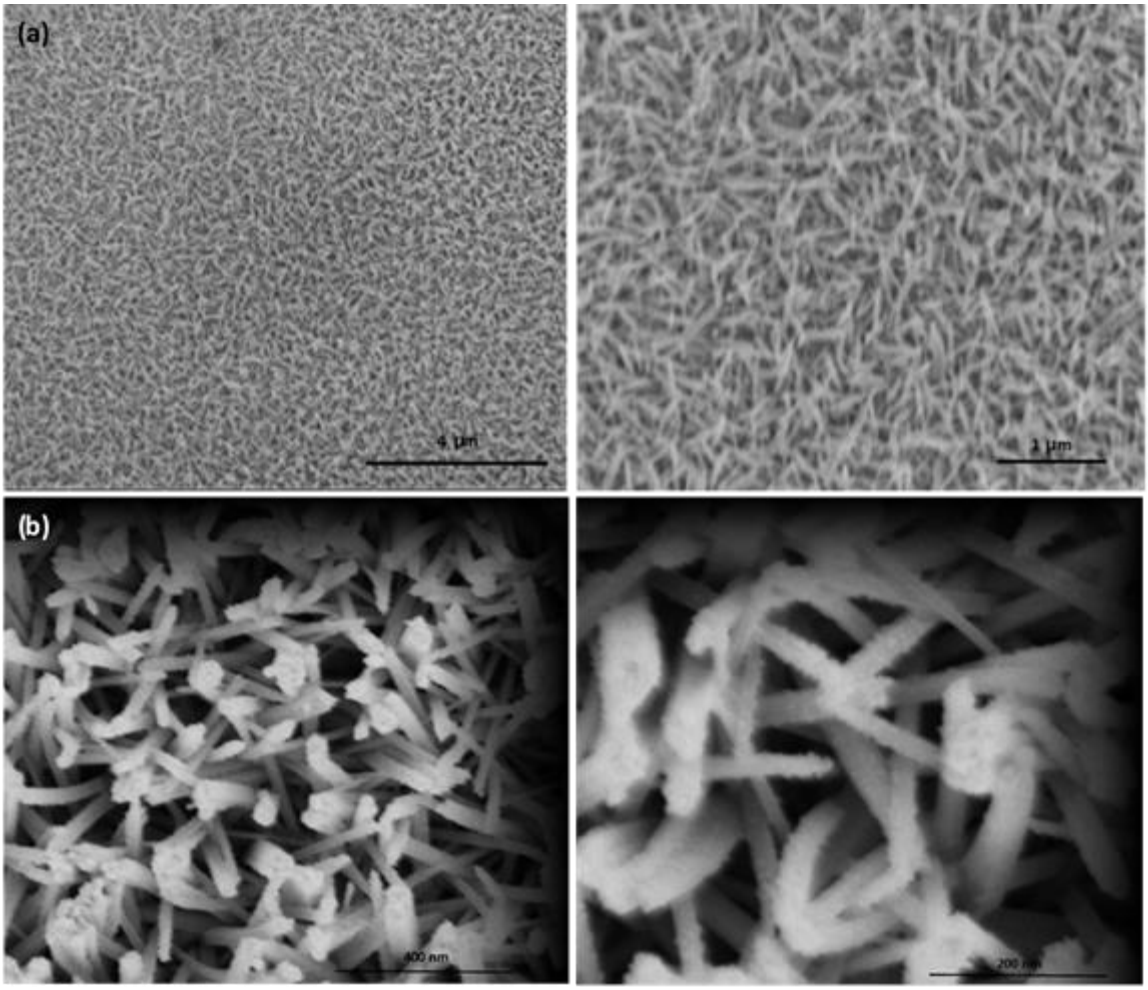

Figure 71 *(a) Rutile phase TiO_2 nanorods obtained with hydrothermal method, $\bar{d}$=39.89 nm and (b) cerium nanoparticles on top of TiO_2 nanorods after spin-coating and heat treatment at 450 °C for 2h.*

3.4. TEM-EDS analysis

TEM analysis performed on cerium-coated ZnO and TiO_2 are shown in figure 72 and 73. Nanoaggregates of 5-20 nm-sized were detected in HCe-Ti and HCe-Zn samples (figure 72c, d), while no aggregates were present on top of LCe-Ti and LCe-Zn (figure 16a, b). High resolution TEM analysis showed the wurtzite and rutile phase for ZnO and TiO_2 NR respectively (figure 73a, b) with the typical crystal phase of CeO_2 and Ce_2O_3 for the aggregates (figure 73c, d) but absent for both LCe-Ti and LCe-Zn (figure 73a, b). In fact, the presence of cerium was confirmed by SEM-EDS analysis for HCe-Ti and HCe-Zn respectively (figure 74), while no detection occurred for LCe-Ti and LCe-Zn samples.

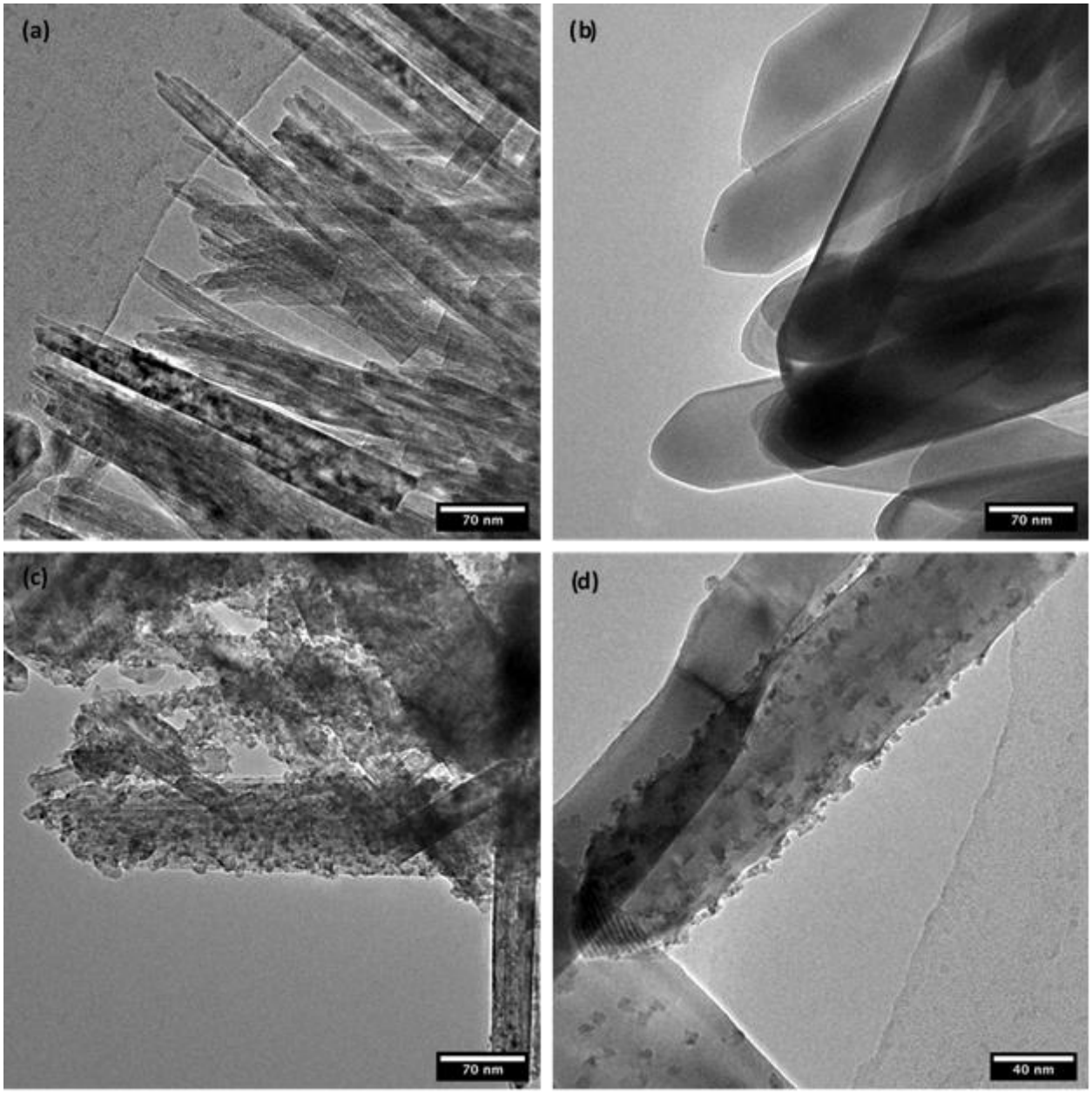

Figure 72 *TEM analysis of (a) LCe-Ti, (b) LCe-Zn, (c) HCe-Ti and (d) HCe-Zn showing the presence of nanoaggregates in c and d.*

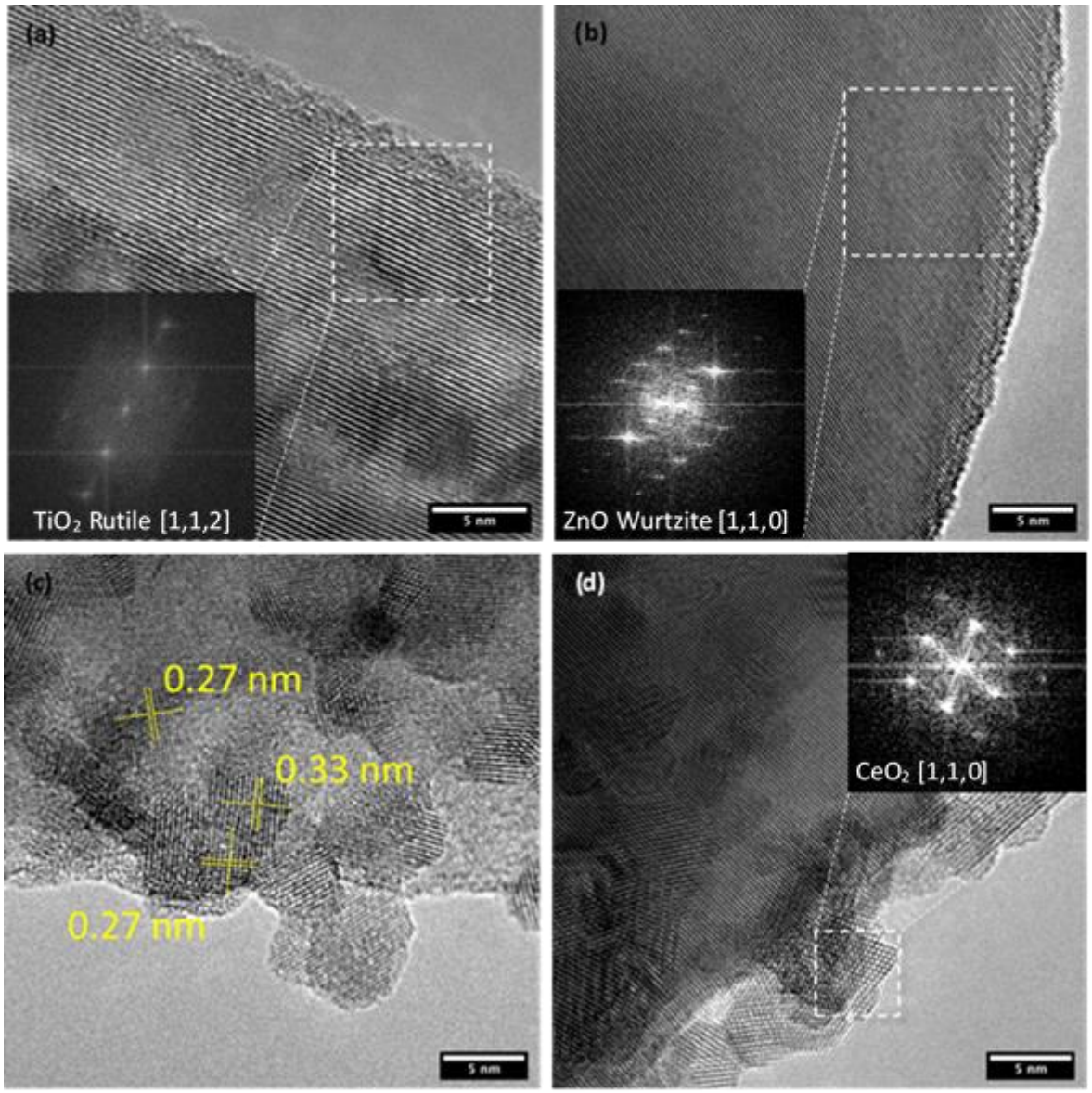

Figure 73 *High resolution TEM analysis showing the crystal planes of (a) Rutile LCe-Ti, (b) Wurtzite LCe-Zn, (d) Cerianite in HCe-Zn and (c) the dimension of monocrystalline CeO_2 nanoparticles in HCe-Ti.*

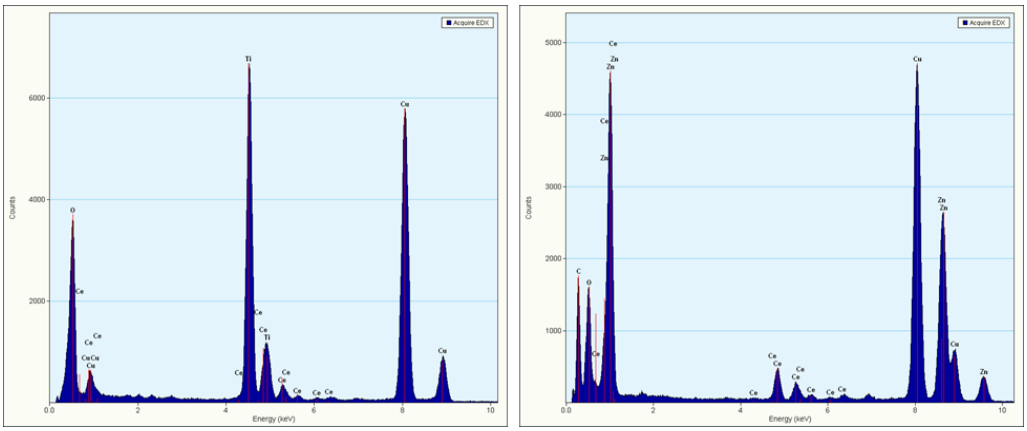

Figure 74 *TEM-EDS analysis of (left) HCe-Ti and (right) HCe-Zn.*

3.5. RBS analysis

RBS analysis on ALD-deposited Ti revealed that the deposition did not occur linearly, when the number of cycles was low (figure 75).

As shown in figure 76, RBS analysis assessed the thickness of TiO_2 films deposited on a silicon substrate with ALD, as shape-related scattering may mislead the interpretation. After 50, 100, 200 and 800 cycles the measured thickness was 0.8, 1, 1.7 and 45 nm respectively (figure 76), the latter confirming what also estimated by SEM imaging (see section 3.4).

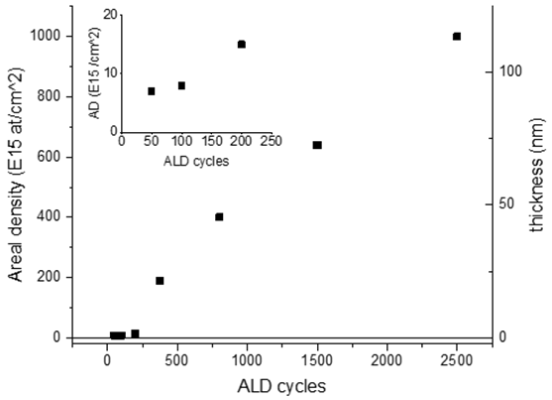

Figure 75 *RBS results vs number of cycles. The deposition becomes linear with high number of cycles.*

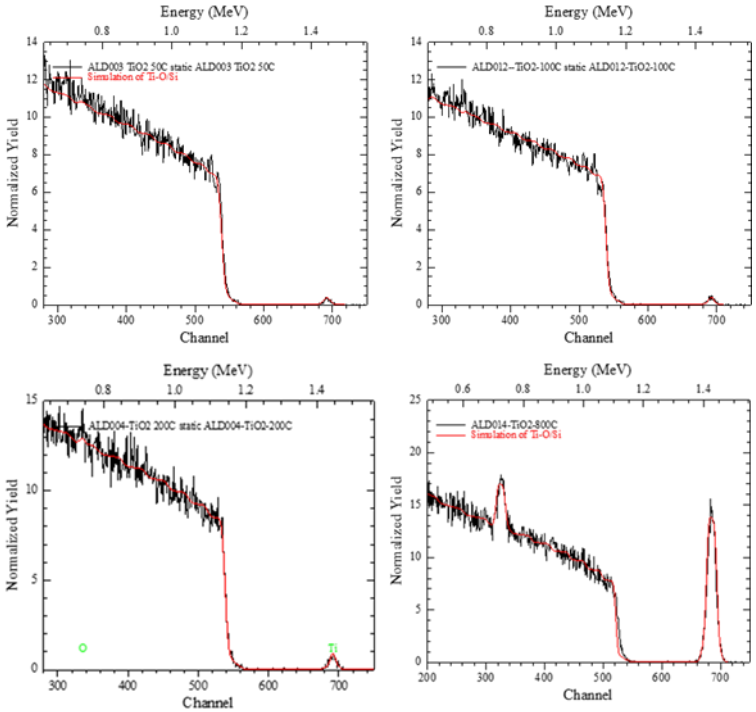

Figure 76 *RBS analysis results of ALD deposition on Silicon substrate after 50, 100, 200 and 800 cycles.*

3.6. PL and time-resolved PL analysis

The broad emission in the visible range (figure 78a) was related to the high number of defects in the material. ZnO visible emission has been extensively studied and generally related to crystal defects, whose type, number and distribution have been proposed to be affected by both the synthetic method and the post-synthetic treatment, such as annealing temperature and environment [26-28].

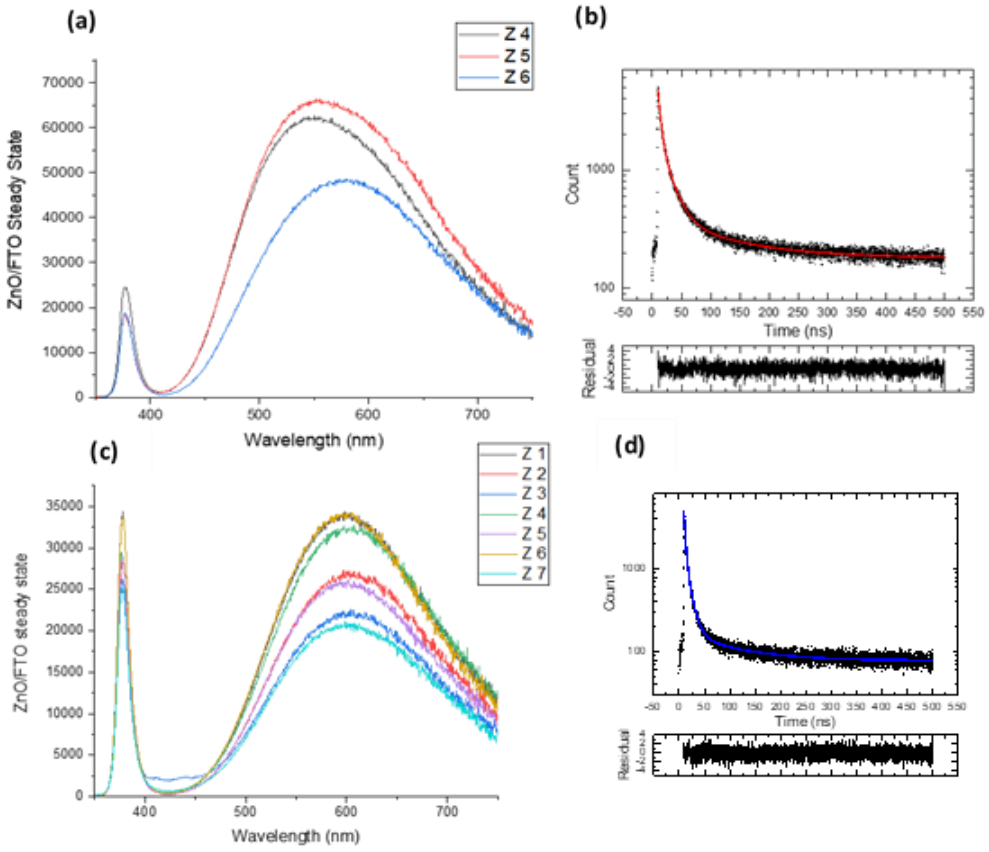

Figure 77 *PL analysis of ZnO nanorods with (a) the steady state and (b) the life-time of visible emission (550 nm) decay of the B2; (c) the steady state and (d) the life-time of visible emission (600 nm) decay of B3, upon LED excitation (371.8 nm).*

As shown in all PL measurements (figure 78-81), the visible emission is present as a broad peak, which is attributed to different type, distribution and percentage of crystal defects. In fact, it is possible that both multiple peaks and defects complexes account for the final emission [29]. Notably, the batches 2 and 3 resulted in different visible emission wavelength, yellow for B2 (550 nm) and orange-red for B3 (600 nm) (figure 78a, c), which also resulted to be different in intensity before and after annealing in air at 450 °C (figure 79a, c).

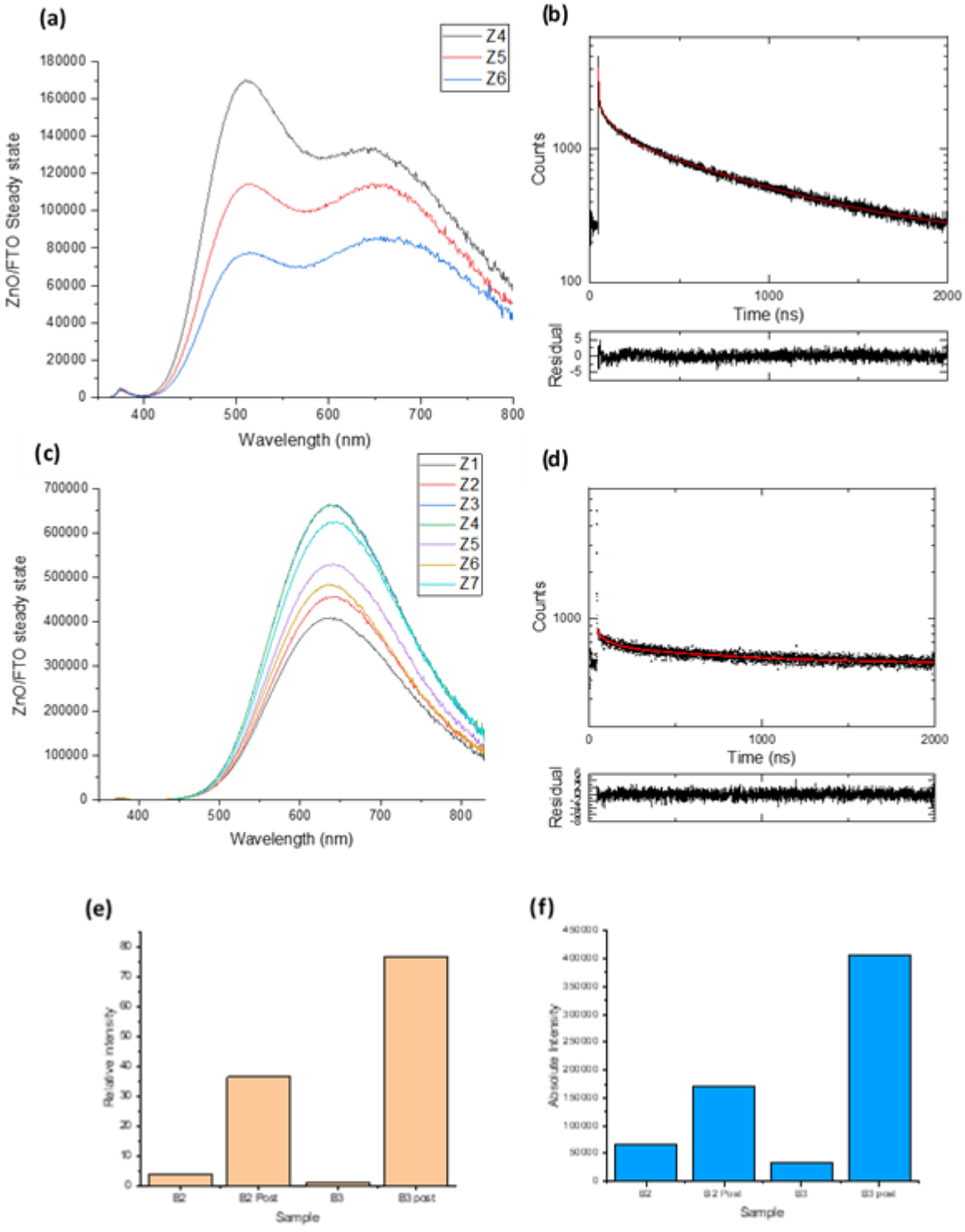

Figure 78 *PL of (a) B2 ZnO nanorods with (b) life-time of the visible emission (510 nm), (c) PL and (d) and life-time of the visible emission (640 nm) of B3 ZnO nanorods after annealing at 450 °C for 2 h, after a 371.8 nm laser excitation. In the bottom (e) relative intensity of the visible to UV emission and (f) absolute intensity of the visible emission before and after annealing at 450 °C of B2 and B3.*

The yellow to orange-red shift in the as prepared ZnO (figure 78a, c) is likely to occur in virtue of a slightly different ratio between oxygen vacancies (V_O), oxygen interstitial (O_i), zinc vacancies (V_{Zn}) and zinc interstitial (Zn_i), both as individual or combined emitters. In general, the orange-red emission

has been related to excess oxygen while the green emission was mainly attributed to V_O (2.3 eV), oxygen anti-sites (O_{Zn}) (2.38 eV) and V_{Zn}, whose emission is more controversial as also identified as blue emission (3.06 eV) [26]. The yellow emission is instead commonly attributed to O_i (2.28 eV) or even to the surface hydroxyl groups in Zn(OH), the latter groups proposed to desorb after a 150 °C treatment [26]. In presence of Zn_i, the V_O-Zn_i and O_i-Zn_i complexes were also proposed play a role in the yellow-orange emission [26]. After annealing at 450 °C the samples of B3 and B4, two different behaviours were observed (Figure 79a, c). B2 showed two main maxima at 510 and 646 nm (figure 23a) while B3 had only one maximum at 640 nm (figure 79c), also enforcing the hypothesis of a different defects content. In general, increasing the annealing temperature lead to a decrease or to a red shift of the defect emission, as well established in the literature. While the defects decreased or blue shifted in inert gas by increasing the annealing temperature, a red-like emission appears after annealing in an air-rich environment [26-28]. Moreover, oxygen levels modulation in the growth environment was positively related to the presence of defects responsible of the yellow-orange emission in as-prepared ZnO nanorods, which were absent when the growth occurred in vacuum conditions [26]. Therefore, the population of oxygen-related defects are likely to play a major role in both the UV and the visible emission of nanostructured ZnO. Notably, the UV emission was considerably decreased after annealing (figures 79e, f) and the higher visible intensity would suggest an increased radiative decay in defect-related states.

Therefore, it is proposed that a higher ratio of V_{Zn}/ V_O defects may account for the blue shifted emission of samples belonging to the B2 (figure 78a) if compared to the ones of B3 (figure 78b). The higher presence of V_{Zn} might then explain the increased green emission at 510 nm after annealing in air, possibly related to anti-site oxygen filling the vacancies (figure 23c) and lowering the presence of O_i by rather marking the red emission. Conversely, a lower V_{Zn}/ V_O ratio would lead to faster V_O depletion and higher content of O_i and surface oxygen. Notably, figure 80a and 81a suggest that defects responsible of the orange-red emission would be mainly surface related, as visibly affected by both the TiO_2 surface layer coating and the presence of CeO_2 nanoparticles.

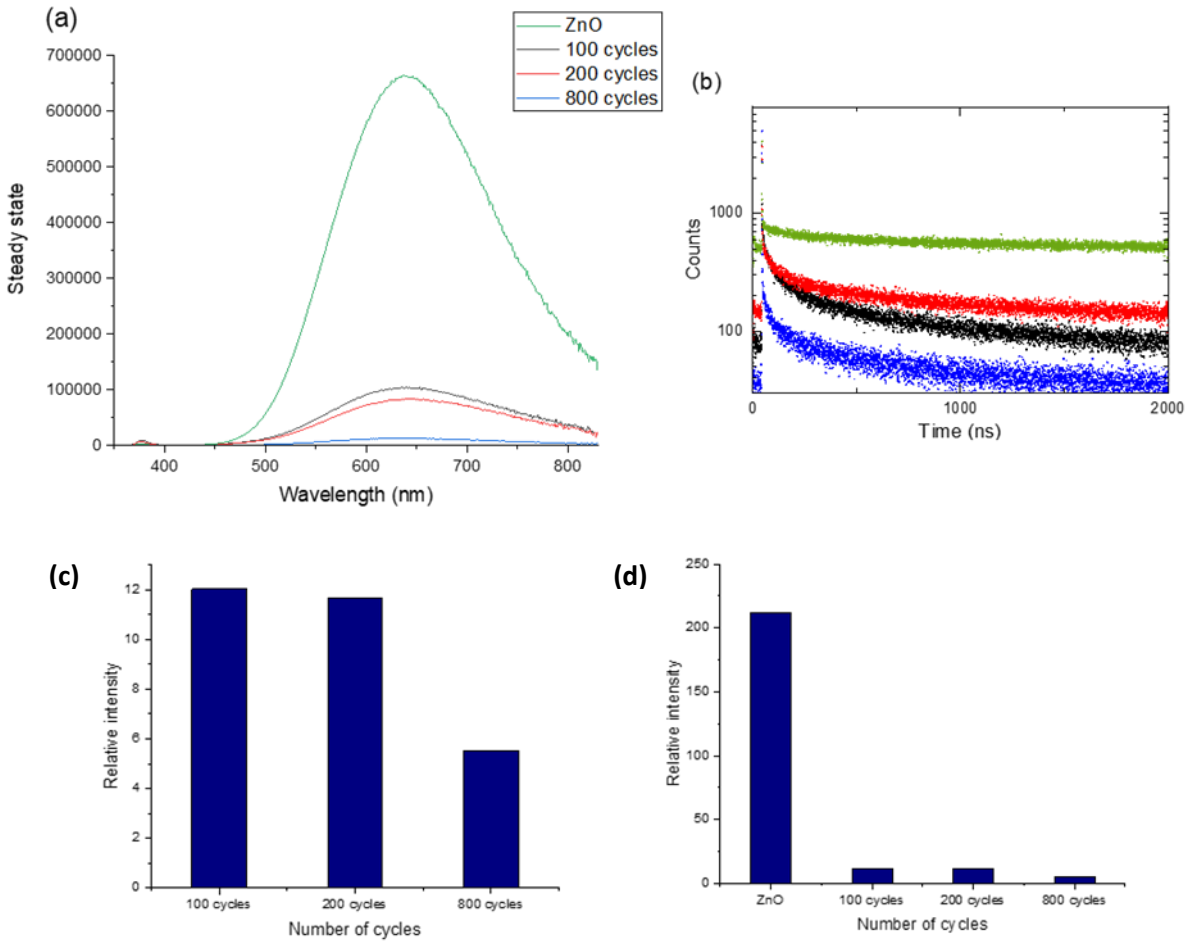

Figure 79 *(a) PL and (b) life-time comparison of control ZnO NR and ALD deposited with different number of cycles. The life-time of the visible emission (640 nm) was measured upon 371.8 nm laser excitation. (c, d) Change in relative intensity of the visible to UV emission with thickness of ALD-deposited layer.*

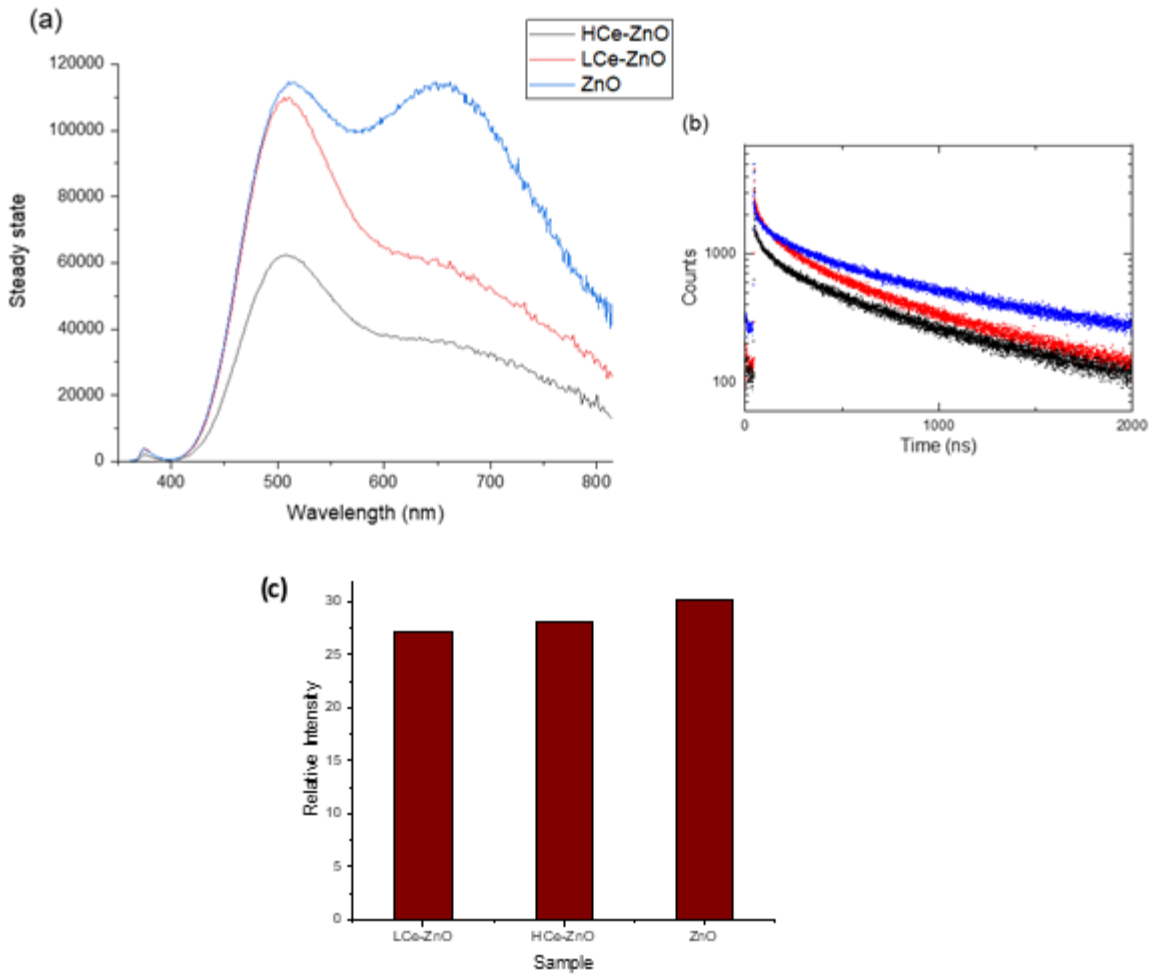

Figure 80 *(a) PL and (b) life-time comparison of control ZnO NR and Ce spin-coated in either the H or the L ZnO NR batches. Life-time of the visible emission (510 nm) was measured upon 371.8 nm laser excitation. (c) Effect of cerium spin-coating deposition on the relative Intensity of the visible to UV emission.*

Table 2 shows the time constants τ_{1-3} obtained by fitting life-time measurements, which resulted in a tri-exponential decay, and the relative percentage (Rel%) as indication of the photon population distribution belonging to a certain decay. The χ^2 value has been considered as measure of reliability when approaching one.

Before annealing (figure 78a and c), the yellow-emitting ZnO NR (B2) showed almost doubled time constants τ_{1-3} with respect to the red-emitting batch (B3) (table 2). This difference would support the different nature of the defects involved in the visible emission. After the annealing, the appearance of a red-emission with consequent variation of the emission pattern in both samples (figure 79), was likely related to the long-radiative event dominating the decay, and possibly attributed to V_O occupancy which would support the remarkable increase in the visible emission (figure 79e and f).

As shown in table 2 and suggested by figure 81b the time decay was shortened in both HCeZn and LCeZn compared to ZnO NR, a feature that coupled to the decreased visible emission (figure 81c),

suggested an interference with the radiative recombination via possible CeO_2-ZnO charge exchange. Similarly, the presence of a TiO_2 layer also affected the visible emission, which decreased with a direct but non-linear proportionality to the layer thickness (figure 80c and d). This result was likely attributed to the effect of a physical shielding of the luminescence by TiO_2-based layers. Notably, the lower values of the time constants of $1TiO_2$@ZnO, $2TiO_2$@ZnO and $8TiO_2$@ZnO when compared to bare ZnO NR, and the consequent shortened decay (figure 80b) supported the possible presence an electron exchange between ZnO and TiO_2, which could explain the decreased visible emission as an increase of non-radiative events, also owed to the presence of a indirect band gap semiconductor such as TiO_2.

Table 6 *Life-time parameters and relative percentages of time-resolved PL*

Sample		X^2	τ_1*(ns)*	*1Rel%*	τ_2*(ns)*	*2Rel%*	τ_3*(ns)*	*3Rel%*
As prepared ZnO NR	***B2***	-	4.31	16.46	18.96	47.27	117.30	36.27
	B3	-	2.55	25.79	9.92	47.41	95.79	26.80
Post-annealing ZnO NR	***B2***	1.140	0.82	0.32	75.55	6.95	738.43	93.09
	B3	1.064	0.43	1.61	72.71	6.58	837.06	91.81
HCe-ZnO		1.068	0.75	0.41	79.16	8.44	653.99	91.14
LCe-ZnO		1.067	13.65	1.44	129.75	14.47	711.97	84.09
$1TiO_2$@ZnO		1.111	0.53	2.52	47.14	16.44	523.20	81.04
$2TiO_2$@ZnO		1.086	0.38	3.03	47.03	11.79	581.34	85.18
$8TiO_2$@ZnO		1.042	0.41	8.15	39.40	12.78	537.60	79.07

3.7. Photoelectrochemical test

3.7.1.Linear sweep voltammetry

The current density produced by different samples was compared and measured in both dark and light conditions. As expected, and as shown in figure 82b the current produced under light illumination is higher than the one obtained in dark conditions (figure 82a). In dark conditions, the best current was produced by LCeZn as 1.65 μA/cm^2 at the potential of 1.70 V (vs RHE).

Furthermore, in presence of light, the best performance was detected for LceZn, with a current density of 55.11 and 91.32 μA/cm^2 at the potential of 0.8 and 1.70 V (vs RHE) respectively, followed by ZnO, LceTi, HceTi, $2TiO_2$@ZnO, TiO_2 NR, HceZn, $1TiO_2$@ZnO and $8TiO_2$@ZnO. It is suggested that

the increase of current due to higher photogenerated electron flow to the photocathode would improve the oxidising abilities of the photoanode, in virtue of the increased presence of holes. Notably, the presence of CeO_2 improved the photocurrent in all Ti-based electrodes, while only addition of low amounts of CeO_2 had a similar effect on ZnO nanorods (figure 82b).

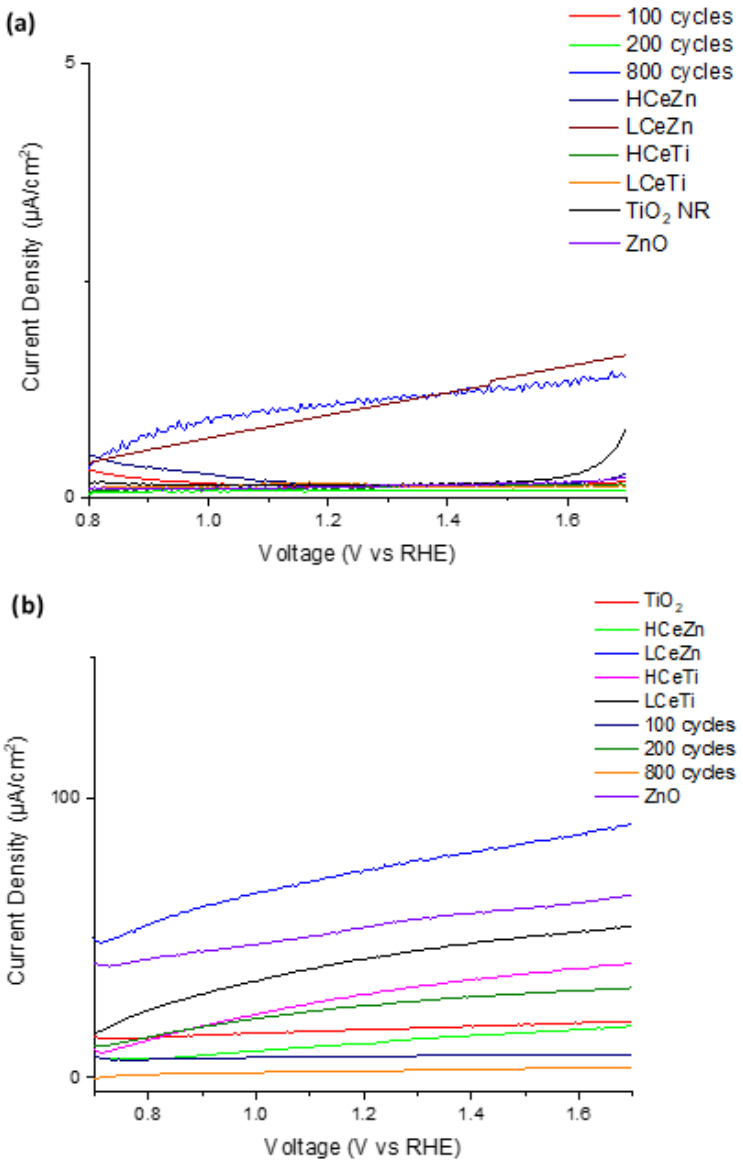

Figure 81 *LSV comparison (a) in dark conditions or (b) after UV-visible light exposure, with a scan rate of 10 mV/s.*

3.7.2. Chrono-amperometry

All the tested materials showed a fast light-to-dark response and all currents were higher in presence of an applied bias of 0.8 V vs SCE with respect to the counterparts without any applied potential (figure 83-85). The effect of 1 nm and 40 nm TiO_2 deposition on ZnO NR was beneficial for the stability of the material, despite being detrimental for the current flow in the sample with a thicker TiO_2 layer

(figure 84a-d). Notably, the presence of CeO_2 nanoparticles in HCeZn (figure 83e) seemed not to protect ZnO NR from photo-corrosion in presence of an applied potential, although the photo-protection was achieved when no potential was applied, which also resulted in a progressive increase in the photocurrent. A similar, but more attenuated behaviour was detected for LCeZn (figure 28f) which however also showed an increased current with respect to bare ZnO NR both with and without applied bias. It is suggested that a more homogeneous cerium oxide coverage in LCe-Zn would account for a better photoprotection and a higher current. The presence of CeO_2 also increased the current response in TiO_2 NR, although the photo- and the electro-stability seemed to remain unvaried (figure 84a and c). Comparison of the synthesized samples (figure 85a and b) showed that the highest current was obtained by LCeZn either with or without bias applied.

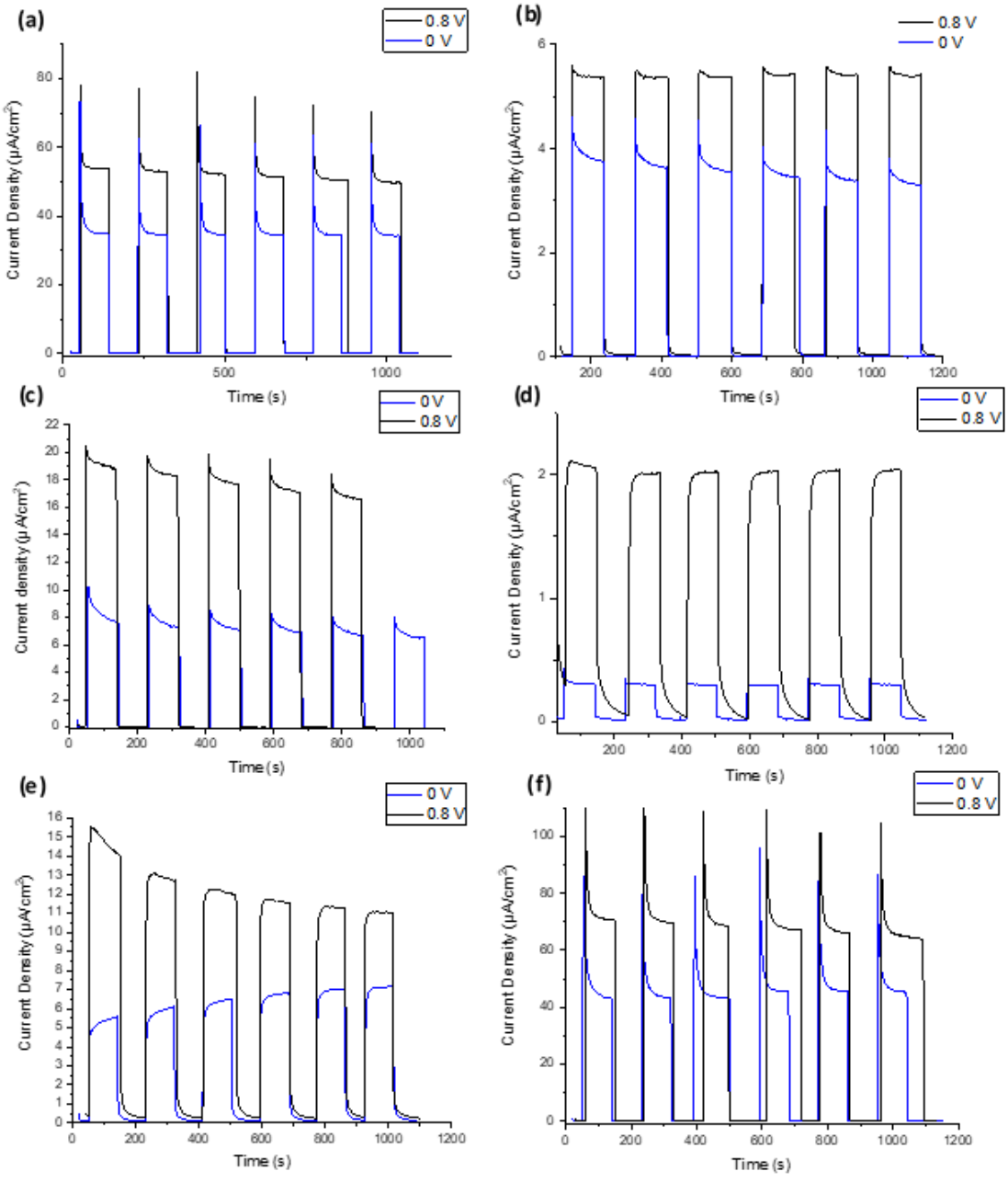

Figure 82 *Transient photocurrent experiment with and without applied bias of (a) ZnO NR, (b) 1TiO_2@ZnO, (c) 2TiO_2@ZnO, (d) 8TiO_2@ZnO, (e) HCe-Zn and (f) LCe-Zn. The bias applied was 0.8 V vs SCE.*

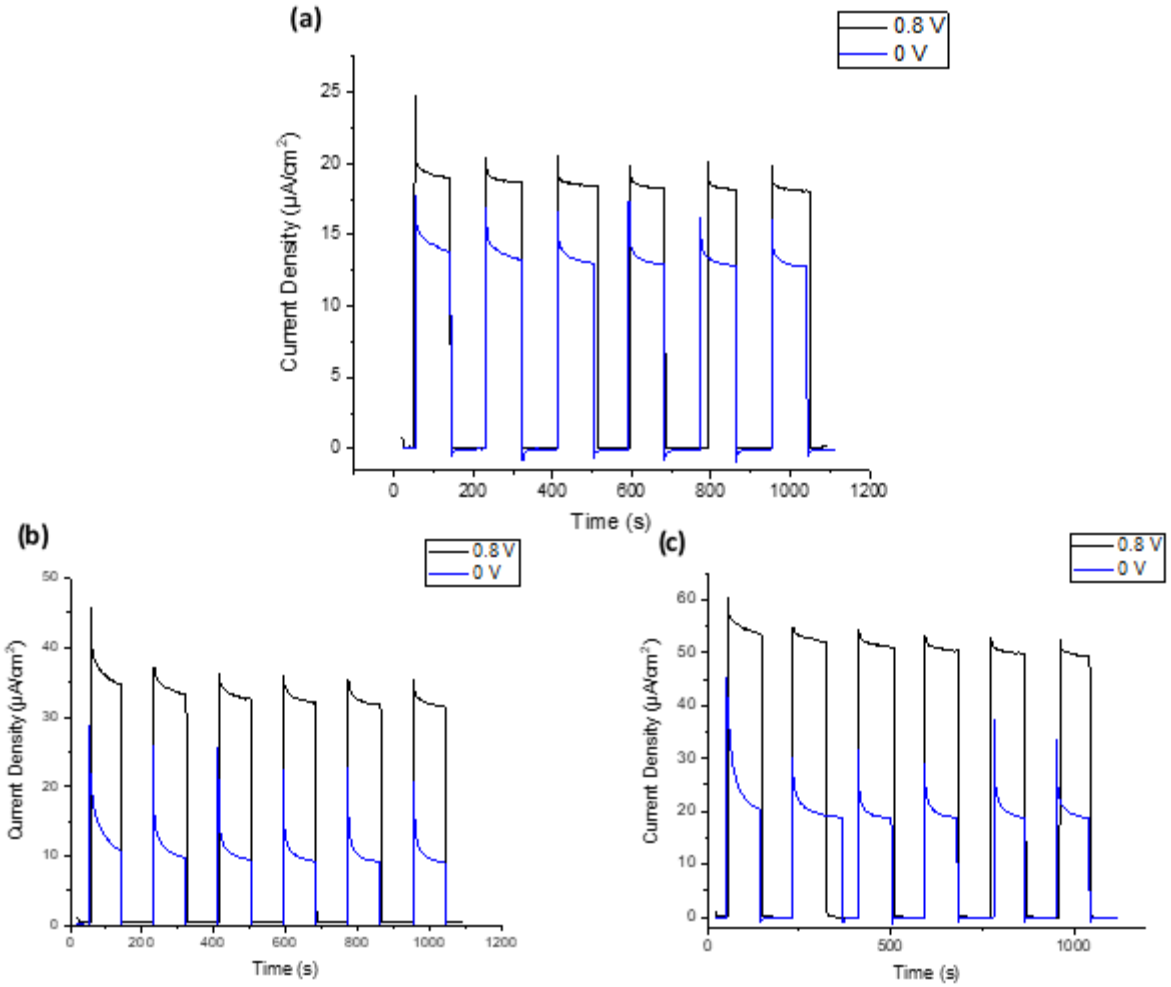

Figure 83 *Transient photocurrent with and without applied bias of (a) TiO_2 NR, (b) HCe-Ti and (c) LCe-Ti. The bias applied was 0.8 V vs SCE.*

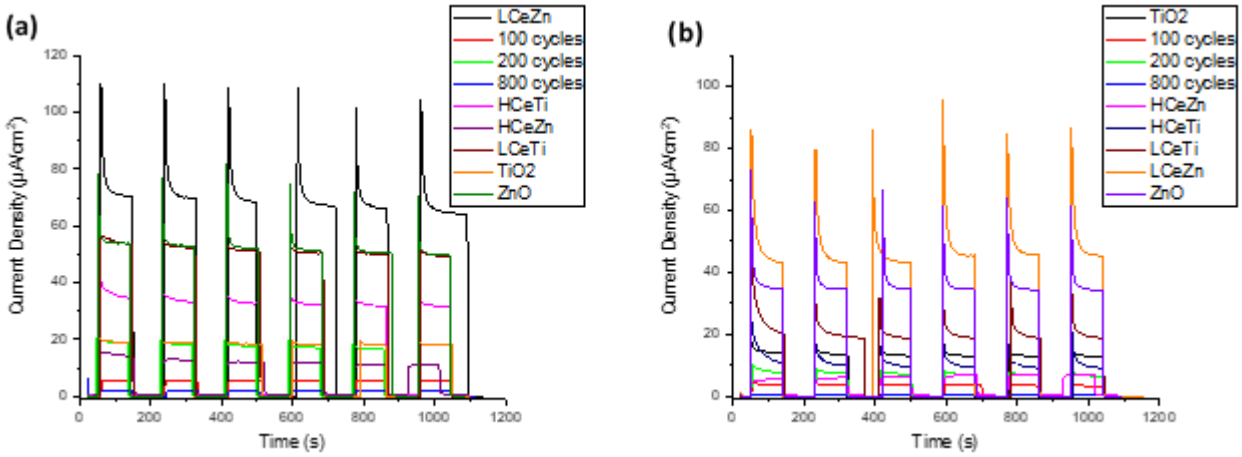

Figure 84 *Transient photocurrent comparison with (right) and without (left) an applied bias of 0.8 V vs*

3.7.3. Electrochemical impedance spectroscopy

The impedance was measured under UV-vis illumination at a potential of ~0.8 V (vs RHE) at which in general the R_p is mainly related to the charge-transfer process [30]. For this reason and for the absence of double circles in the Nyquist plot, a Q-R equivalent circuit has been chosen to fit the experimental data (figure 86). However, HCe-Ti, HCe-Zn, LCe-Ti and TiO_2 were not adequately fitted by the Q-R model and resulted in a significant error, possibly suggesting the requirement of a different equivalent circuit or of the addition of circuit elements [30, 31].

The resistance attributed to the interface charge exchange (R_2) resulted modified by the presence of a coating layer. An increase of the layer thikness of ALD-grown TiO_2 resulted also in an increase in the resistance, when compared to bare ZnO NR (Table 3). Nevertheless, the calculated capacitance C_{DL}^{α} resulted increased only in $8TiO_2$@ZnO, suggesting the possible presence of recombining events within TiO_2 thin layers of $1TiO_2$@ZnO and $2TiO_2$@ZnO, as supported by PL analysis (section 3.6), both localized at the solid-liquid interface and at the level of the SC-SC junction, thereby favouring a thin depletion layer and a consequent lowered surface-related charge accumulation [32]. Conversely, the increase of the C_{DL}^{α} in presence of a thicker layer in $8TiO_2$@ZnO, was proposed depend on the increased width of the depletion layer, also attributed to a possible decrease in the charge mobility owed to the non-crystalline phase of the TiO_2 layer, and which explained the remarkably increased resistance. In this regard, the photo-current response of $8TiO_2$@ZnO NR measured both by LSV and by the transient photo-current experiment (section 2.7 and 2.8) was the lowest current, supporting the aforementioned mechanism. The presence of CeO_2 decreased the resistance R_2 from 1750.8 Ω/cm^2 in ZnO NR to 1220.6 and 1010.2 Ω/cm^2 in LCe-Zn and HCe-Zn respectively. Moreover, the C_{DL}^{α} was also decreased, validating the CeO_2-ZnO electron exchange suggested by the PL experiment (section 3.6) and likely responsible of the decrease of the depletion layer thickness, a lower interfacial charge accumulation and a more efficient solid-liquid charge exchange. However, the presence of CeO_2 NP, rather than a homogeneous layer as in $1TiO_2$@ZnO, $2TiO_2$@ZnO and $8TiO_2$@ZnO, was identified as one the possible reason for the different capacitance between TiO_2- and CeO_2-loaded ZnO based materials (table 3). Eventually, it is reminded that the not particularly adequate fitting procedure for TiO_2-based materials, may have led to misleading results, as suggested by table 3, which were therefore not further discussed.

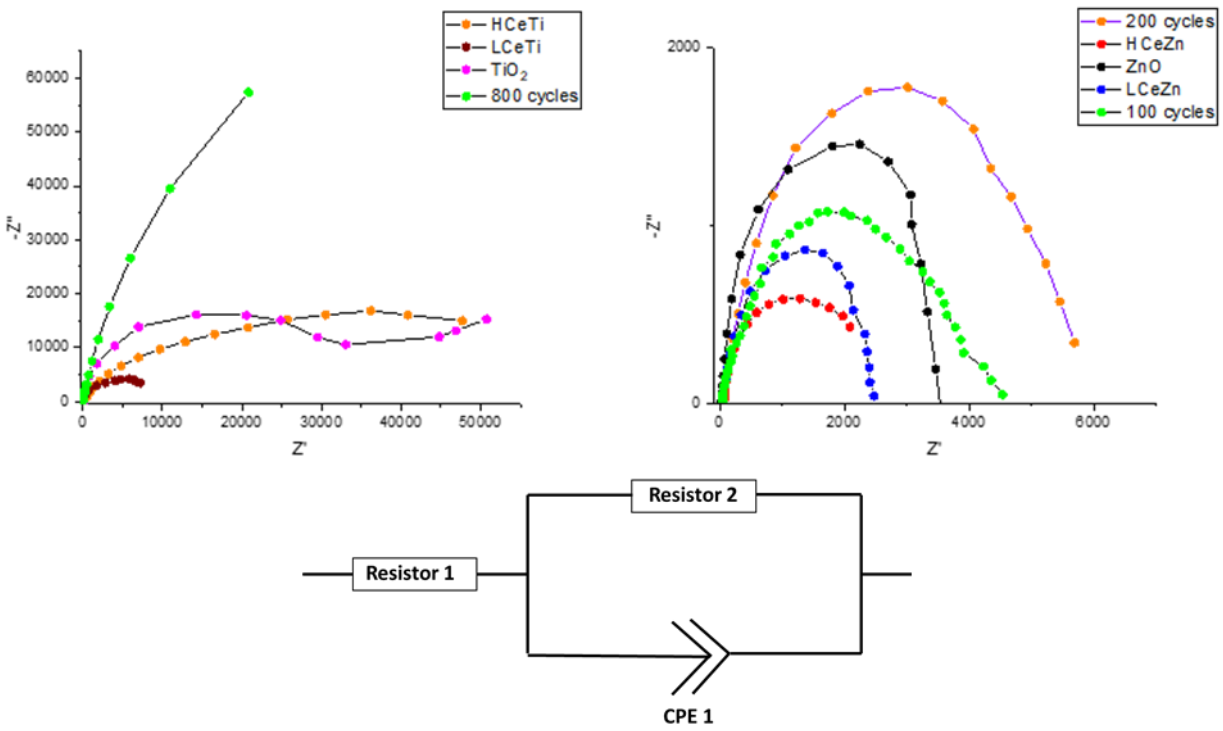

Figure 85 *(Up) Nyquist plot of ZnO and TiO_2 based photoanodes and (down) equivalent circuit used to fit the Nyquist plot obtained.*

Table 7 *Samples and double layer capacitance obtained by plotting the average current at half path against the scan rate.*

Sample	Capacitance from CV	Capacitance from impedance	Resistance form impedance
	C_{DL} (µFarad/cm²)	C_{DL}^{α} (µFarad/cm²)	R_2 (Ω/cm²)
ZnO NR	8.05	11.34	1750.9
1TiO_2@ZnO	6.32	1.80	1960.9
2TiO_2@ZnO	4.55	2.31	2786.8
8TiO_2@ZnO	71.87	67.0	136734.7
LCe-Zn	0.17	7. 09	1220.7
HCe-Zn	0.33	8.73	1010.2
TiO_2 NR	10.44	8.28	40663.3
LCe-Ti	10.55	19.10	4026.9
HCe-Ti	1.82	0.0052	25918.4

3.7.4. Cyclic voltammetry

The average current of all samples measured in dark conditions was plotted against the scan rate and the C_{DL} was identified as the slope (table 3) of the fitted curve (figure 87).

In dark conditions, all materials showed electric double-layer capacitors (EDLC) properties as for ZnO (figure 87), with a potential-independent current related to the capacitance.

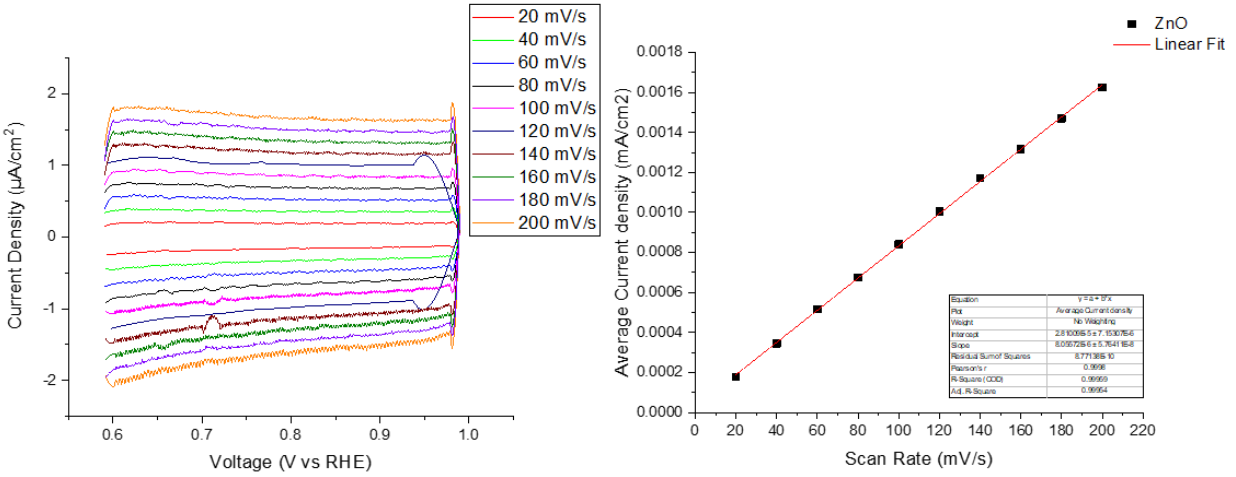

Figure 86 *Current vs voltage in a CV experiment in dark conditions (left) and plot of the average current against the scan rate (right) of ZnO NR in a three-electrode configuration with Pt foil as CE and SCE as RE. The slope of the linear fit has been considered for the evaluation of the slope as the double layer capacitance.*

However, in presence of light, the current become potential-dependent as effect of modified charge mobility on the electrode surface and possibly resulting in a modified charge-discharge process, as suggested by the change in slope of the current-to-voltage potential (Figure 88-90). An exception was represented by 8TiO_2@ZnO (figure 88d) which maintained an EDLC behaviour also under UV-Vis light illumination.

The slower discharge rate displayed for LCe-Zn and HCe-Zn (figure 89a, b), was likely attributed either to an electron exchange between the two oxides or to a possible instability with consequent surface corrosion and degradation, as also hypothesised for ZnO (figure 88a).

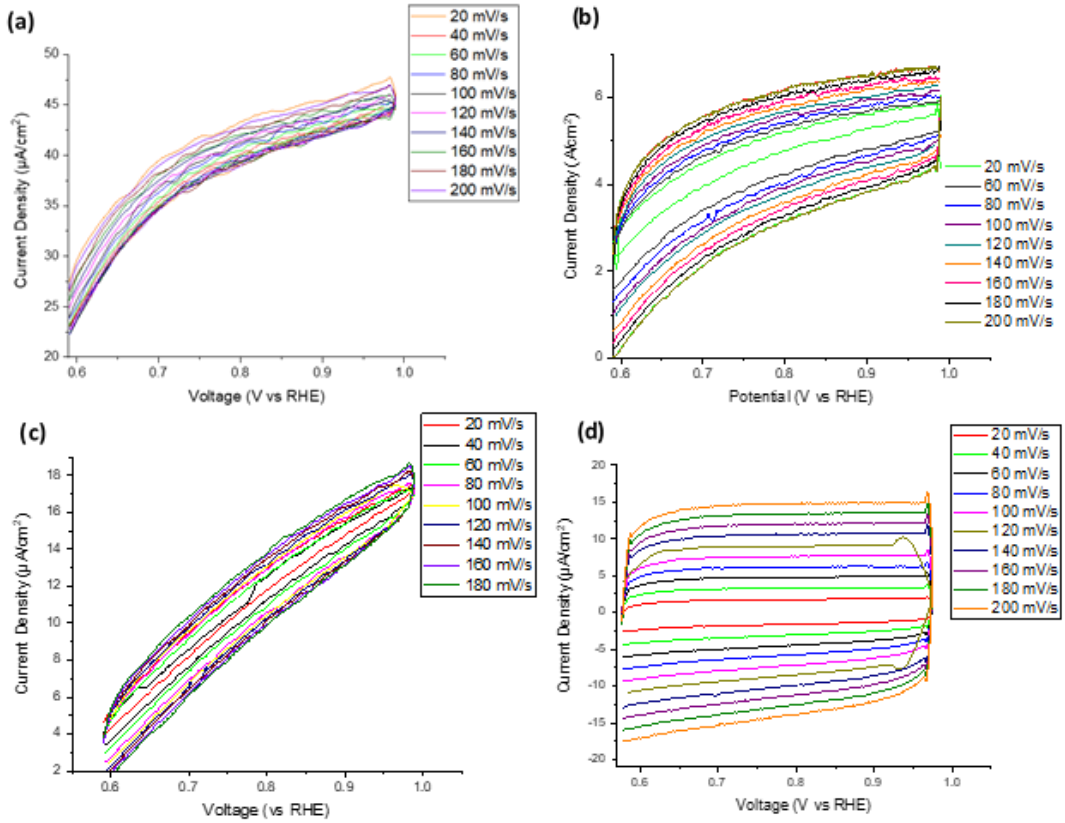

Figure 87 *CV experiment of (a) ZnO NR, (b) 1TiO_2@ZnO, (c) 2TiO_2@ZnO and (d) 8TiO_2@ZnO under UV-Vis light illumination in a three-electrode configuration with Pt foil as CE and SCE as RE.*

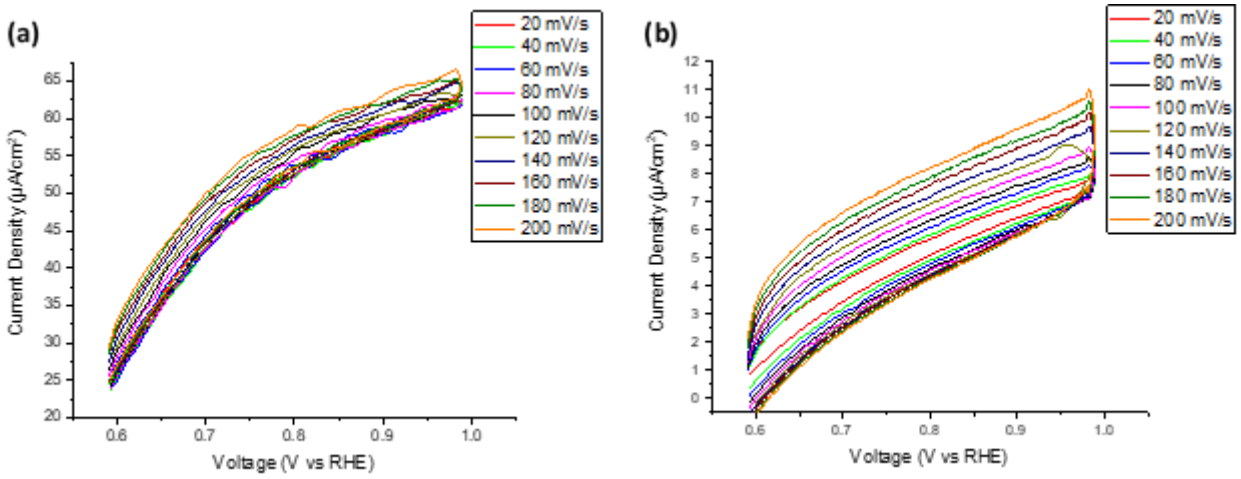

Figure 88 *CV experiment of (a) LCe-Zn and (b) HCe-Zn under UV-Vis light illumination in a three-electrode system with Pt foil as CE and SCE as RE.*

Eventually, the asymmetry of HCe-Ti and LCe-Ti cyclic voltammogram (figure 90 b, c) was suggested as possible indication of pseudocapacitive behaviour, which could derive either from the effect of the light source or from the appearance of a Faradaic charge exchange, related to the presence of Ce^{3+} and Ce^{4+} states combined with Ti^{3+} and Ti^{4+} [34]. The calculated C_{DL} values were found in high

disagreement (≤ 50 %) when compared to the values obtained by the EIS data evaluation (C_{DL}^{α}). Nevertheless, more importantly, the general trend of the capacitance dependent on the material composition remained unvaried (table 3), thereby further supporting the suggested mechanism and its relation to the SC-SC interaction (section 2.9).

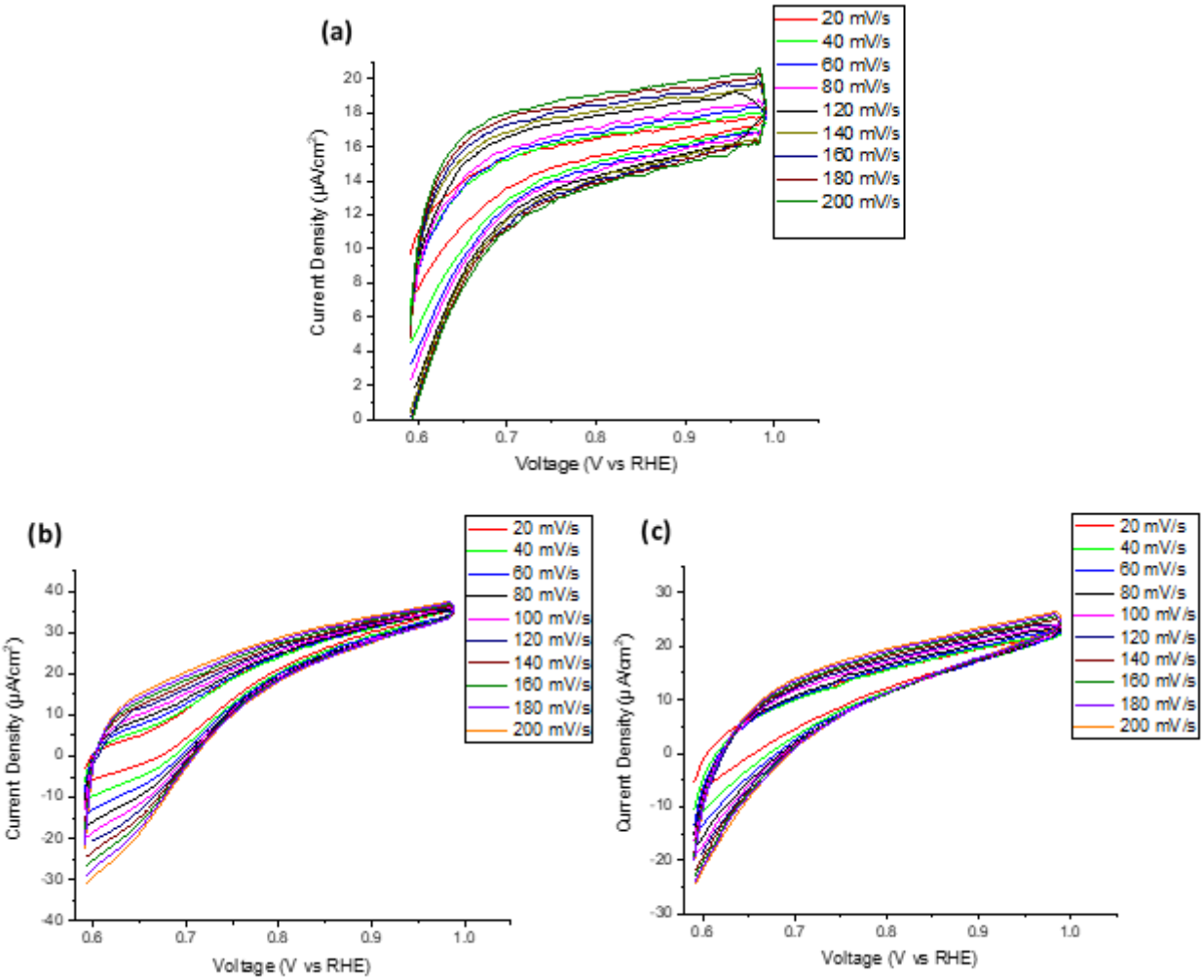

Figure 89 *CV experiment of (a) TiO_2 NR, (b) LCe-Ti and (c) HCe-Ti upon UV-Vis light illumination in a three-electrode configuration with Pt foil as CE and SCE as RE.*

3.8. UV-Visible absorption

Both CeO_2 and TiO_2 coating of ZnO NR affected the absorption, by either providing an increase or a decrease in the UV-visible absorption spectra (figure 91a and b). HCe-Zn, 2TiO_2@ZnO and 8TiO_2@ZnO samples showed an increase in the UV-light absorption. The visible-light absorption in 8TiO_2@ZnO (figure 91b) was attributed to the low crystallinity of the 40-nm-thick TiO_2 layer, which in fact had a blackish appearance. The presence of both CeO_2 and TiO_2 coating in low

amounts (LCeZn and 1TiO_2@ZnO), which was hypothesized as the dominance of a shielding effect over the absorption contribution for very thick layers.

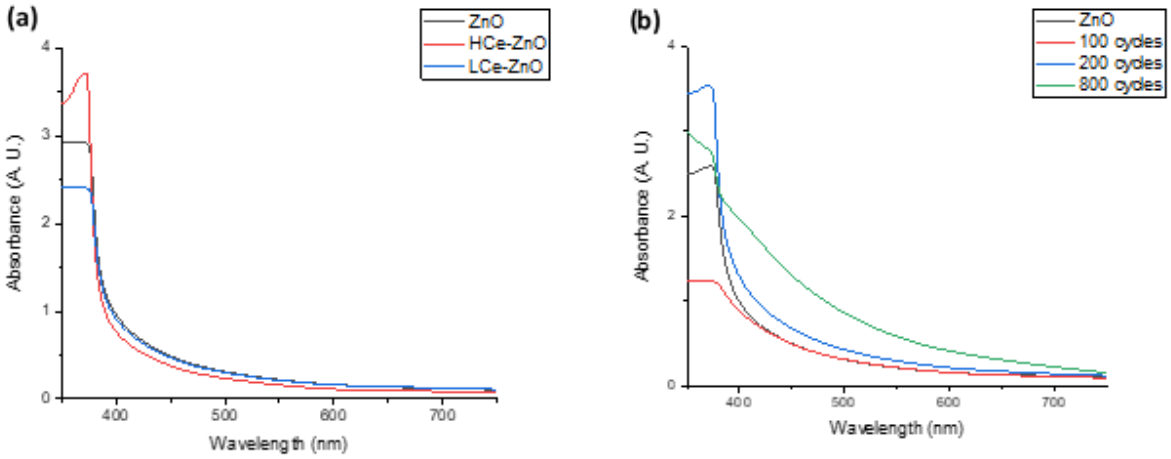

Figure 90 *UV-Vis absorption spectra of (a) Ce-coated ZnO NR and (b) TiO2@ZnO NR against the control ZnO NR.*

Conversely, the presence of CeO2 in TiO2 NR increased the absorption for both HCe-Ti and LCe-Ti (figure 92). An increase in the absorption was attributed to the presence of additional UV absorbing materials, such as TiO2 or CeO2 as elsewhere reported [10], while the decrease could be attributed to several factors, such as low crystallinity or increased scattering effects.

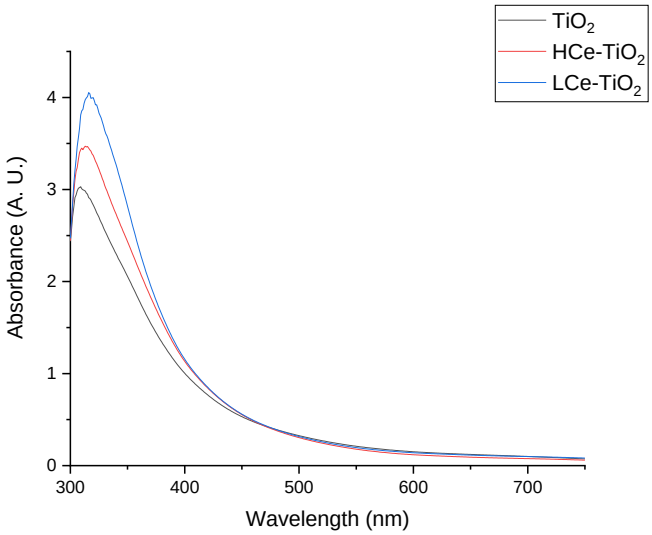

Figure 91 *UV-Vis spectra of Ce-coated TiO_2 NR*

3.9. Photo-elecrocatalysis of methylene blue

The photodegradation of MB under UV-Vis illumination was evaluated either with or without the application of a 0.2 V (vs SCE) potential, in order the relate the obtained results to the calculated C_{DL} and resistance by EIS and CV analysis (see section 3.9 and 3.10). As shown in figure 93 and 94, all samples showed similar photocatalytic properties. The material with the highest performance was identified as HCe-Ti with an applied potential of 0.2 V (vs SCE) and TiO_2 without any potential after 75 min of light exposure. Notably, the application of a potential only slightly improved (17%) the photocatalytic performance of all samples but one ($1TiO_2$@ZnO). The effect of layers with different thickness of ALD grown TiO_2 had already shown a thickness-dependent photocatalytic activity, which was improved by the application of a 0.6 V (vs Ag/AgCl) potential [33], although the layer thickness in $1TiO_2$@ZnO, $2TiO_2$@ZnO and $8TiO_2$@ZnO samples was not comparable [33]. Moreover, it is possible that the potential applied was too low to obtain a remarkable change in the photocatalytic performance, which could rather occur with a further increase in the potential [33, 34].

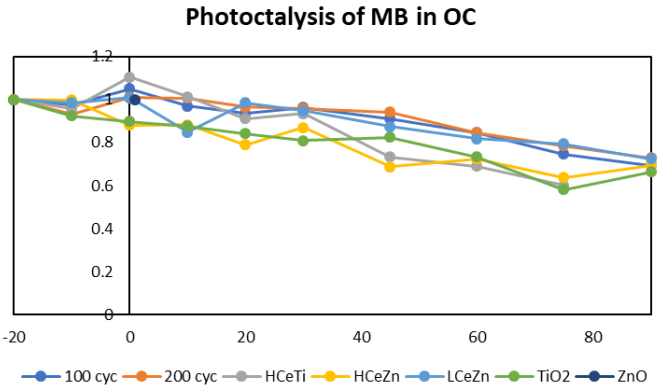

Figure 92 *Time-related evolution of the photodegradation of MB under UV-Vis illumination.*

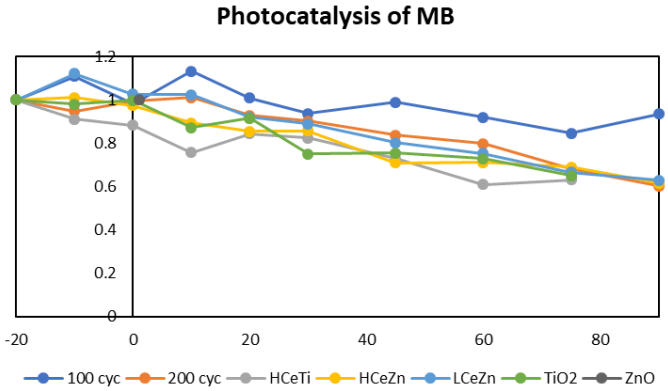

Figure 93 *Time-related evolution of the photodegradation of MB under UV-Vis illumination with an applied bias of 0.2 V (vs SCE)*

4. Conclusions

In conclusion, earth-abundant semiconductors such as ZnO and TiO_2 nanorods were synthesized on FTO electrodes by hydrothermal method. The PEC and photocatalytic properties of samples were studied as photoanodes and the effect of a thin-layer coating by mean of two different techniques was evaluated and compared. Although the application of a bias was damaging for many of the materials, in different extents, it was able to improve the photocatalytic performance of most samples. Coating with Ce not merely provided modification of the optical behaviour of Zn-based materials, but also photo-protection under UV-Vis illumination. CV and EIS confirmed the capacitor-like behaviour of most ZnO-based materials, which were further increased with the presence of a 40 nm-thick ALD grown TiO_2 layer.

Eventually, PL, XRD and SEM analysis provided optical and structural characterization enabling the understanding of the surface and interface behaviour of the proposed materials. Further assessment would include the evaluation of oxidative properties in OC combined to surface defects evaluation and additional photo-electrocatalytic experiments to confirm the detected behaviour with application of different potentials.

5. Bibliography

[1] B. Metz, O.R. Davidson, P.R. Bosch, R. Dave, L.A. Meyer, *IPCC, 2007: Climate Change 2007: Mitigation. Contribution of Working Group III to the Fourth Assessment Report of the Intergovernmental Panel on Climate Change, Cambridge University Press, Cambridge, United Kingdom and New York, NY, USA., XXX*

[2] O. Edenhofer, R. Pichs-Madruga, Y. Sokona, K. Seyboth, P. Matschoss, S. Kadner, T. Zwickel, P. Eickemeier, G. Hansen, S. Schlömer, C. von Stechow, *IPCC, 2011: Summary for Policymakers. In: IPCC Special Report on Renewable Energy Sources and Climate Change Mitigation*, Cambridge University Press, Cambridge, United Kingdom and New York, NY, USA.

[3] O. Ellabbana, H. Abu-Rubb and F. Blaabjerg *Renewable energy resources: Current status, future prospects and their enabling technology*, Renewable and Sustainable Energy Reviews (2014) 39, 748–764

[4] T. Jafari, E. Moharreri, A. Shirazi Amin, R. Miao, W. Song and S. L. Suib, *Photocatalytic Water Splitting—The Untamed Dream: A Review of Recent Advances,* Molecules (2016) 21(900), 1-29

[5] M. Ni, M. K. H. Leung, D. Y. C. Leung and K. Sumathy, *A Review and recent developments on photocatalytic water-splitting using TiO_2 for hydrogen production,* Renewable and Sustainable Energy Reviews (2007) 11, 401–425

[6] S. Choudary, S. Upadhyay,P. Kumar, N. Singh, V. R. Satsangi, R. Shrivastav and S. Dass, *Nanostructured bilayered thin films in photoelectrochemical water-splitting – A review.* International Journal of Hydrogen Energy (2012) 37, 18713-18730

[7] Y. Lin, G. Yuan, R. Liu, S. Zhou, S. W. Sheehan, D. Wang, *Semiconductor nanostructure-based photoelectrochemical water splitting: A brief review*. Chemical Physics Letters (2011) 507, 209–215

[8] A. Wolcott, W. A. Smith, T. R. Kuykendall, Y. Zhao and J. Z. Zhang, *Photoelectrochemical water splitting using dense and aligned TiO_2 nanorods arrays*, Small (2009) 5(1), 104–111

[9] Wang S, Zhu B, Liu M, Zhang L, Yu J, Zhou M, *Direct Z-scheme ZnO/CdS hierarchical photocatalyst for enhanced photocatalytic H2-production activity*, Applied Catalysis B: Environmental (2018), https://doi.org/10.1016/j.apcatb.2018.10.019

[10] K. Jeong, P. R. Deshmukh, J. Park, Y. Sohn and W. G. Shin, *ZnO-TiO_2 Core−Shell Nanowires: A Sustainable Photoanode for Enhanced Photoelectrochemical Water Splitting,* ACS Sustainable Chem. Eng. 2018, 6, 6518−6526

[11] B. S. Shaheen, H. G. Salem, M. A. El-Sayed and N. K. Allam, *Thermal/Electrochemical Growth and Characterization of OneDimensional ZnO/TiO2 Hybrid Nanoelectrodes for Solar Fuel Production, J. Phys. Chem. C 2013, 117, 18502−18509*

[12] S. Kundu, J. Ciston, S. D. Senanayake, D. A. Arena, E. Fujita, D. Stacchiola, L. Barrio, R. M. Navarro, J. L. G. Fierro, and J. A. Rodriguez, *Exploring the Structural and Electronic Properties of Pt/Ceria Modified TiO2 and Its Photocatalytic Activity for Water Splitting under Visible Light*, J. Phys. Chem. C (2012) 116, 14062−14070

[13] S. A. Khan, S. B. Khan and A. M. Asiri, *Electro-catalyst based on cerium doped cobalt oxide for oxygen evolution reaction in electrochemical water splitting,* J Mater Sci: Mater Electron (2016) 27, 5294–5302

[14] M. Mayer, *Rutherford Backscattering Spectrometry (RBS*), Workshop on Nuclear Data for Science and Technology: Materials Analysis Trieste, (2003), LNS0822003

[15] S. Mendoza, E. Bustos, J. Manríquez, L. A. Godínez, *Voltammetric Techniques*, Agricultural and Food Electroanalysis, First Edition © John Wiley and sons, Ch. 2, 24-30

[16] H. Wang and L. Pilon, *Physical interpretation of cyclic voltammetry for measuring electric double layer capacitance*, Electrochimica Acta (2012) 64, 130-139

[17] Bio-Logic Science Instruments, *Measurement of the double layer capacitance,* www.biologic.info, 1-4

[18] Y. Gogotsi and R. M. Penner, *Energy Storage in Nanomaterials − Capacitive, Pseudocapacitive, or Battery-like?* ACS Nano (2018) 12, 2081−2083

[19] P. R. Deshmukh, Y. Sohn and W. G. Shin, Chemical *Synthesis of ZnO nanorods: investigation of electrochemical performance and photoelectrochemical water splitting application*, Journal of Alloys and Compounds (2017) 711, 573-580

[20] A. Lasia, *Electrochemical Impedance Spectroscopy and Its Applications, Modern Aspects of Electrochemistry*, from B. E. Conway, J. Bockris and R.E. White, Kluwer Academic/Plenum Publishers, New York, 1999, Vol. 32, p. 143-248.

[21] *Basics of Electrochemical Impedance Spectroscopy*, Application Note, Rev. 1.0 11/9/2016 © Copyright 1990-2016 Gamry Instruments, Inc., 1-19

[22] R. K. Singh, R. Devivaraprasad, T. Kar, A. Chakraborty and M. Neergat, *Electrochemical Impedance Spectroscopy of Oxygen Reduction Reaction (ORR) in a Rotating Disk Electrode Configuration: Effect of Ionomer Content and Carbon-Support*, Journal of The Electrochemical Society, 162 (6) F489-F498 (2015)

[23] B. Bera, T. Kar, A. Chakraborty and M. Neergat, *Influence of nitrogen-doping in carbon on equivalent distributed resistance and capacitance – Implications to electrocatalysis of oxygen reduction reaction*, Journal of Electroanalytical Chemistry (2017) 805, 184–192

[24] C. C. L. Mc Crory, S. Jung, J. C. Peters and Thomas F. Jaramillo Benchmarking *Heterogeneous Electrocatalysts for the Oxygen Evolution Reaction*, J. Am. Chem. Soc. (2013) 135, 16977−16987

[25] A. M. T. Silva, C. G. Silva, G. Drazic, J. L. Faria, *Ce-doped TiO_2 for photocatalytic degradation of chlorophenol,* Catalysis Today (2009) 144, 13–18

[26] K. H. Tam, C. K. Cheung, Y. H. Leung, A. B. Djurisic, C. C. Ling, C. D. Beling, S. Fung, W. M. Kwok, W. K. Chan, D. L. Phillips, L. Ding and W. K. Ge, *Defects in ZnO Nanorods Prepared by a Hydrothermal Method*, J. Phys. Chem. B (2006) 110, 20865-20871

[27] B. Djurišić, Y. H. Leung, K. H. Tam, Y. F. Hsu, L. Ding, W. K. Ge, Y. C. Zhong, K. S. Wong, W. K. Chan, H. L. Tam, *Defect emissions in ZnO nanostructures*, Nanotechnology (2007) 18, 095702, 1-8

[28] Y. H. Leung, A. B. Djurišić, Z. T. Liu, D. Li ,M. H. Xie, W. K. Chan, *Defect photoluminescence of ZnO nanorods synthesized by chemical methods*, Journal of Physics and Chemistry of Solids (2008) 69(2-3), 353-357

[29] B. Panigrahy, M. Aslam, D. S. Misra, M. Ghosh and D. Bahadur, *Defect-Related Emissions and Magnetization Properties of ZnO Nanorods,* Adv. Funct. Mater. (2010) 20, 1161-1165

[30] B. Bera, T. Kar, A. Chakraborty and M. Neergat, *Influence of nitrogen-doping in carbon on equivalent distributed resistance and capacitance – Implications to electrocatalysis of oxygen reduction reaction*, Journal of Electroanalytical Chemistry (2017) 805, 184–192

[31] R. K. Singh, R. Devivaraprasad, T. Kar, A. Chakraborty and M. Neergat, *Electrochemical Impedance Spectroscopy of Oxygen Reduction Reaction (ORR) in a Rotating Disk Electrode Configuration: Effect of Ionomer Content and Carbon-Support*, Journal of The Electrochemical Society, 162 (6) F489-F498 (2015)

[32] R. Beranek, *(Photo)electrochemical Methods for the Determination of the Band Edge Positions of TiO_2-Based Nanomaterials*, Advances in Physical Chemistry (2011), 786759, 1-20

[33] M. Heikkila, E. Puukinlainen, M. Ritala and M. Leskela, *Effect of thickness of ALD grown TiO_2 films on photoelectrocatalysis,* Journal of Photochemistry and Photobiology A: Chemistry (2009) 204, 200–208

[34] J. Ouyang, M. Chang and X. Li, CdS-sensitized ZnO nanorod arrays coated with TiO2 layer for visible light photoelectrocatalysis, J. Mater. Sci. (2012) 47, 4187–4193

AKNOWLEDGEMENTS

After more than a couple of year of intense and fruitful study, I would like to sincerely thank whoever crossed my path, whatever the role, which somehow contributed to enriching my perspective.
In particular, thanksgivings from the bottom of my heart go to: my mother, who supported me every step and donated me the freedom that I aim to celebrate; my sister, for suggesting not to aim for perfection; Francesco, for supporting me as a daughter; Salva, for praising me with its endless love; Franci, for being dear to my real self; Zelal, for teaching me what love really means; Fethiye, for reminding me to be present to myself and to enjoy life in every moment; Mehmet, for opening its house and heart even when that meant to suffer, and all of the friends that I have not mentioned but I thank for being part of my life. I thank Danny, for its inestimable support and its example of intelligence, competency and hard-working, which allowed me to progress both in science and life. Moreover, sincere thanks to all the members of the CATMAT lab, with which I pleasantly shared the last few months, with a special tahanks to the prof. Signoretto, for the rewarding opportunities which gifted me with.
Eventually, after my pleasant staying at Luleå Tekniska Universitet, I would also like to sincerely thanks: the prof. Isabella Concina, for her useful direction, suggestion, corrections, as well as for her patience, which also motivated my self-improvement and growth in science; Anton Lanstrom for the trust, the advices and therefore the opportunity to work in autonomy in a stimulating environment; Getachew Solomon, for his uttermost role as co-supervisor, essentially contributing to my understanding of electrochemical analysis and experiments, and as friend for reminding me whenever and wherever I have been wrong; Mojtaba Gilzad Kohan, for its scientific support, advices and friendly availability whenever required.

Thank you.

You all are in my biology, for life.